Calorimetric and Magnetic Studies on the Vortex Lattice of Low-T_c Superconductors

---

Dissertation
zur
Erlangung der naturwissenschaftlichen Doktorwürde
(Dr. sc. nat.)
vorgelegt der
Mathematisch-naturwissenschaftlichen Fakultät
der
Universität Zürich
von

Olaf Bossen

aus
Deutschland

Promotionskomitee:
Prof. Dr. Andreas Schilling (Vorsitz und Leitung)
Prof. Dr. Hugo Keller
Prof. Dr. Ueli Straumann

Zürich, 2013

Zusammenfassung

Thermodynamische und magnetische Messungen zeigen, dass das Vortexgitter von Hoch-T_c-Kupratsupraleitern einen Schmelzübergang in eine flüssige Phase beim Überschreiten einer Schmelztemperatur $T_m > T_c$ aufweist. Es ist davon auszugehen, dass dieser Phasenübergang nicht auf das Vortex-Gitter von Hoch-T_c-Supraleitern beschränkt ist, sondern dass er auch in Niedrig-T_c-Supraleitern auftritt. Allerdings konnte in diesen Stoffen jenes Phänomen noch nicht eindeutig nachgewiesen werden. In dieser Arbeit diskutieren wir etablierte Theorien des Vortex-Gitters zur Berechnung der Schmelzentropie und des damit verbundenen Magnetisierungssprungs. Für eine Anzahl von gebräuchlichen Niedrig-T_c-Supraleitern werten wir die erhaltenen Formeln mit Literaturwerten für die Materialparameter numerisch aus, um eine Aussage über die benötigte Messgenauigkeit zur Detektion des Vortexgitter-Schmelzens zu machen. Um unsere Vorhersagen bezüglich der magnetischen und thermischen Signatur des Vortex-Gitter-Schmelzens zu überprüfen, haben wir A.C.-Magnetisierungs-Messungen und thermische Messungen an einer Nb_3Sn-Probe durchgeführt, welche in früheren Messungen anderer Autoren Anzeichen eines Vortexgitter-Schmelzens gezeigt hat. Dabei zeigt sich eine Doppelspitzen-Struktur im Imaginärteil der magnetischen Suszeptibilität, welche durch das Anwachsen des kritischen Stroms in der „Peak-Effect“-Region dieser Probe erklärt werden kann, und welche zu einer stark temperaturabhängigen magnetischen Selbsterwärmung der Probe im A.C.-Magnetfeld führt. Wir zeigen, wie die „Vortexgitter-Schüttel“-Methode durch ebendiese Selbsterwärmung Artefakte ähnlich der Schmelzsignatur in Wärmekapazitäts-Messungen verursachen kann, und wie man diese Artefakte in der Analyse mittels einer Phasenkorrektur des Messsignals wieder entfernt. Schließlich beschreiben wir eine neuartige Wärmekapazitäts-Messmethode, welche auf dem Prinzip eines thermischen Oszillators basiert und gegenüber herkömmlichen Methoden bessere statistische Eigenschaften aufweist.

Abstract

Thermodynamic and magnetic measurements show that the vortex lattice of high-T_c cuprate superconductors undergoes a melting transition into a vortex liquid phase, when the temperature exceeds a melting temperature $T_m < T_c$. It is to be expected that this phase transition is not an exclusive property of the vortex lattice of high-T_c superconductors, but it should be displayed by the vortex lattice of low-T_c superconductors as well. Nevertheless, an unequivocal confirmation of this phenomenon is still missing in such compounds. In this work we review established theories of the vortex lattice to predict the vortex lattice melting entropy and the associated magnetization discontinuities. For a number of common low-T_c superconductors we evaluate the obtained formulas numerically using literature values for material properties in order to make a judgment on the resolution requirements for the experimental detection of a vortex lattice melting. In order to test our predictions for the thermal and magnetic signature of vortex lattice melting we performed AC magnetization and thermal measurements on a sample of Nb_3Sn for which signs of a vortex lattice melting transition have been reported by other authors in the past. The measurements reveal a double-peak structure in the imaginary part of the magnetic susceptibility, which can be explained by the increase of the critical current in the "peak effect region" of this sample, and which cause a strongly temperature dependent self heating of this sample inside an AC magnetic field. We show how the "vortex lattice shaking" method employed in heat capacity measurements may cause melting like artifacts in heat capacity measurements due to the aforementioned self heating, and demonstrate how these artifacts can be removed in the analysis by a phase correction of the measurement data. Finally, we describe a novel method for heat capacity measurements based on a thermal oscillator approach, with superior statistical properties as compared to more traditional measurement techniques.

Publications pertaining to this work

- O. Bossen and A. Schilling, “Estimates for the thermodynamic signatures of vortex-lattice melting in conventional superconductors”, *Physica C*, vol. 483, pp. 201 – 206, 2012.
- O. Bossen and A. Schilling, “LC-circuit calorimetry”, *Rev. Sci. Instrum.*, vol. 82, pp. 094901, 2011.
- O. Bossen and A. Schilling, “AC magnetic susceptibility in the vortex lattice region in Nb_3Sn”, *Physica C*, vol. 492, pp. 133 – 137, 2013.

Contents

1. Introduction

The field of low temperature physics was initiated by Kamerlingh Onnes when he successfully liquefied Helium and achieved temperatures below 4 K [1]. One of his first discoveries in this temperature region was the superconductivity of mercury, which was detected as the disappearance of resistance in this metal below a critical temperature of $T_c = 4.2\,\mathrm{K}$ [2–4]. Once other laboratories succeeded in liquefying helium as well, many other metals were discovered to show the same property. One of the first applications envisioned for superconductivity was that of superconducting electro magnets, which could hold their field indefinitely long without a continuous energy source due to the absence of resistive losses. In 1933 Meissner and Ochsenfeld discovered that elemental superconductors expel magnetic fields from their interior [5]. This showed that the superconducting state is independent of a material's magnetic history, which allows for the treatment of superconductivity as a thermodynamic state of matter and explains why superconductivity breaks down in sufficiently high magnetic fields, rendering the materials known at the time of little use for the construction of high field superconducting magnets. The superconducting state found an electromagnetic description in the equations by London and London [6] soon after in 1935. The *London equations* show that the magnetic fields are confined to a surface layer with a characteristic thickness called the London penetration depth λ_L. High field superconducting magnets were deemed unfeasible until it was discovered that some alloys allowed the magnetic field to penetrate the superconductor partially, even though it was expelled due to the Meissner Ochsenfeld effect in the elemental parent compounds. Better understanding of this type of mixed state came in 1950 when Ginzburg and Landau developed a phenomenological theory of superconductivity that allowed for the description of the spatial variation of the electronic system in the superconductor [7], which allowed Abrikosov to formulate his theory of the mixed state [8] in the type II superconductors, showing that these superconductors are penetrated by a lattice of magnetic flux quanta (vortices) allowing them to resist much higher magnetic fields. Four years later

Matthias *et al.* discovered the type II superconductor Nb_3Sn which is still the high performance superconductor used in most high field magnets today. The understanding of the microscopic origin of the Ginzburg-Landau theory was advanced after the discovery of the isotope effect in mercury by Reynolds *et al.* [9] and independently by Maxwell [10], which lead Fröhlich to the insight that superconductivity must be caused by phonon mediated electron interaction [11]. Cooper discovered that an arbitrarily small attraction of electrons would lead to the collapse of the metallic ground state of a material [12]. Together with Bardeen and Schrieffer they devised the theory of the BCS ground state [13, 14], which was later used by Gor'kov to justify the theoretical treatment by Ginzburg and Landau, for materials close to the superconducting phase transition [15, 16]. The BCS theory and its extensions are the accepted theories of how superconductivity works at the microscopic level. Due to theoretical arguments it was thought that the critical temperature of the A-15 class of superconductors with a maximum T_c of 23 K was close to the upper limit for such a phononic interaction. Therefore it came as a surprise when in 1986 Bednorz and Müller announced their discovery of the high temperature superconductivity in the Ba–La–Cu–O cuprate system [17]. After this discovery a range of high temperature cuprates were discovered, many of which have critical temperatures above the atmospheric pressure boiling point of liquid nitrogen ($T_{\mathrm{LN}_2} = 77.36\,\mathrm{K}$.) Based on this and other discoveries [18, 19] it is now believed that the interaction, which leads to the binding of electrons into so called *Cooper pairs* does not necessarily need to be based on phonons alone.

As in all type II superconductors the current carrying capability of the cuprates is influenced by the vortex dynamics of the superconductor. An ideal type II superconductor would turn resistive with the appearance of vortices, which would move freely under the effects of the Lorenz force and dissipate energy. The reason for this not to happen is *vortex pinning* – the trapping of vortices to perturbations in the crystal lattice, which renders them immobile unless the transported current is very high or the temperature is close to T_c. In that case the vortices start to *creep*, which leads to a finite resistance [20]. The pinning also causes a hysteresis in the magnetization and hinders the formation of a regular *vortex lattice* – a perfectly periodic arrangement of vortices, which can be observed in high purity single crystalline samples. In cuprate superconductors, this lattice shows a first order melting transition into a “liquid” state at a melting temperature $T_m < T_c$ [21–23], an effect that seems to be suppressed in samples of lower purity where pinning centers drive the transition to be glass-like. A deeper understanding of the effects of pinning is very much desirable as they can enhance j_c considerably. In certain cases, and for reasons that are not fully understood, some superconductors show a strong increase of j_c just before the transition to the normal state, thus breaking the trend of decreasing critical current with increasing temperature. This is called the *peak effect*. It was first discovered in Nb alloys by Berlincourt *et al.* [24].

One early explanation for the peak effect was given by Pippard [25]. His model describes a weakening of the vortex-vortex interaction leading to an attachment of the individual vortices to more pinning sites as they can adjust more freely. This picture is incompatible with the existence of a perfectly ordered rigid vortex lattice inside the peak effect region of the magnetic phase diagram.

Quite surprisingly in a report by Lortz *et al* [26], the occurrence of a vortex-related first-order transition in the peak effect region of Nb_3Sn was reported, resembling the melting transition of a perfectly ordered vortex lattice. In this work we attempted to reproduce these measurement, and discuss the more general question whether low-T_c superconductors show a measurable melting entropy according to established theories for the vortex lattice melting transition, and it turns out that this entropy can be very small.

Furthermore we discuss the magnetic signature of a first order vortex lattice melting transition and the appearance of multiple maxima of the AC magnetic susceptibility in superconductors showing a "peak effect".

We present measurements on a Nb_3Sn single crystal of both the AC magnetic susceptibility and the heat capacity, where we demonstrate how the strongly varying AC magnetic susceptibility in the peak effect region of the Nb_3Sn sample can lead to melting-like artifacts in heat capacity measurements if an auxiliary vortex "shaking" field is used as in the measurements performed in Ref. [26].

Because of the smallness of the expected thermal signatures we suggest a novel measurement technique that may improve the accuracy of current calorimetric techniques in the future. It is based on a thermal LC oscillator circuit, and it possesses superior statistical properties as compared to those of traditional methods.

2. Superconductivity

Superconductivity is a low temperature phenomenon with numerous effects on various material properties, e.g. the resistivity, heat capacity and magnetization. For the sake of brevity we will not proceed with the theory of superconductivity in its historical order, but we will start with the London equations, continue with a description at the microscopic level using the Bardeen-Cooper-Schrieffer (BCS) model, and sketch the Ginzburg-Landau theory as well as the macroscopic effects subsequently. For a more thorough treatment we refer to Tinkham's monograph [27], which we follow here with certain adjustments, most notably the conversion of the equations to SI units.

2.1. London equations

In 1911 Kammerlingh-Onnes discovered the disappearance of the electrical resistance of mercury at a temperature of $T_c = 4.19\,\mathrm{K}$ [2–4] and coined the term *superconductivity* for this phenomenon. Due to the disappearance of the resistance in a superconductor and Ohm's law $R = U/I = 0$ the potential difference between any two points of the superconductor is zero, and together with Faraday's law $U = -\frac{\mathrm{d}\Phi_B}{\mathrm{d}t} = 0$ one finds that the magnetic flux Φ_B through an area enclosed by any contour within a superconductor must be constant. If superconductivity would only signify perfect conductivity, it could not be described as a thermodynamic phase of matter as the energy density of the magnetic field could be "frozen" at its value upon the start of perfect conductivity, and the thermodynamic state would thus not be path independent. In 1933 this mystery was resolved when Meissner and Ochsenfeld discovered that tin and lead expelled magnetic fields upon entering the superconducting state [5], which shows that superconductivity corresponds to a thermodynamic phase of matter. The uniqueness of this thermodynamic state made it possible to use an effective thermodynamic treatment using the Landau theory of phase transitions, which we will discuss in section 2.3.

The mathematical description for the magnetic field and the electrical currents in the presence of a field-expelling superconductor was given by the London equations two years after Meissner and Ochsenfeld's discovery [6].

$$\mathbf{E} = \frac{\partial}{\partial t}\left(\Lambda \mathbf{j}_s\right), \tag{2.1}$$

$$\mathbf{H} = -\operatorname{curl}\left(\Lambda \mathbf{j}_s\right), \tag{2.2}$$

$$\Lambda = \mu_0 \lambda^2 = \frac{m^\star}{n_s \left(e^\star\right)^2}, \tag{2.3}$$

$$\text{or} \quad \lambda = \sqrt{\frac{m^\star}{\mu_0 n_s \left(e^\star\right)^2}}, \tag{2.4}$$

where $\mathbf{E}$ and $\mathbf{H}$ describe the electric and magnetic field on microscopic scales, respectively, $\mathbf{j}_s$ is the superconducting current density, and $m^\star, n_s$ and $e^\star$ are effective mass, density and charge of the charge carriers involved. Substituting the Maxwell equation $\operatorname{curl}\mathbf{H} = \mathbf{j}$ in Eq. (2.2) we obtain

$$\nabla^2 \mathbf{H} = \frac{\mathbf{H}}{\lambda^2}. \tag{2.5}$$

We see that λ is a measure of the depth, over which the magnetic field decays at the interface between vacuum and a superconductor. It is called *magnetic penetration depth* and depends on the material parameters of the superconductor at hand. Eq. (2.1) describes the movement of superconducting charge carriers without resistive friction. Using this fact we can derive from the classical description of current as moving charge carriers $\mathbf{j} = n_s e^\star \mathbf{v}_s$, and the velocity due to the canonical momentum $\mathbf{v}_s = \frac{1}{m^\star}\left(\mathbf{p} - e^\star \mathbf{A}\right)$ the average kinetic energy density of the charge carriers:

$$E_{\text{kin}} = \frac{1}{2} n_s m^\star \mathbf{v}_s^2 = \frac{n_s \left(e^\star\right)^2 \mathbf{A}^2}{m^\star} = \frac{\mathbf{A}^2}{2\mu_0 \lambda^2} \tag{2.6}$$

2.2. BCS model

Bardeen, Cooper and Schrieffer created the foundations of the modern theory of superconductivity in 1951 using a novel microscopic model for a system of correlated electrons, whose main features have been confirmed for most superconductors. Due to the Pauli exclusion principle that forbids electrons to be in the same quantum mechanical state, electrons in crystals form the *Fermi sphere*, i.e. they occupy all electronic states up to an energy called the *Fermi energy* ε_f. The key to understanding superconductivity is the fact first shown by Cooper [12] that this sphere is unstable under arbitrarily weak attractive interactions between electrons. If there is such an interaction, the Fermi sphere collapses and the electrons form bound bosonic pair states – so called *Cooper pairs*.

The starting point of the BCS theory is the theory of a free electron gas inside a conductor. The vacuum state $|\emptyset\rangle$ is the filled Fermi sphere to which electron states are added or removed by creation and annihilation operators. The operator $c^\dagger_{\vec{k},\sigma}$ creates an electron with momentum $\vec{k}$ and spin z-component σ while $c_{\vec{k},\sigma}$ annihilates this state. We assume that there is an attractive interaction between the electrons of momenta $\vec{k}$ and $\vec{k}'$ described by a matrix $V_{\vec{k},\vec{k}'}$, which is symmetric under particle exchange. This interaction stems usually (but not necessarily) from a polarization of the crystal lattice, i.e. an electron passing through the lattice will attract nearby nuclei and leave a wake of positive charge behind. This positive charge in turn attracts other electrons. The Hamiltonian describing this scenario is:

$$\mathcal{H} = \sum_{\vec{k},\sigma} \xi_k c^\dagger_{\vec{k},\sigma} c_{\vec{k},\sigma} + \frac{1}{2} \sum_{\vec{k},\vec{k}',\sigma} V_{\vec{k},\vec{k}'} c^\dagger_{\vec{k},\sigma} c^\dagger_{-\vec{k},-\sigma} c_{-\vec{k},-\sigma} c_{\vec{k},\sigma}, \tag{2.7}$$

$$\xi_k = \frac{\hbar^2 k^2}{2M} - \mu, \tag{2.8}$$

where $\mu = E_F$ is the chemical potential which is approximately equal to the Fermi energy, and $V_{\vec{k},\vec{k}'}$ is a potential that only depends on the difference $\vec{k} - \vec{k}'$ and will be chosen at a later point in this treatment. As an ansatz for the ground state of this system Bardeen, Cooper and Schrieffer proposed

$$|\psi_{\mathrm{BCS}}\rangle = \Pi_{\vec{k}} \left[u_k + v_k c^\dagger_{k,\uparrow} c^\dagger_{-k,\downarrow} \right] |\emptyset\rangle \, . \tag{2.9}$$

By minimizing the expectation value of $\mathcal{H}$ one finds that the value of the parameters u_k and v_k is given by

$$v_k^2 = \frac{1}{2}\left[1 - \frac{\xi_k}{E_k}\right], \tag{2.10}$$

$$u_k^2 = \frac{1}{2}\left[1 + \frac{\xi_k}{E_k}\right], \tag{2.11}$$

$$E_k = \sqrt{\Delta_k^2 + \xi_k^2}, \tag{2.12}$$

with Δ_k as a parameter depending on the choice of the potential $V_{\vec{k},\vec{k}'}$. We choose a potential of the form

$$V_{\vec{k},\vec{k}'} = \begin{cases} -V & \text{if } |\xi_k| < \hbar\omega_D \wedge |\xi_k'| < \hbar\omega_D \\ 0 & \text{otherwise.} \end{cases} \tag{2.13}$$

where ω_D is the Debye frequency of the superconductor. This simple potential is motivated by the idea that the electrons can only bind if phonons exist with energies comparable to the deviation of the electron energy with respect to the Fermi energy. The result is an energy gap that is also independent of k except when $|\xi_k|$ exceeds $\hbar\omega_D$,

$$\Delta_k = \begin{cases} \Delta & \text{if } |\xi_k| \leq \hbar\omega_D \\ 0 & \text{if } |\xi_k| > \hbar\omega_D. \end{cases} \tag{2.14}$$

The energy gap $\Delta = 2\hbar\omega_D e^{-1/N(0)V}$ opens up around the Fermi energy inside which there are no electron states which can be occupied. (This is valid if $N(0)V \ll 1$, where $N(0)$ is the density of states at the Fermi level.) The electrons are bound in pairs which need a minimal energy of 2Δ to break apart. If this energy is not reached this leads to a vanishing electrical resistivity, because scattering cannot take place as there are no available target electron states to scatter to. The BCS treatment allows one to calculate the expected critical temperature from the Debye frequency ω_D

$$k_{\mathrm{B}} T_c \approx 1.14\hbar\omega_D e^{-1/N(0)V}. \tag{2.15}$$

We see that the critical temperature increases if the density of states at the Fermi level is large.

One can calculate the resulting electronic specific heat from the occupation statistics for the electron states around the gap. In the low temperature limit when $T < T_c/10$, the specific heat follows an exponential given by the occupation probability of the gap states. Expressed using the modified Bessel function K_α [13, 14],

$$\frac{c}{\gamma T_c} = \frac{3}{2\pi^2}\left(\frac{\Delta}{k_B T_c}\right)^3\left(\frac{T_c}{T}\right)\left(3K_1\left(\frac{\Delta}{k_B T}\right) + K_3\left(\frac{\Delta}{k_B T}\right)\right), \tag{2.16}$$

which simplifies further as $T \to 0$ to [27]

$$\frac{c}{\gamma T_c} \approx 8.5 e^{-1.44\frac{T_c}{T}}. \tag{2.17}$$

We see that while the electronic specific heat in normal conducting metals is linear in T, i.e. $c_n(T) = \gamma T$ with the Sommerfeld parameter $\gamma = \frac{2}{3}\pi^2 k_B N(0)$, the electronic specific heat in the superconducting state has a completely different temperature dependence. Since the electronic entropy needs to be continuous at the phase transition, the specific heat displays a discontinuity,

$$\frac{c_s(T_c) - c_n(T_c)}{c_n(T_c)} \approx 1.43. \tag{2.18}$$

2.3. Ginzburg Landau theory

The Ginzburg-Landau theory was developed as a macroscopic theory before the microscopic BCS theory had been established. It has been shown by Gor'kov [15, 16] to be an approximation of the BCS theory close to T_c, and is better suited for the description of spatially varying phenomena in superconductors. Using a complex *order parameter* ψ of which the absolute value squared is the cooper pair density $|\psi|^2 = n$ we can expand the free energy $F(\psi)$ as a Taylor series in n up to second order. An term representing the interaction with the vector potential $\mathbf{A}$ accounts for the energy associated with electrical currents, and the term $\frac{\mu_0 H^2}{2}$ represents the magnetic field energy density

$$f = f_{n0} + \alpha \left|\psi\right|^2 + \frac{\beta}{2} \left|\psi\right|^4 + \frac{1}{2m^\star} \left| \left(\frac{\hbar}{i} \nabla - e^\star \mathbf{A} \right) \psi \right|^2 + \frac{\mu_0 H^2}{2}. \tag{2.19}$$

We choose the coefficient $\beta(T) \approx$ const, to be positive, and $\alpha(T)$ temperature dependent and approximately linear around the critical temperature, $\alpha \approx a(T - T_c)$. This makes α positive above T_c in the absence of currents and ensures a minimum at $|\psi| = 0$. Thus, we see that the free energy favors a cooper pair density of 0 above T_c. Below T_c the energy minimum is reached for a Cooper pair density $\left|\psi\right|^2 = -\frac{\alpha(T)}{2\beta(T)}$.
By identifying the energy density containing $\mathbf{A}$ in Eq. (2.19) with the kinetic energy from Eq. (2.6) one obtains the effective penetration depth in terms of measurable physical quantities [27]:

$$\lambda_{\text{eff}}^2 = \frac{m^\star}{\mu_0 \left|\psi\right|^2 (e^\star)^2} = \frac{m}{2\mu_0 \left|\psi\right|^2 e^2}. \tag{2.20}$$

Here we identified $e^\star$ and $m^\star$ with the charge and the mass of a Cooper pair, hence $e^\star = 2e$ and $m^\star = 2m$, where m is the effective mass of the electrons in the conduction band.

Using the penetration depth one can express α and β in terms of parameters that are accessible to measurement.

$$\alpha(T) = -\frac{e^2 \mu_0^2}{m} H_c^2(T) \lambda_{\text{eff}}^2(T), \tag{2.21}$$

$$\beta(T) = \frac{2e^4 \mu_0^3}{m^2} H_c^2(T) \lambda_{\text{eff}}^4(T). \tag{2.22}$$

Here $H_c(T)$ is the thermodynamical critical field above which the cost to expel the magnetic field is locally higher then the gain to form cooper pairs. So far we have used the assumption that $\left|\psi\right|^2$ varies weakly in space, which is often a good assumption, but which breaks down in two cases: In the presence of thermal fluctuations and in the so called type II superconductors in the mixed state (see. Section 3.1).

2.4. The Ginzburg Landau Differential Equations

In oder to describe effects of a spatially varying magnetic field we assume that the free energy given by Eq. (2.19) is minimal for a given $\psi_0(\vec{r})$. For this it is necessary that the variational derivative of the free energy $F(\psi) = \int_V f(\psi(\vec{r}))\mathrm{d}^3 r$ disappears:

$$\left.\frac{\delta F(\psi)}{\delta \psi}\right|_{\psi_0} = 0. \tag{2.23}$$

Using the calculus of variations this condition can be rewritten as a system of differential equations:

$$\alpha\psi + \beta\left|\psi\right|^2\psi + \frac{1}{2m^\star}\left(\frac{\hbar}{i}\nabla - e^\star\mathbf{A}\right)^2\psi = 0, \tag{2.24}$$

$$\mathbf{j} = \operatorname{curl}\mathbf{H} = \frac{e^\star\hbar}{2m^\star i}\left(\psi^*\nabla\psi - \psi\nabla\psi^*\right) - \frac{(e^\star)^2}{m^\star}\psi^*\psi\mathbf{A}, \tag{2.25}$$

$$= \frac{e^\star}{m^\star}\left|\psi\right|^2\left(\hbar\nabla\phi - e^\star\mathbf{A}\right) = e^\star\left|\psi\right|^2\mathbf{v}_s, \tag{2.26}$$

where ϕ is the phase of ψ. These equations are the *Ginzburg Landau Differential Equations.* In the absence of magnetic fields or disturbances, ψ reaches the equilibrium value

$$\psi_\infty^2 = \frac{m}{2\mu_0 e^2\lambda_{\mathrm{eff}}^2}. \tag{2.27}$$

Furthermore, when fields are absent ψ can be chosen to be real and to be normalized to $f = \psi/\psi_\infty$. Thus Eq. (2.24) becomes

$$\xi^2(T)\frac{\mathrm{d}^2 f}{\mathrm{d}x^2} + f - f^3 = 0 \quad \text{and} \tag{2.28}$$

$$\xi^2(T) = \frac{\hbar^2}{2m^\star\left|\alpha(T)\right|} = \left(\frac{\Phi_0}{2\sqrt{2}\pi\mu_0 H_c(T)\lambda_{\mathrm{eff}}(T)}\right)^2, \tag{2.29}$$

in one dimension. Here $\Phi_0 = \frac{h}{2e}$ is the quantum mechanical *flux quantum*, and the parameter $\xi(T)$ is called the *coherence length.* The f^3 term is only of the same order of magnitude as f if f is close to 1. Once f has dropped appreciably (e.g. close to the vortex core as described in the next section) the solution to

Eq.(2.28) is an exponential with a characteristic decay length $\xi(T)$. Thus ξ can be interpreted as the length scale on which the wave function ψ can vary significantly.

When the order parameter is allowed to fluctuate, more states become available to the system, and thus the entropy increases considerably. A measure of the temperature region around T_c where fluctuations dominate is given by the *Ginzburg number* [28]:

$$Gi = \frac{1}{2}\left(\frac{k_B T_{c0}}{4\pi\mu_0 H_c(0)^2 \xi(0)^3}\right)^2 \tag{2.30}$$

where the term in the brackets is on the order of the ratio of the thermal energy at the phase transition, $E_{\text{therm}} = k_{\text{B}} T_c$, and the condensation energy $V_{\text{corr}} E_B = V_{\text{corr}} \mu_0 H^2/2$ of a coherence volume $V_{\text{co}} = \frac{4}{3}\pi\xi^3$. If the temperature is close enough to T_c, fluctuations of the order parameter cause the heat capacity to diverge. One can show that the heat capacity must diverge in the Ginzburg-Landau model as $1/\sqrt{T - T_c}$ upon reaching the critical temperature.

3. Vortex Physics

3.1. Type II Superconductors

Having derived the two fundamental length scales λ and ξ we can find an explanation how the magnetic field may penetrate the superconductors microscopically in certain materials – called type II superconductors – while it is completely screened in other materials (type I superconductors). As we have seen, the formation of Cooper pairs produces a net energy gain due to the binding energy, by contrast, the expulsion of the magnetic field by the Meissner effect costs energy. The two effects happen on different length scales: the magnetic field is expelled on the length scale λ_{eff} while ψ changes on the length scale ξ. These length scales are material dependent and can vary strongly between different compounds. If $\xi \gg \lambda_{\mathrm{eff}}$ the energy gain from forming Cooper pairs may exceed the loss from the field expulsion at the boundary surface between normal and superconducting regions. The exact point at which this happens can be expressed with a dimensionless parameter

$$\kappa = \frac{\lambda_{\mathrm{eff}}}{\xi}. \tag{3.1}$$

If this *Ginzburg Landau parameter* exceeds $\kappa_{\mathrm{crit}} = 1/\sqrt{2}$ the formation of a boundary surface produces an energy gain. This was first predicted and analytically discussed by Abrikosov [8]. In the case of a type II superconductor with $\kappa > \kappa_{\mathrm{crit}}$ a field exceeding a critical value of

$$H_{\mathrm{c1}} = \frac{H_c \ln \kappa}{\sqrt{2}\kappa} \tag{3.2}$$

is permitted to penetrate the superconductor in small regions, thus lowering the diamagnetic response of the superconductor.

This field penetration takes place in form of *superconducting vortices*, the shape of $|\psi(\mathbf{r})|$ and the microscopic magnetic field distribution of which we will discuss in the following. The association of an energy gain with a boundary leads to a maximization of the surface area. This is realized by distributing the flux through the superconductor in the form of individual vortices. As the current inside the superconductor is associated with a phase gradient due to Eq. (2.26) and the phase needs to be continuous, the circular super current around the *vortex core* is quantized such that the magnetic flux through the core has a minimum magnitude of Φ_0. On a closed curve around such a core the superconducting wave function changes its phase by 2π. To do so in a continuous manner it needs to be zero in the center of the vortex.

The radial dependence of $|\psi|$ can be approximated by [27]

$$|\psi(r)| \approx |\psi_\infty| \tanh \frac{r}{\xi}. \tag{3.3}$$

The current around the vortex core can be approximately described by the differential equation [27]:

$$\lambda^2 \mathrm{curl}\, \mathbf{j}_s + \mathbf{H} = \hat{z} \frac{\Phi_0}{\mu_0} \delta(\mathbf{r}), \tag{3.4}$$

where $\delta(\mathbf{r})$ is a two dimensional delta function in the x, y-plane and $\hat{z}$ is the unit vector in the z-direction. The solution for the microscopic magnetic field is

$$\mu_0 H(r) = \frac{\Phi_0}{2\pi\lambda^2} K_0 \left(\frac{r}{\lambda}\right), \tag{3.5}$$

where K_0 is a zeroth order Hankel function of imaginary argument. The shapes of $|\psi(r)|$ and $H(r)$ are displayed in Fig. 3.1. This solution is only valid for $r \gg \xi$ as Eqs. (3.4) and (3.3) neglect the extent of the vortex core.

The vortices fill the superconductor homogeneously in order to minimize the macroscopic field gradients.The number of vortices is given by the magnetic flux density B via $N\Phi_0 = \int B \mathrm{d}A$, (where A is the area perpendicular to the field.) When the external field reaches a critical value of

$$H_{\mathrm{c2}} = \frac{\Phi_0}{2\pi\xi^2(T)} = \sqrt{2}\kappa H_c \tag{3.6}$$

the vortex cores start to overlap and the superconductivity breaks down.

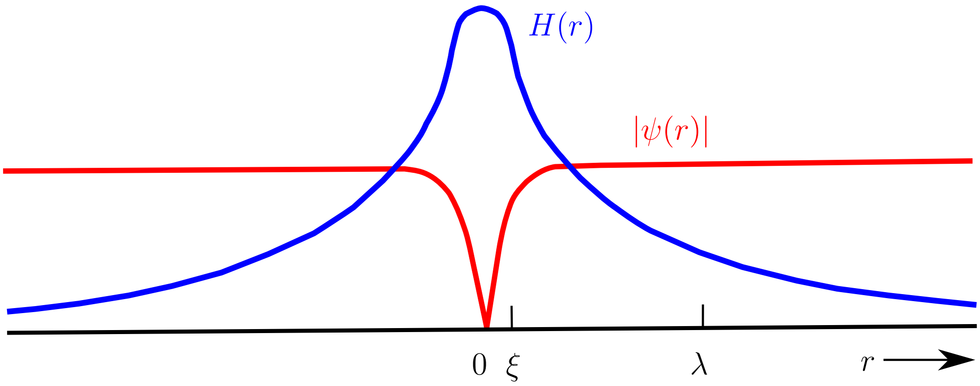

Figure 3.1.: Microscopic magnetic field and superconducting wave function for a single vortex in the high κ approximation (adapted from Ref. [27])

Superconducting vortices behave as magnetic dipoles and repel each other, therefore when the crystal is in thermal equilibrium the vortices will arrange themselves in a lattice in order to maximize the distance between each other. The geometry of this lattice is determined as follows: In high fields $|\psi|^2$ will be reduced enough so that it is justified to drop the non-linear term $\beta |\psi|^2 \psi$ from Eq. (2.24) producing a linearized Ginzburg-Landau equation

$$\left(\frac{\nabla}{i} - \frac{2\pi \mathbf{A}}{\Phi_0}\right)^2 \psi = -\frac{2m^\star \alpha}{\hbar^2}\psi = \frac{\psi}{\xi^2(T)}. \tag{3.7}$$

If there exists an optimal vortex distribution with a minimal energy it is natural to assume that it will show a periodicity. Let H be along the z-axis and we chose the electromagnetic gauge such that $A_y = Hx$, then the solutions of Eq. (3.7) can be put in a general form as discussed by Abrikosov

$$\psi_L = \sum_n C_n \exp\left(inqy\right) \exp\left(-\frac{\left(x - x_n\right)^2}{2\xi^2}\right), \tag{3.8}$$

the solution is periodic in the y-direction, and with $C_{n+\nu} = C_n$ for some ν it is also periodic in the x-direction. Abrikosov showed that the geometry of the vortex lattice depends on the *Abrikosov parameter*

$$\beta_A = \frac{\langle \psi_L^4 \rangle}{\langle \psi_L^2 \rangle^2}, \tag{3.9}$$

where $\langle \dots \rangle$ denotes the average value. The more peaked and less smooth $\psi(\mathbf{r})$ is, the larger β_A becomes. The solution given by Eq. (3.8) has a minimal free energy if the value of β_A is minimal. For triangular lattices $\beta_A \approx 1.16$, while for square lattices $\beta_A \approx 1.18$ and thus the vortices form usually a triangular lattice, although the energy difference is very small and changes from the triangular to the square lattice have been reported in the literature as well [29]. A visualization of such a lattice can be obtained by various techniques that are sensitive to magnetic fields or electronic conductivity. A picture of a lattice in $\mathrm{NbSe_2}$ that was obtained using a scanning tunneling microscope (STM) technique is shown in Fig. 3.2

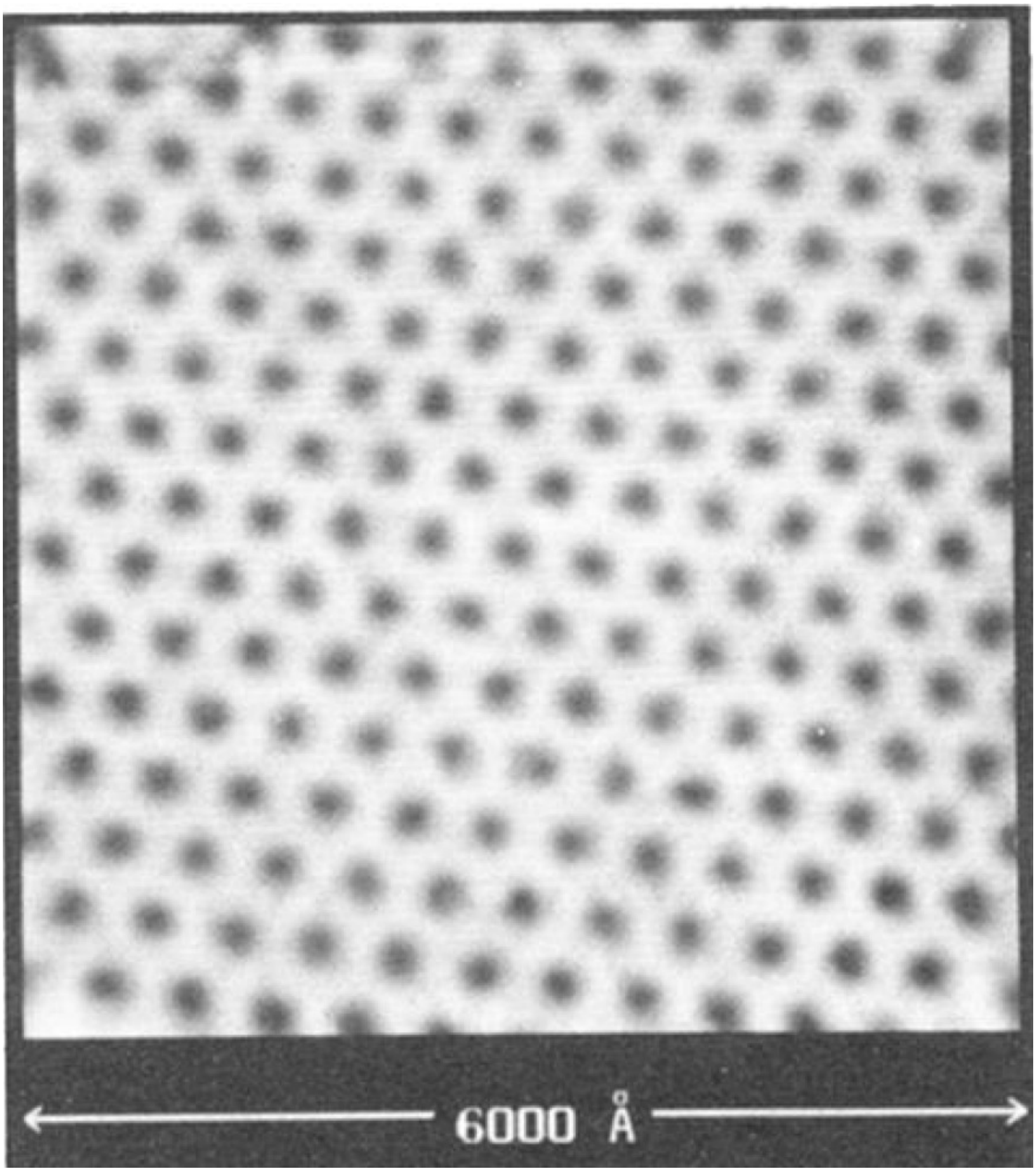

Figure 3.2.: Vortex lattice in $NbSe_2$ observed with STM at 1.8 K in a field of 1 T from Ref. [30]. The lattice has a triangular geometry as discussed in the text.

3.2. Vortex shaking

If there are defects in the crystal lattice of a superconductor, the phonons involved in the Cooper pairing mechanism are disturbed by the defect site, and the energy gain due to the formation of the superconducting state decreases at such a place. A vortex with a low Cooper pair density $|\psi|^2$ in the vortex core that resides at such a defect is in a lower energy state than a vortex in the pure bulk where it takes more energy to suppress the formation of Cooper pairs. It will cost energy to move the vortex out of this position, even when the external field configuration changes – the vortex becomes *pinned*. Due to this pinning, type II superconductors generally show hysteresis when the temperature or the magnetic field are reduced below an *irreversibility line* in the magnetic phase diagram and the pinning gets strong enough to prevent the vortices from thermal depinning. In conventional low-T_c superconductors this irreversibility line is virtually indistinguishable from $H_{c2}(T)$. However in high-T_c superconductors the two lines have been shown to be clearly separate. It has been observed in magnetic torque experiments that this irreversibility line can sometimes be shifted towards lower fields and temperatures by applying a small, oscillating magnetic field in addition to the main field [32]. The explanation of this *vortex shaking* effect was given by Brandt and Mikitik using an extension of the Bean model.

After a magnetic field is applied to a type II superconductor which shows hysteresis, non-equilibrium currents form on the surface causing a non-equilibrium magnetization. When an AC magnetic field is applied perpendicular to the main magnetic field, the two fields sum up, and the vortices are forced to tilt. However, the vortices cannot tilt freely due to the Bean critical currents on the surface of the superconductor. When a vortex tilts, the currents surrounding it must shift as well, but if there is a prevailing non-equilibrium current the shift is not symmetric for the two directions of the AC magnetic field. The most simple case for this discussion is when the main field, the surface currents and the shaking field are all perpendicular to each other inside a thin slab of superconductor. This case is depicted in Fig. 3.3. A thin strip with thickness d, width w, and a critical current density j_c is placed inside a field B_z normal to the strip. We assume that there is a sheet current due to magnetization hysteresis along the sides of the strip with a magnitude $J = jd$. The critical sheet current beyond which the vortices can move freely is $J_c = j_c d$. We discuss the behaviour of a vortex in

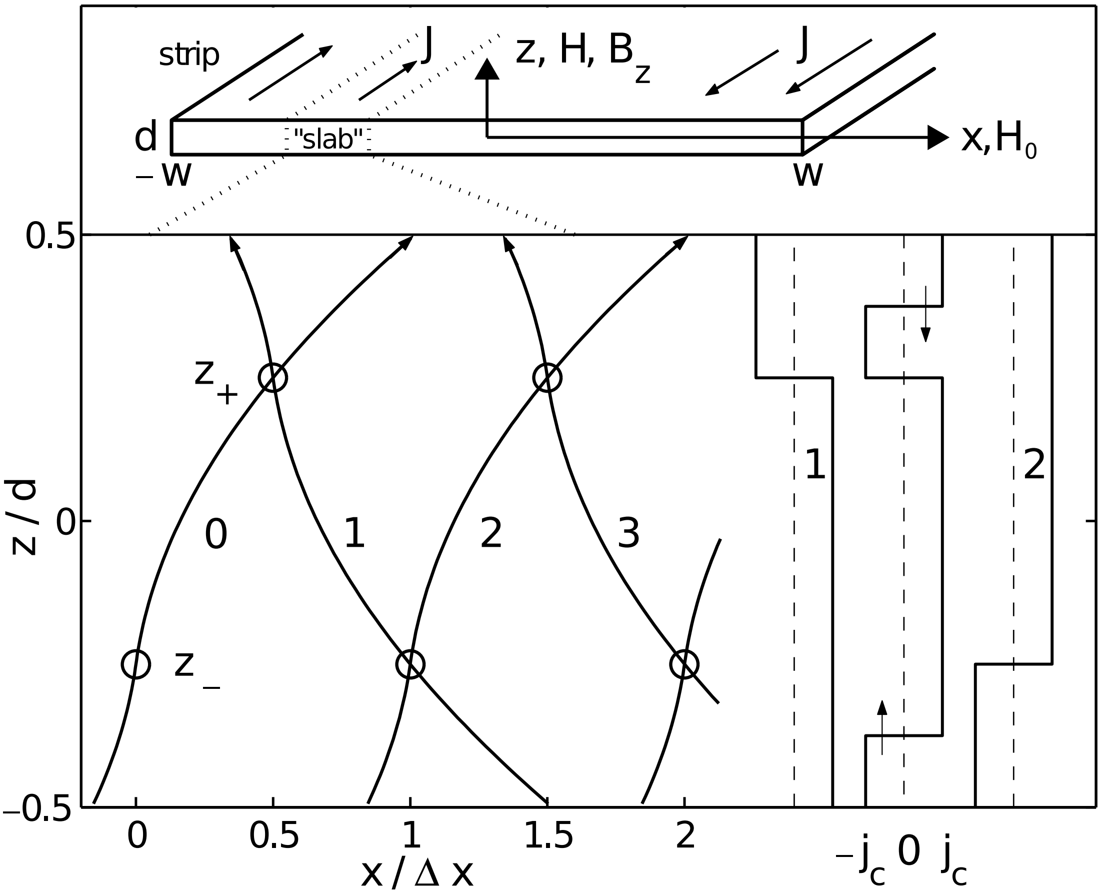

Figure 3.3.: Configuration sketch of transversal vortex lattice "shaking" (taken from Ref. [31]). The top panel shows an infinite strip geometry with a thickness d and a width w, with an indication of the direction of the irreversibility current density J and the direction of the main magnetic field H as well as the "shaking" magnetic field H_0. On the lower left panel a vortex in a short slab is depicted for consecutive half cycles of the shaking field walking further to the right with every half cycle by turning around the circled swivel points. The lower right panel depicts the current profile in the slab for the alternating field directions and for an intermediate situation where the arrow indicates the movement of the current inversion front.

a slab of this strip as depicted in Fig. 3.3. If an oscillating field of magnitude $H_{ac}(t) = H_0 \cos \omega t$ is applied in the x-direction, where

$$\begin{aligned} H_0 >& H_p(J), && (3.10) \\ H_p(J) =& (J_c - |J|)/2, && (3.11) \\ & && (3.12) \end{aligned}$$

the vortex tilts to align with the magnetic field. This is shown for times $t = n/\omega, \ \ n = 0, 1, 2, 3$ in Fig. 3.3 together with the asymmetric Bean-currents forming on the surface of the slab. When the swivel point, around which the vortex is turning, is calculated one finds it for each half cycle in the alternating positions

$$z_+ = -z_- = \frac{J}{2j_c}, \tag{3.13}$$

therefore the vortex moves along the x-direction on each cycle by

$$\Delta x = \frac{2\mu_0 J}{j_c B_z} \left[H - H_p\left(J\right) \right]. \tag{3.14}$$

This causes the vortex to "walk" against the field gradient towards the center of the superconductor until the magnetization is in the thermodynamic (quasi-) equilibrium. Brandt and Mikitik have analyzed this model numerically [31], and obtained an exponential decay of the non-equilibrium magnetization with a characteristic decay time

$$\tau = \frac{w J_c}{0.6386 \omega d \left(2H - J_c\right)}. \tag{3.15}$$

This model can be further extended to include shaking fields with arbitrary orientation [33]. In every case the shaking field causes the current distribution to equilibrate as soon as the minimum field of $H \approx J_c$ is exceeded which is necessary to penetrate the superconductor completely, otherwise a fraction of the vortices does not move and remains in place.

3.3. Observation of vortex lattice melting

It was predicted in 1988 that a vortex lattice might undergo a first-order "melting" transition [34, 35] and turn into a "liquid" at sufficiently high temperatures, but well below the transition to superconductivity. This prediction was subsequently invoked to explain the sudden onset of damping of mechanical oscillators bearing a superconducting sample in a magnetic field [36, 37], hysteresis in the resistivity [38], and neutron-scattering data [21]. The first microscopic detection of vortex lattice melting was done by Lee *et al.* using muon spin rotation studies [39]. The theoretical properties of vortex matter were discussed exhaustively [28, 40, 41], but the existence of a true first-order transition has been of speculative nature until the first strong thermodynamic evidence for it was found in magnetization measurements on $Bi_2Sr_2CaCu_2O_8$ [42, 43]. The measurement of the associated latent heat through specific-heat measurements on $YBa_2Cu_3O_7$ followed soon after [22, 23]. Data of one of these measurements is shown in Fig. 3.4. In the c_p/T vs. T representation a small peak below the superconducting transition indicates a first order phase transition with an associated latent heat. Thermodynamic consistency with magnetization data [44] was demonstrated [22, 45] subsequently. It became clear that high-quality crystals are necessary in order to clearly observe the first-order behaviour, because defects such as twinning boundaries have been shown to drive the transition to glass-like [46]. Many experimental reports in the literature indeed describe second-order or glass-like transitions, the exact nature of which is influenced by the details of vortex pinning in a given sample. Although the nature of the high-temperature ("liquid") phase is essentially unexplored and no direct experimental proofs for the existence of vortices as distinct entities in this phase are available, we will call the phase transition under discussion hereafter "melting transition".

All confirmed measurements of first-order melting transitions have been made on layered cuprates [22, 23, 42–45, 47–53], and they are now theoretically fairly well understood [35, 54, 55]. Following the same theoretical arguments, a temperature-driven phase transition of the vortex lattice should, in principle, also occur in sufficiently clean low-temperature superconductors. However, there are only very few reports on measurements of thermodynamic quantities in the context of vortex-lattice melting in such compounds. For Nb and Nb_3Sn, for example, attempts have been made to measure the melting entropy directly [26, 56], and the absence of a related signal in very pure Nb has led to reflections about the complete absence of vortex-lattice melting in this compound [56]. Nb_3Sn seems to be the only low T_c superconductor with a report of first-order like features in thermodynamic quantities [26], which still awaits an independent experimental

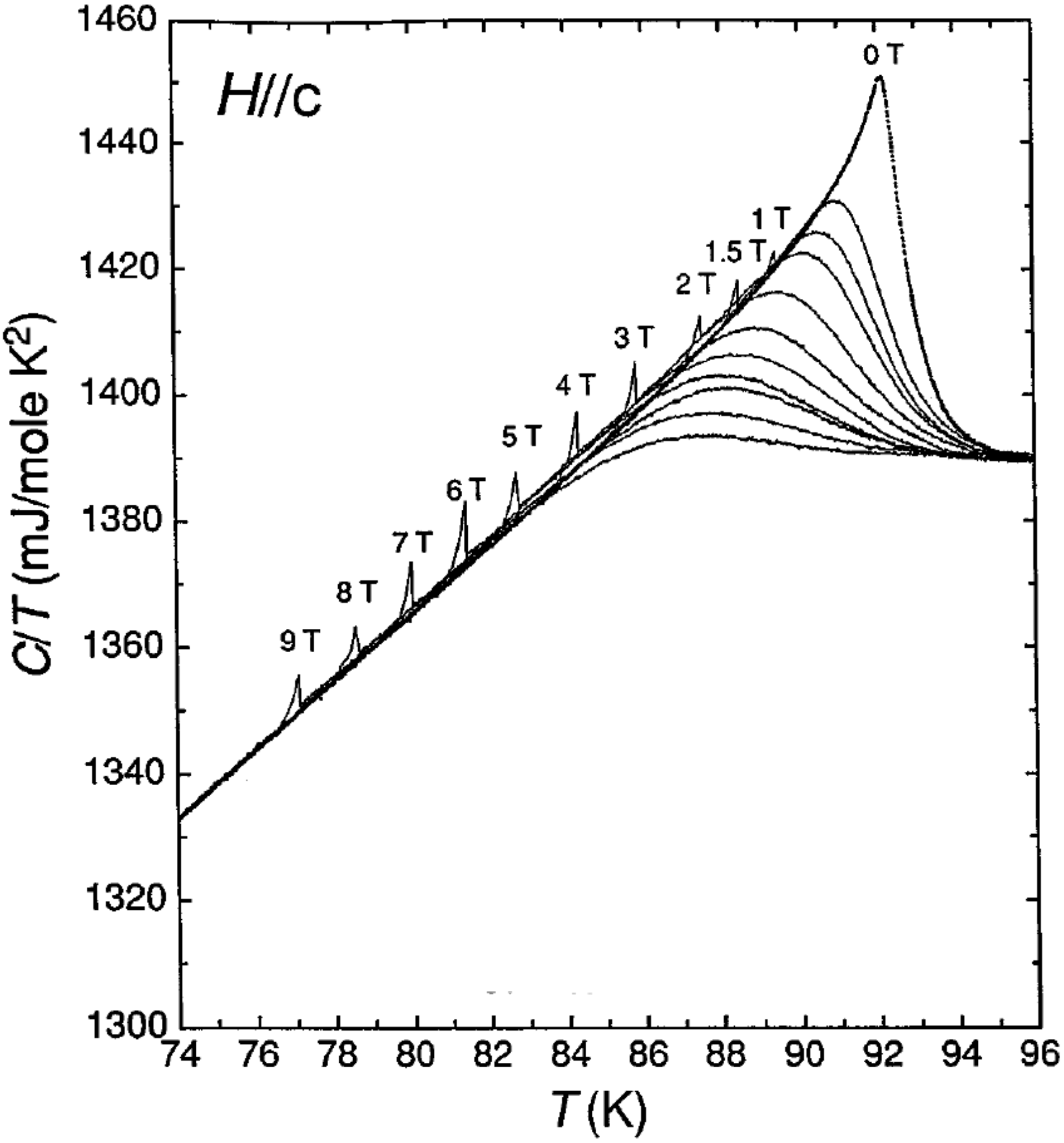

Figure 3.4.: Peaks in the specific heat due to the melting of the vortex lattice in an untwinned $YBa_2Cu_3O_{7-\delta}$ single crystal in different external magnetic fields in parallel to the c-axis. Adapted from Ref. [47].

confirmation, however.

4. Thermodynamics of vortex-lattice melting

In order to quantitatively understand experimental results in the context of vortex lattice melting we derive here explicit estimates for the expected discontinuities in entropy and in magnetization for various type II superconductors. These estimates are based on established theoretical work in the literature about the location of the conjectured vortex-lattice melting lines in the magnetic phase diagram, on Richard's rule [57] to estimate the melting entropy per particle, on the use of the correct "single-vortex length" [58], and on taking the enhancement of the resulting configurational entropy by the strong temperature dependence of relevant model parameters near the upper critical field into account [54, 55]. We conclude that a measurement of the melting entropy and a related discontinuity in the magnetization, if they exist in conventional superconductors, should be feasible on selected compounds using state-of the art techniques provided that vortex pinning is weak enough. The results have been published by us in Ref. [59].

4.1. Basic melting theory

4.1.1. The melting lines

The assumptions of the simplest theory about the melting of the vortex lattice are very similar to a basic melting theory for solids. In 1910, Lindemann introduced a melting criterion [60], based on the idea that melting occurs as soon as the thermal mean-square displacement $\langle u_{\mathrm{th}}^2 \rangle^{1/2}$ of the atoms in a lattice reaches a certain fraction of the lattice constant a, i.e., $\langle u_{\mathrm{th}}^2 \rangle^{1/2} \approx c_L a$ with the Lindemann number $c_L < 1$. This heuristic argument has proved to be reliable, although the value for c_L may vary widely for different crystal systems. Corresponding quantitative calculations for the vortex-lattice melting lines $B_m(T)$ (by comparing a calculated $\langle u_{\mathrm{th}}^2 \rangle^{1/2}$ for vortices with the mean vortex distance $a_0 = \sqrt{\Phi_0/B}$) lead to an implicit equation [35, 61]

$$\frac{t_{\mathrm{m}}}{\sqrt{1-t_{\mathrm{m}}^2}} = \frac{2\pi c_{\mathrm{L}}^2}{Gi^{1/2} b^{1/2} f(b)}\,, \tag{4.1}$$

with $t_m = T_m/T_{c0}$ the reduced melting temperature T_m for $B = B_m$ with respect to the critical temperature T_{c0} in zero magnetic field, $b = B/B_{c2}(T)$ the reduced magnetic induction B with respect to the temperature dependent upper-critical field $B_{c2}(T)$, and $f(b)$ a model-dependent function (see below). The Ginzburg number Gi is a measure for the width of the fluctuation region in zero magnetic field around T_{c0} (see Section 2.4). We consider here an anisotropic uniaxial case in which the external magnetic field is applied along the crystal direction with the smallest upper critical field ("c-axis"). In SI-units, Gi is then defined as

$$Gi = \frac{1}{2}\left(\frac{\mu_0 k_B T_{c0}}{4\pi B_c(0)^2 \varepsilon \xi(0)^3}\right)^2 = \frac{\pi \mu_0^2 k_B^2 T_c^2 \kappa^4}{B_{c2\mathrm{GL}}(0)\varepsilon^2 \Phi_0^3}, \tag{4.2}$$

where $\mu_0 = 4\pi 10^{-7}\,\mathrm{Vs/Am}$ is the permeability of the vacuum, $k_B = 1.38 \cdot 10^{-23}\,\mathrm{J/K}$ is the Boltzmann constant, κ is the Ginzburg-Landau parameter for $B \parallel c$, $\varepsilon < 1$ is the anisotropy parameter, here defined as the ratio of B_{c2} in the c-direction and in a direction perpendicular to it, ξ is the coherence length relevant for $B \parallel c$ (i.e., the "in-plane coherence length"), and $B_c(0)$ and $B_{c2\mathrm{GL}}(0)$ are the thermodynamic and the upper-critical fields within the Ginzburg-Landau theory, respectively, linearly extrapolated from T_{c0} to $T = 0$ K. The assumption of a linear $B_{c2}(T)$ does not account for experimentally determined values of $B_{c2}(0)$ that are often given in the literature, however, and it will not lead to an accurate estimate of the melting lines over the full range of temperatures. Therefore we will assume in the following a relationship of the form

$$B_{c2}(T) = B_{c2}(0)\left(1 - (T/T_{c0})^2\right) \tag{4.3}$$

with $B_{c2\mathrm{GL}}(0) = 2B_{c2}(0)$. The empiric formula (4.3) can be made asymptotically correct for low and high fields by modifying the parameter $B_{c2}(0)$. Any deviation from the simple Eq. (4.3) in a given material can be accounted for, if necessary, by replacing the term $1 - t_m^2$ in Eq. (4.1) by an appropriate formula [35, 61].

The function $f(b)$ in Eq. (4.1) has been first calculated by Houghton, Pelcovits and Sudbø [35] for $\kappa \gg 1$,

$$f_{\mathrm{HPS}}(b) = \left(\frac{1.657}{\sqrt{1-b}} + 1 \right) / (1-b). \tag{4.4}$$

In their original work, a linear $B_{c2}(T)$ was assumed, which we have replaced in Eq. (4.1) by Eq. (4.3). Mikitik and Brandt calculated $f(b)$, again for $\kappa \gg 1$, within a collective pinning theory [61] to

$$f_{\mathrm{MB}}(b) = \frac{2\beta_A}{1-b} \frac{\sqrt{1+(1+c(b))^2}-1}{c(b)(1+c(b))}, \tag{4.5}$$

valid for all values of b throughout the mixed state, with $c(b) = \sqrt{\beta_A(1-b)/2}$ and $\beta_A = 1.16$ the Abrikosov number. The functions $f(b)$ from Eqs. (4.4) and (4.5) only slightly differ between the two approaches. The quantities $f(b)(1-b)^{3/2}$ vary only slowly with b between ≈2.66 for $b = 0$ and ≈1.73 for $b = 1$.

In order to be able to briefly discuss also the important case of an arbitrary κ, it is instructive to consider a simplified version of Eq. (4.1),

$$k_B T_m = A c_{66} c_L^2 a_0^3 \varepsilon \tag{4.6}$$

with the shear modulus c_{66}. To interpret Eq. (4.6) we consider the result of Brandt [62] within a theory of weak collective pinning,

$$c_{66} \approx \frac{B_{c2}(T)^2}{\mu_0} \frac{b(1-b)^2}{8\kappa^2} \left(1 - \frac{1}{2\kappa^2}\right) \left(1 - 0.58b + 0.29b^2\right) \tag{4.7}$$

which was computed for all values of $\kappa > 1/\sqrt{2}$ and b throughout the mixed state. The Eq. (4.6) together with Eq. (4.7) asymptotically coincides in the limit $b \to 0$ with the Houghton, Pelcovits and Sudbø formula (Eqs. (4.1) and (4.4)) for $A \approx 15$ and with that of Mikitik and Brandt (Eq. (4.5)) for $A \approx 17$, and in the limit $b \to 1$ within the same approaches for $A \approx 33$ and $A \approx 31$, respectively, if the Volume $a_0^3\varepsilon$ in Eq. (4.6) is replaced in this limit by V_0 from Eq. (4.14), see below.

The Eqs. (4.6) and (4.7) show in a very transparent way that for a given T_m and $\kappa \to 1/\sqrt{2}$ (i.e., when approaching the type-I limit with $c_{66} \to 0$), the magnetic-flux density $B_m(T)$ approaches zero because $a_0 \to \infty$. In terms of the external magnetic field H, the melting field $H_m(T)$ aligns with the lower-critical field $H_{c1}(T)$ over a wide range of temperatures. In an alternative interpretation of this limit, a $\kappa \to 1/\sqrt{2}$ leads to a decrease of the Lindemann number to an effective value $\tilde{c}_L = c_L(1 - 1/2\kappa^2)^{1/2}$, or, in terms of the Ginzburg number in Eq. (4.1), to an increase of Gi to an effective $\tilde{Gi} = Gi(1 - 1/2\kappa^2)^{-2}$.

In the following we will nevertheless use the melting lines obtained by Mikitik and Brandt [61] for $\kappa \gg 1$ because they are explicitly valid for all values of b and Gi and also allow for a temperature dependence of the upper-critical field according to Eq. (4.3). We choose $c_L = 0.20$ [63], and we will ignore for the moment any possible renormalization of Gi for the limit $\kappa \to 1/\sqrt{2}$, which would only affect Nb and CaC_6 listed in table 4.1.

4.1.2. Distance of B_m from the fluctuation region around B_{c2}

In Fig. 4.1 we illustrate that besides c_L it is mainly the Ginzburg number Gi (which can vary in different superconductors by orders of magnitude, see table 4.1) that determines the distance of the melting line from $B_{c2}(T)$. For most conventional superconductors to be discussed below Gi is small and the melting lines will therefore be close to the upper-critical field. However, even in isotropic superconductors Gi can be large enough so that a vortex-lattice melting transition distinct from $B_{c2}(T)$ might be observed in principle. For this case we have to additionally address the question whether $B_m(T)$ is located outside the critical-fluctuation region around $B_{c2}(T)$ or not. For the case $b \to 1$, which is of interest here, Mikitik and Brandt [61] have estimated the difference

$$\delta B = B_{c2}(T) - B_m(T) \approx \left(\frac{1.78}{2\pi c_{L^2}}\right)^{2/3} B_{c2}(0) t^{2/3} Gi^{1/3} (1 - t^2)^{2/3}. \tag{4.8}$$

The width of the critical-fluctuation region in a magnetic field on the temperature scale, on the other hand, has been estimated to [64]

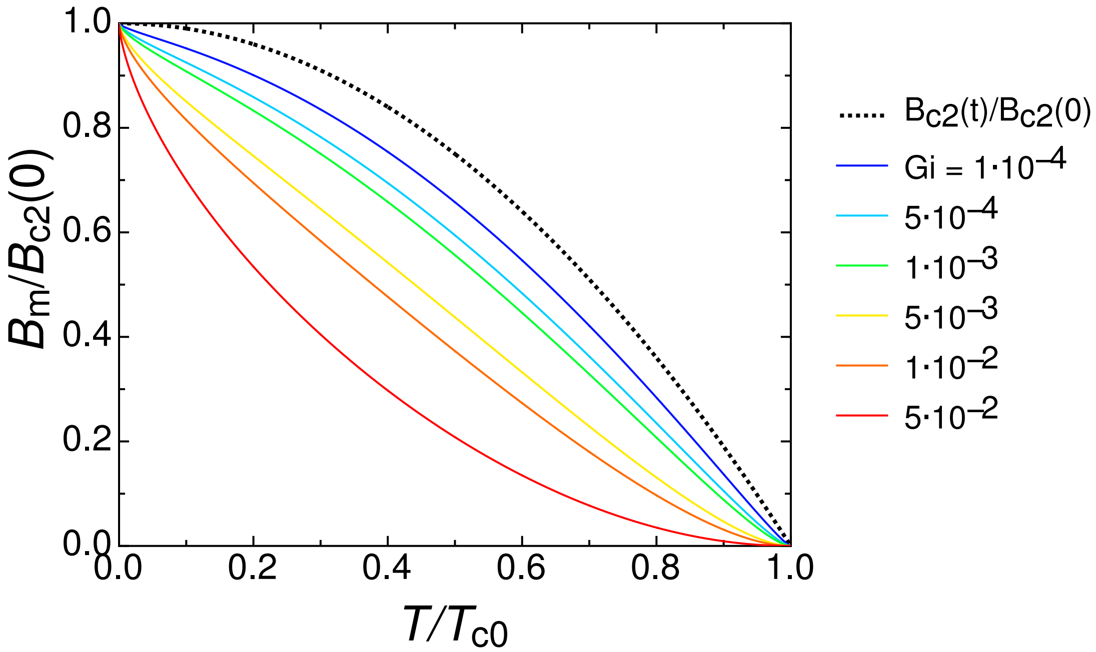

Figure 4.1.: Melting lines (according to Ref. [61] with $c_L = 0.20$) for different values of Gi.

$$\delta T_{\text{fluct}} \approx T_{c2}(B)\, Gi^{1/3} \left(\frac{B}{B_{c2}(0)}\right)^{2/3}, \tag{4.9}$$

where $T_{c2}(B)$ is the inverted $B_{c2}(T)$. The corresponding width in B around $B_{c2}(T)$ is

$$\delta B_{\text{fluct}} \approx \left|\frac{\mathrm{d}B_{c2}}{\mathrm{d}T}\right| \delta T_{\text{fluct}} = 2B_{c2}(0)t^2\, Gi^{1/3}(1-t^2)^{2/3}, \tag{4.10}$$

where we have again made use of Eq. (4.3). The melting line is outside the critical region if $\delta B > \delta B_{\text{fluct}}$, or

$$t < 0.361/c_{\mathrm{L}} \tag{4.11}$$

which is always fulfilled for reasonable values of c_L, notably independently of the value of Gi. A tighter condition, $\delta B > n\delta B_{\text{fluct}}$ with $n > 1$, will modify this criterion to $t < 0.361n^{-3/4}/c_L$, but we may note that a clear first-order transition has been observed in $\mathrm{YBa_2Cu_3O_7}$ up to $t \approx 0.98$ [49].

4.1.3. Discontinuities in entropy and in magnetization

To obtain the melting entropies, we make use of Richard's rule [57] for crystal lattices, in which the configurational melting entropy per particle is assumed to be a constant multiple (or fraction) of k_B. With the volume V_0 occupied by one particle we then have

$$\Delta s_0 V_0 = \eta k_B, \tag{4.12}$$

where Δs_0 is the configurational melting entropy per volume and η is an unknown and yet to be determined constant (see below).

To obtain the elementary volume V_0 for vortices that is relevant for counting the total number of degrees of freedom in the system, it is essential to use the correct "single-vortex length" L_0. This length has often been erroneously taken as the zero-temperature coherence length ξ [26, 56], thereby vastly underestimating it and overestimating Δs_0. Kierfeld and Vinokur [58] calculated L_0 to

$$L_0 = \frac{\varepsilon a_0}{\sqrt{1-b}} \tag{4.13}$$

(which is much larger than ξ,) and the volume V_0 becomes

$$V_0 = \frac{\varepsilon a_0^3}{\sqrt{1-b}} \tag{4.14}$$

which diverges as B approaches the upper-critical field and therefore leads to a substantial reduction of Δs_0 in materials in which the melting lines are located very close to $B_{c2}(T)$.

It turned out that the entropy obtained from applying Richard's rule alone considerably underestimates the measured entropy changes Δs upon vortex-lattice melting both in $\mathrm{YBa_2Cu_3O_7}$ and in $\mathrm{Bi_2Sr_2CaCu_2O_8}$ [54, 55]. Taking the marked temperature dependence of thermodynamic quantities into account, Dodgson *et al.* arrive at an enhancement of Δs_0 of the form [55]

$$\Delta s = \frac{\left[1-\tilde{b}+(2\tilde{b}-t^2)t^2\right]}{(1-t^2-\tilde{b})(1-t^2)}\Delta s_0 \tag{4.15}$$

with $\tilde{b} = B/B_{c2}(0)$. Although calculated in the London approximation, Eq. (4.15) contains corrections to account for the suppression of the order parameter around the vortex cores in the high-field limit $b \to 1$. This enhancement of Δs_0 may be particularly relevant for superconductors with small Gi where $B_{c2}(T) - B_m(T)$ is expected to be small, because it diverges at $B_{c2}(T)$ as $(1-b)^{-1}$ and therefore overcompensates the reduction of Δs_0 due to the diverging elementary vortex volume V_0, and also partly moderates the effect of the reduction of c_{66} on Δs_0 as $B_m(T)$ approaches $B_{c2}(T)$, see Eqs. (4.14) and (4.7). While the $B_m(T)$ line of $YBa_2Cu_3O_7$ itself is, to some extent, also modified by the arguments raised in Ref. [55] because it is located very far from $B_{c2}(T)$ in this particular compound, the $B_m(T)$ in conventional superconductors with small Gi that are under discussion here must remain very close to $B_{c2}(T)$. However, we state that even small errors in estimating $B_m(T)$ may result in substantial uncertainties in Δs (and therefore in ΔM) because these quantities sensitively depend on $(1-b)$. In this sense, the corresponding quantities calculated in the remainder of this chapter have to be taken as order-of-magnitude estimates, rather than as exact results.

In the context of vortex-lattice melting, the constant η in Eq. (4.12) has been estimated to ≈ 0.16 [54] for $YBa_2Cu_3O_7$. At the first order melting transition the heat capacity ideally diverges in the form of a delta function. We saw in Fig. 3.4 that for real measurements this delta function becomes a finite peak on top of the heat capacity curve where Δs corresponds to the area of this peak in the $c_p(T)/T$ vs. T representation. Using the data of Fig. 3.4 we have recalculated $B_m(T)$ and Δs for this compound according to the above rules (Eqs. (4.1), (4.5), (4.12) and (4.15)) with the material parameters from table 4.1 and $c_{\mathrm{L}} = 0.20$, and we obtain the best fit to the Δs data from Ref. [49] for $H \parallel c$ with $\eta = 0.077$ (see Fig. 4.2). To further justify this rather small value, we can use a crude estimate taken to explain Δs in $Bi_2Sr_2CaCu_2O_8$ in Ref. [42], $T_m\Delta s = c_{66}c_{\mathrm{L}}^2$, which, in combination with Eqs. (4.12) and (4.14), yields the correct melting line of Eq. (4.6) with $\eta = 1/A$. For $b \to 0$, we then have $\eta \approx 0.06$ and for $b \to 1$, $\eta \approx 0.03$. It is possible, however, that η assumes entirely different values in materials with lower Gi, and we therefore do not further specify the value of η in our calculations.

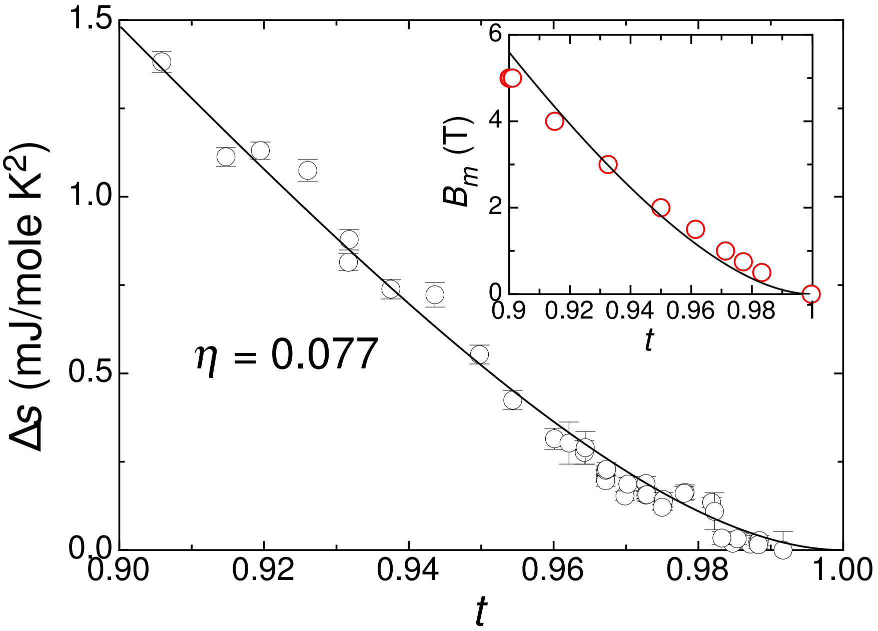

Figure 4.2.: Melting entropy Δs and melting line $B_m(T)$ of $\mathrm{YBa_2Cu_3O_7}$, calculated from the parameters given in table 4.1 and Eqs. (4.1), 4.5, 4.12 and 4.15. The Δs-data fit best for $\eta = 0.077$.

The resulting discontinuities in magnetizations can finally be derived from the Clausius-Clapeyron equation,

$$\Delta s = -\Delta M \frac{\mathrm{d}B_m}{\mathrm{d}T} \tag{4.16}$$

with $\Delta M > 0$, i.e., M increases when crossing $B_m(T)$ from the solid to the "liquid" phase.

It is interesting to note that in the limit $\kappa \to 1/\sqrt{2}$ (i.e., when approaching the type-I limit), c_{66} in Eq. (4.7) vanishes even if the vortex density remains high in large magnetic fields, and so must the discontinuities in s and in M which are related to this energy scale. However, as long as $\kappa > 1/\sqrt{2}$, both Δs and ΔM remain finite even in *isotropic* superconductors with $\varepsilon = 1$ because $B_m(T)$ seems to stay outside the fluctuation region defined by Eq. (4.9) around $B_{c2}(T)$.

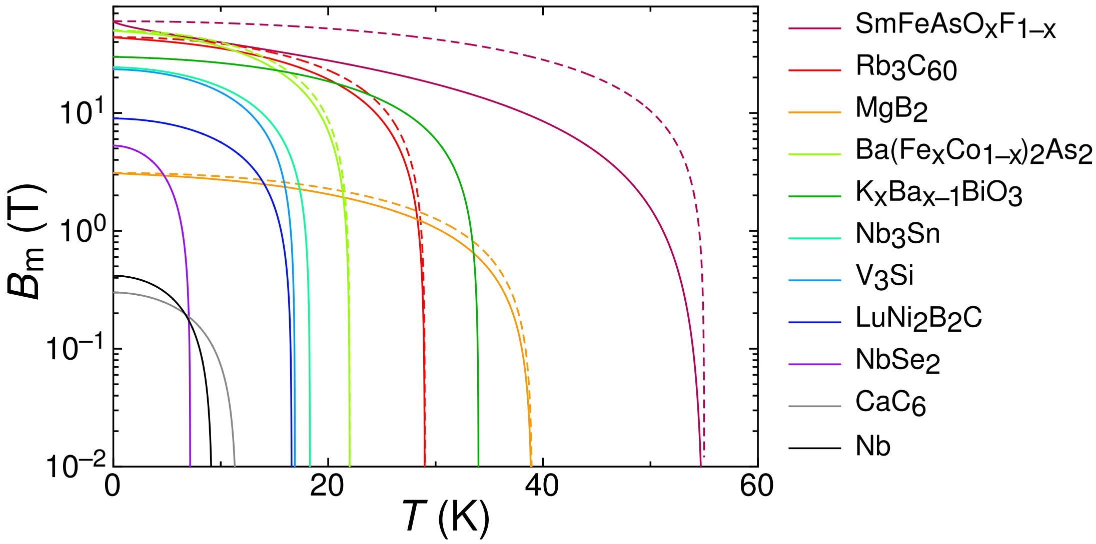

Figure 4.3.: Expected melting lines $B_m(T)$ for various type-II superconductors, calculated from Eqs. (4.1) and (4.5) with $c_L = 0.20$ and the material parameters given in table 4.1 (solid lines). The $B_{c2}(T)$-lines (dotted lines) have been plotted only for SmFeAsO$_x$F$_{1\text{-x}}$, Rb$_3$C$_{60}$, MgB$_2$, and Ba(Fe$_x$Co$_{1\text{-x}}$)$_2$As$_2$ for which they appear distinct from $B_m(T)$ in this representation.

4.2. Application to real materials

In order to estimate the order of magnitude of the discontinuities in entropy Δs and in magnetization ΔM in real superconductors, we have compiled literature values of relevant material parameters for a number of superconductors of contemporary interest (see Table 4.1). We have then calculated the melting lines $B_m(T)$ according to Eqs. (4.1) and (4.5) with $c_L = 0.20$ (see Fig. 4.3).

In the Figs. 4.5-4.7 we have plotted the expected values for Δs and ΔM (where we tentatively took the enhancement from Eq. (4.15) into account, but ignoring a possible influence on B_m and Δs for the limit $\kappa \to 1/\sqrt{2}$), together with δT and δB, the distances of the melting lines from $B_{c2}(T)$ in T and in B, respectively. In Fig. 4.8, we also show a corresponding calculation for Δs vs. T without the factor from Eq. (4.15) for comparison with Fig. 4.5a, to illustrate the impact of this correction on the order of magnitude of Δs.

Table 4.1.: Literature values for relevant material parameters of various type-II superconductors

Substance	T_{c0} [K]	$B_{c2}(0)$ [T]	κ	ε	Gi	References
$SmFeAsO_xF_{1\text{-}x}$	55	60	99	0.125	$1.66 \cdot 10^{-2}$	[65]
$YBa_2Cu_3O_7$	92	120	65	0.125	$4.96 \cdot 10^{-3}$	[47, 66, 67]
Rb_3C_{60}	29	44	90	1	$6.70 \cdot 10^{-5}$	[68]
MgB2	39.0	3.1	11	0.097	$4.08 \cdot 10^{-5}$	[69, 70]
$Ba(Fe_{1\text{-}x}Co_x)_2As_2$	22	50	66	0.666	$2.16 \cdot 10^{-5}$	[71]
$K_xBa_{1\text{-}x}BiO_3$	34.0	30	36	1	$3.46 \cdot 10^{-6}$	[72]
Nb_3Sn	18.3	24.5	34	1	$9.77 \cdot 10^{-7}$	[73, 74]
V_3Si	16.9	23.5	22	1	$1.52 \cdot 10 - 7$	[73, 75, 76]
$LuNi_2B_2C$	16.6	9.0	13	0.75	$8.31 \cdot 10^{-8}$	[77–79]
NbSe2	7.16	5.3	11	0.31	$7.88 \cdot 10^{-8}$	[80, 81]
CaC_6	11.5	0.3	2.1	0.37	$3.35 \cdot 10^{-9}$	[82, 83]
Nb	9.22	0.416	2.2	1	$2.56 \cdot 10^{-10}$	[84, 85]

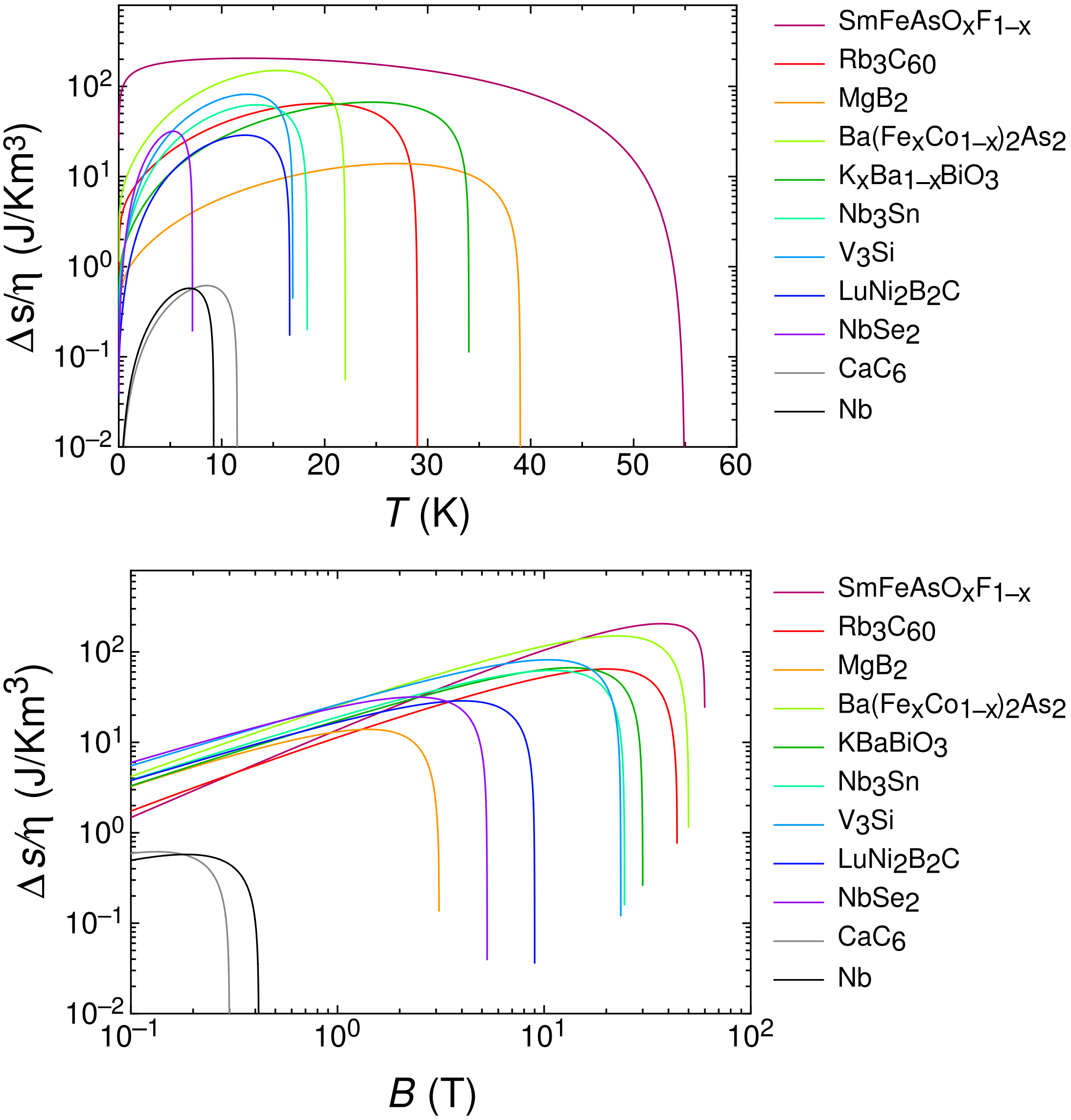

Figure 4.4.: Vortex-lattice melting entropies $\Delta s/\eta$ for various type-II superconductors at the $B_m(T)$ shown in Fig. 4.3, a) as a function of T and b) as a function of B.

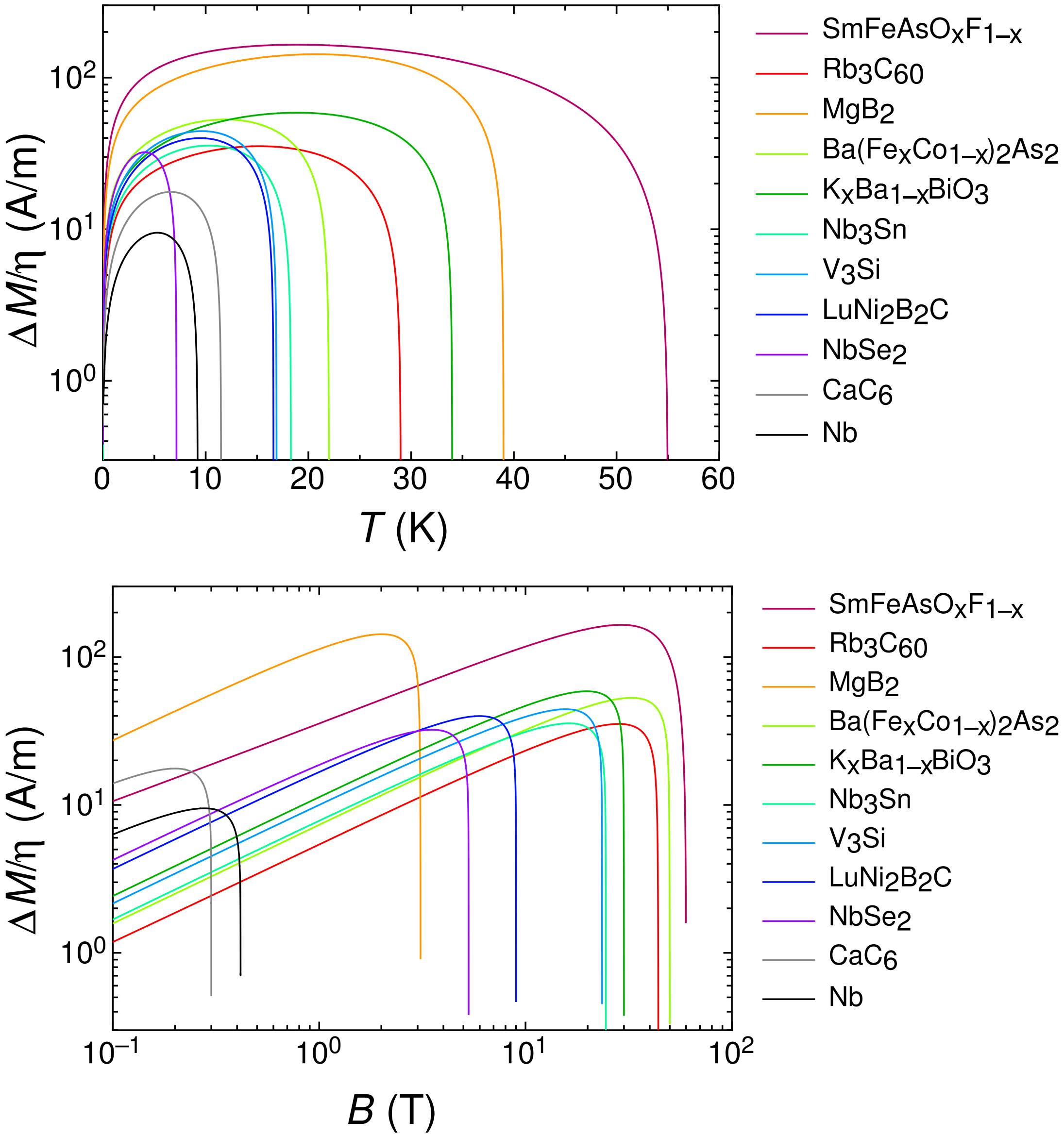

Figure 4.5.: a) Discontinuities $\Delta M/\eta$ in magnetization at the $B_m(T)$ of the materials under discussion, a) as a function of T and b) as a function of B. To convert the given ΔM values from SI into cgs units, the corresponding SI-values have to be multiplied with 10^{-3} to obtain ΔM, and with $4\pi 10^{-3}$ to obtain $4\pi\Delta M$ in Gauss.

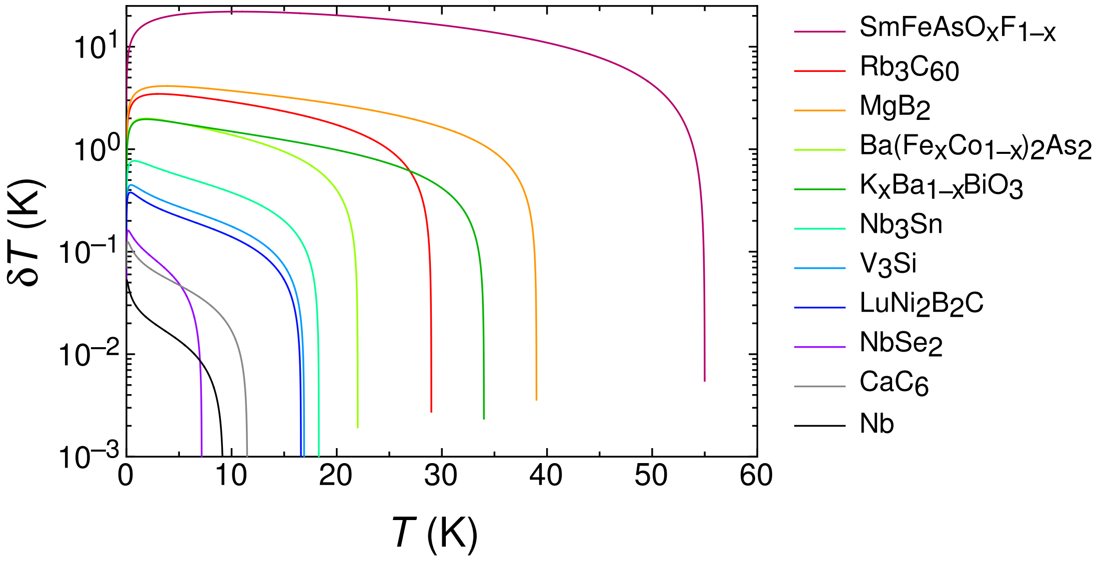

Figure 4.6.: Distances δT of the melting temperatures T_m from T_{c2} in experiments with fixed magnetic-flux density B.

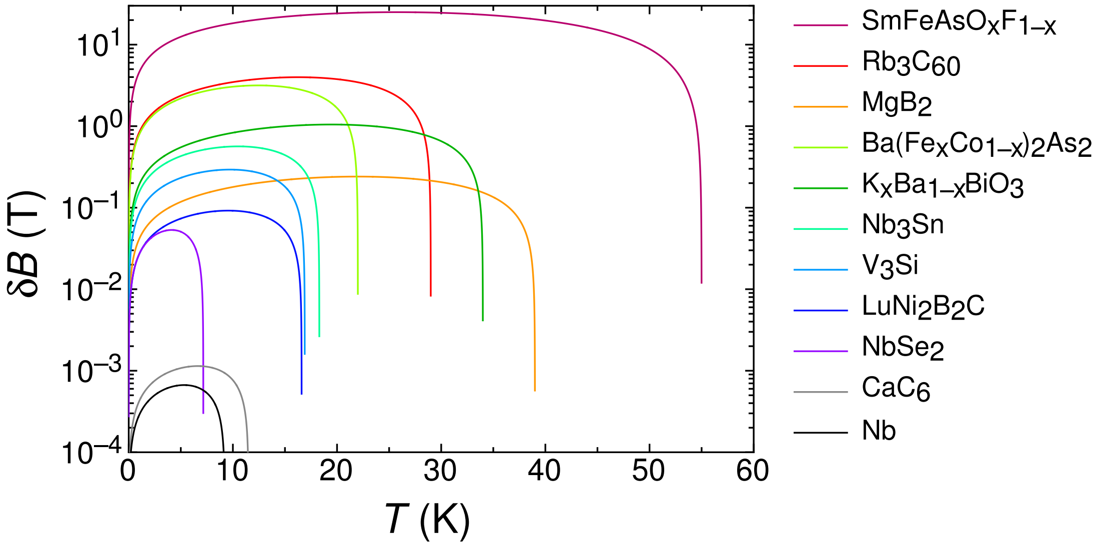

Figure 4.7.: Difference $\delta B = B_{c2}(T) - B_m(T)$ in experiments with constant temperature T.

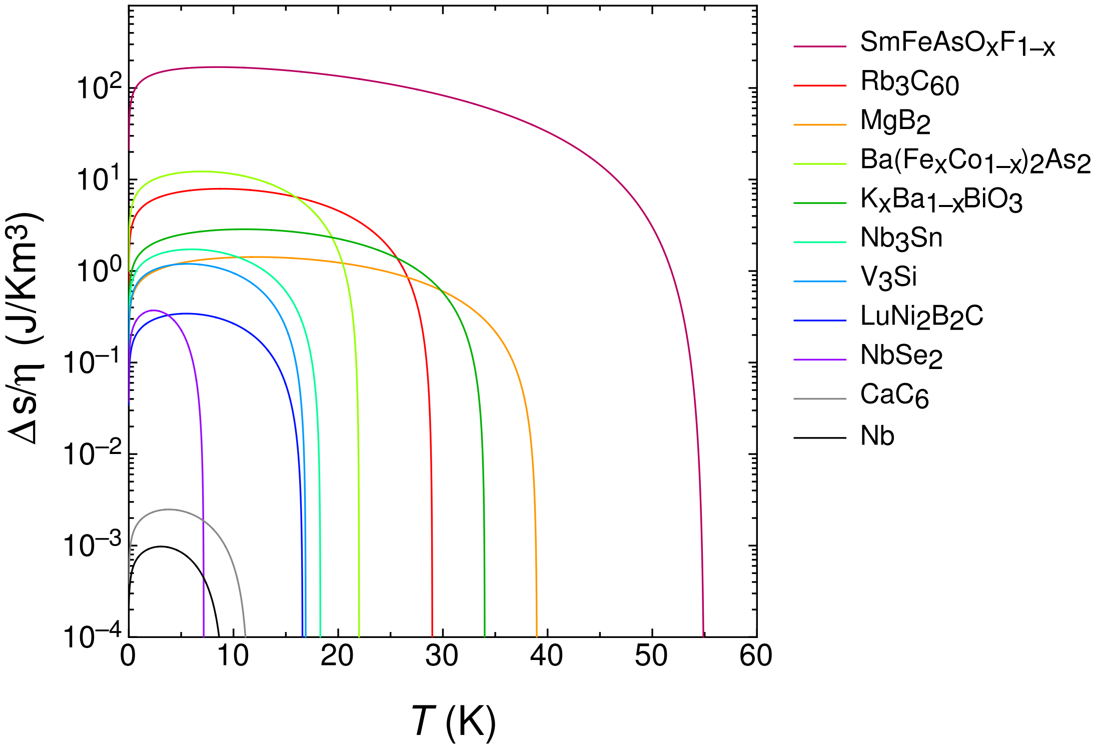

Figure 4.8.: Vortex-lattice melting entropies $\Delta s/\eta$ calculated as in Fig. 4.5a, but without the enhancement given by Eq. (4.15) taken into account.

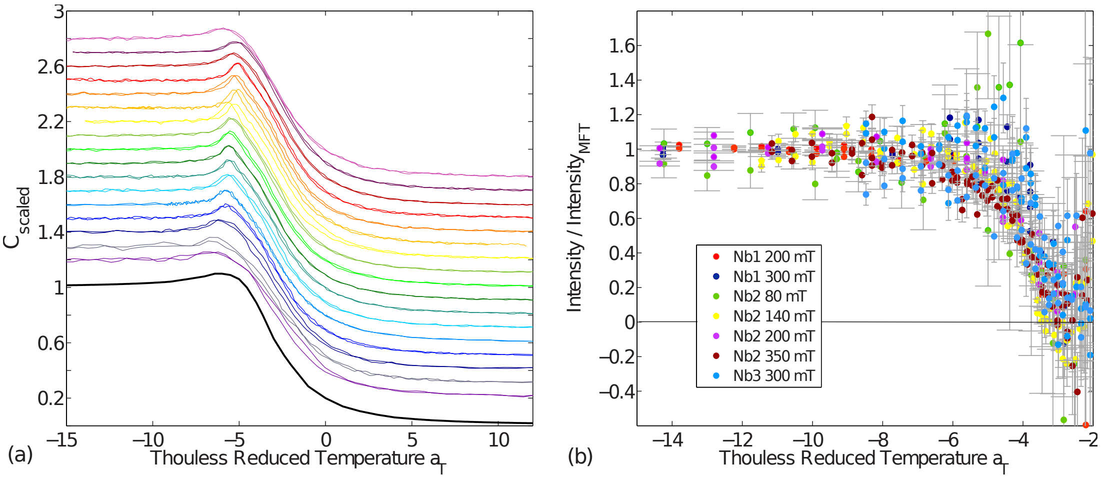

Figure 4.9.: a) Normalized heat capacity data of Nb b) Small angle neutron scattering (SANS) data on the same sample (both reproduced from Ref. [56])

4.2.1. Resolvability in heat capacity and magnetization measurements

As expected, the discontinuities in Δs and ΔM are largest in compounds with a high critical temperature T_{c0} and a large Gi. The maximum possible values for the discontinuities Δs vary by more than two orders of magnitude between the different substances, and they are commonly attained around approximately $B \approx B_{c2}(0)/2$ (see Fig. 4.4b). The smallest Δs and ΔM values can be expected in low-T_{c0}, low-Gi materials such as Nb and CaC$_6$. Moreover, the latter materials show also low κ values on the order of unity, and they may therefore suffer from an additional reduction of Δs and ΔM as discussed above.

Nevertheless, even with a conservative estimate $\eta \approx 0.03$ and taking a reduction of the form $1 - 1/2\kappa^2$ into account, we obtain for the maximum possible Δs in Nb $\approx 16\ \mathrm{mJ/Km^3}$, which should still be within reach of state-to the art calorimeters [56]. In this context we would like to mention that in Ref. [56], a marked narrowing of the expected fluctuation peak in the heat-capacity $C(T, B)$ data of Nb near $T_{c2}(B)$ has been observed (see Fig. 4.9a), with a $C(T, B)$ that clearly exceeds the Thouless theoretical prediction [86] to explain the fluctuation contribution to the heat capacity, and notably in a field range where we find Δs to be maximum (around $B \approx 200\,\mathrm{mT}$, see Fig. 4.4b). A clear drop a few mK below $T_{c2}(B)$ of the diffracted intensity in corresponding small-angle neutron scattering (SANS) experiments (see Fig. 4.9b, a quantity which is related to the magnetization M [56]), might be closely related to that anomalous behavior because both thermodynamic quantities M and C can be derived from the same Gibb's potential $G(T, H)$. The narrowing and enhancement of the heat capacity beyond standard expectations have been explained in Ref. [56] as possibly stemming from either fluctuation contributions that are not accounted for in Thouless' original theory, or from a coupling of the vortex system to the crystal lattice, while the sharp drop in intensity (i.e., the sudden increase in M with increasing T) remained unexplained. It is conceivable that the observed heat-capacity contribution in excess to standard fluctuation theory is, along with the increase in M, in fact related to the missing vortex-melting entropy. A rough estimate of the excess entropy based on the $C(T, B)$ data presented in Ref. [56] is at least in line with the order of magnitude that we have calculated for Δs.

For Nb_3Sn, distinct peaks in $C(T, B)$ have been reported to occur in certain range of magnetic fields and for temperatures T near $T_{c2}(B)$ [26], which appeared only with the aid of an additional externally applied "shaking" magnetic field. Such "shaking" techniques have been very successful to reveal the ΔM in $YBa_2Cu_3O_7$ [87] because they help the vortex lattice to come to an equilibrium state as discussed in Section 3.2. The related magnetocaloric experiments on Nb_3Sn yield an estimate of $\Delta s \approx 2\,\mathrm{mJ/g\text{-}at\ K} \approx 180\,\mathrm{J/Km^3}$ in $B = 7\,\mathrm{T}$, while the published $C(T, B)$ data suggest a $\Delta s \approx 0.3$ mJ/g-at K $\approx 27\,\mathrm{J/Km^3}$ in $B = 6\,\mathrm{T}$ [26]. Inspecting our Fig. 4.4b we estimate that under these conditions and with $\eta \approx 0.06$, $\Delta s \approx 4\,\mathrm{J/Km^3}$ at most, which is much smaller than what has been reported in Ref. [26]. We have to state, however, that Nb_3Sn shows a particularly strong "peak-effect" near $T_{c2}(B)$ that becomes even more pronounced upon "vortex-shaking", with a very sharp onset as T is increased towards $T_{c2}(B)$ [88]. This peak-effect is believed to be a manifestation of enhanced vortex pinning right below the upper critical field, and the vortex lattice is therefore expected to be prone to disorder and non-equilibrium effects as well as artifacts in the heat capacity measurements as described in Section 6.4.2.

The order-of magnitude estimates that we have calculated for the magnetization discontinuities, $\Delta M/\eta \approx 10\,\mathrm{A \cdot m^{-1}}$ to $150\,\mathrm{A \cdot m^{-1}}$ (with $\eta \approx 0.06$, $4\pi\Delta M \approx 8\,\mathrm{mG}$ to $110\,\mathrm{mG}$ in cgs units) are small, but should still be within the sensitivity specifications of commercial SQUID magnetometers. Nevertheless, unlike the heat capacity which is a measure of a bulk property of the vortex lattice (i.e., probing the total magnetic flux density B), the magnetization M very is sensitive to tiny variations in B because $\mu_0 M = B - \mu_0 H$ and usually $|\mu_0 M| \ll B$. While non-equilibrium effects due to vortex pinning may change the total flux density B only slightly, they can have disastrous consequences on attempts to measure the tiny equilibrium $\Delta M < |M| \ll B/\mu_0$.

4.2.2. Hindrances to experimental detection

In the above approach to obtain reasonable estimates for the expected melting entropies Δs and the associated discontinuities in magnetization ΔM we have deliberately ignored vortex pinning, although such an effect, if strong enough, can make a reliable measurement impossible because thermodynamic equilibrium is not reached on laboratory time scales. In addition, strong pinning makes the identification of the thermodynamic melting line $B_m(T)$ very difficult [89]. Moreover, we have not considered other possible peculiarities in the B-T phase diagrams, such as a dimensional crossover as observed in the cuprates [90], which would affect the occurrence of a first-order melting transition of the vortex lattice as well. We have also made assumptions that should be further backed up by theory. It should in particular be clarified to what extent the enhancement of the configurational entropy Δs_0 near $B_{c2}(T)$ in Eq. (4.15) is really applicable in conventional superconductors. Without such an enhancement (see Fig. 4.8) both the expected Δs and ΔM can be significantly smaller (by up to two orders of magnitude) than the above estimates (see Fig. 4.5) and may fall beyond the detection limit of an experiment.

Physica C 483 (2012) 201–206

Contents lists available at SciVerse ScienceDirect

Physica C

journal homepage: www.elsevier.com/locate/physc

Estimates for the thermodynamic signatures of vortex-lattice melting in conventional superconductors

O. Bossen [*], A. Schilling

Physik-Institut der Universität Zürich, Winterthurerstrasse 190, 8057 Zürich, Switzerland

ARTICLE INFO

Article history:
Received 17 July 2012
Accepted 30 August 2012
Available online 12 September 2012

Keywords:
Vortex lattice melting
Phase transition
HTSC
LTSC
Flux line lattice melting

ABSTRACT

The first-order nature of the vortex-lattice melting transition in copper-based layered high-T_c superconductors is well established. The associated discontinuities in magnetization have been extensively studied, for example, in $YBa_2Cu_3O_7$ [1,2] and $Bi_2Sr_2CaCu_2O_8$ [3], while the respective latent heats have been systematically investigated only in $YBa_2Cu_3O_7$ and related compounds [4–13]. The apparent absence of such signatures in conventional superconductors such as Nb raises the question whether or not the concept of vortex-lattice melting is applicable at all in such materials [14]. Based on available literature to describe the vortex-state and using the Lindemann criterion, we estimate quantitatively the order of magnitude for the expected latent heats of melting and the associated discontinuities in magnetization, respectively, as functions of a few known material parameters. It turns out that both thermodynamic quantities are not strictly vanishing even in isotropic materials as long as $\kappa > 1/\sqrt{2}$, but they are small and may often be beyond the available experimental resolution.

1. Introduction

In 1957 Abrikosov wrote his seminal work [15] on two distinctly different types of superconductors. He predicted that in so-called type II superconductors, an external magnetic field penetrates a superconductor in form of magnetic flux lines which arrange themselves in a regular lattice, each one carrying one magnetic flux quantum $\Phi_0 = 2.07 \times 10^{-15}$ Vs. It was conjectured later that this lattice might undergo some kind of first-order "melting" transition [16,17] and turn into a "liquid" at sufficiently high temperatures, but well below the transition to superconductivity. This prediction was subsequently invoked to explain the sudden onset of damping of mechanical oscillators bearing a superconducting sample in a magnetic field [18,19], hysteresis in the resistivity [20] and neutron-scattering data [21]. The theoretical properties of vortex matter were discussed exhaustively [22–24], but the existence of a true first-order transition has been of speculative nature until the first strong thermodynamic evidence for it was found in magnetization measurements on $Bi_2Sr_2CaCu_2O_8$ [3,25]. The measurement of the associated latent heat through specific-heat measurements on $YBa_2Cu_3O_7$ followed soon after [4,10], and thermodynamic consistency with magnetization data [1] was demonstrated [2,4]. It became clear that high-quality crystals are necessary in order to clearly observe the first-order behaviour, because defects such as twinning boundaries have been shown to suppress the transition and render it to second order [10], presumably because they lead to a glass-like phase [26]. Many experimental reports in the literature indeed describe second-order or glass-like transitions, the exact nature of which is influenced by the details of vortex pinning in a given sample. Although the nature of the high-temperature ("liquid") phase is essentially unexplored and no direct experimental proofs for the existence of vortices as distinct entities in this phase are available, we will call the phase transition under discussion hereafter "melting transition".

All confirmed measurements of first-order melting transitions have been made on layered cuprates [1–8,10,11,25,27,28], and they are now theoretically fairly well understood [17,29,30]. Following the same theoretical arguments, a temperature-driven phase transition of the vortex lattice should, in principle, also occur in sufficiently clean low-temperature superconductors. However, there are only very few reports on measurements of thermodynamic quantities in the context of vortex-lattice melting in such compounds. For Nb and Nb_3Sn, for example, attempts have been made to measure the melting entropy directly [14,31], and the absence of a related signal in very pure Nb has led to reflections about the complete absence of vortex-lattice melting in this compound [14]. Nb_3Sn seems to be the only low T_c superconductor with a report of first-order like features in thermodynamic quantities [31], which still awaits an independent experimental confirmation, however.

In order to quantitatively understand such experimental results we derive here explicit estimates for the expected discontinuities in entropy and in magnetization for various

---

[*] Corresponding author. Tel.: +41 446355778; fax: +41 446355704.
E-mail address: obossen@physik.uzh.ch (O. Bossen).

0921-4534/$ - see front matter © 2012 Elsevier B.V. All rights reserved.
http://dx.doi.org/10.1016/j.physc.2012.08.005

type-II superconductors. These estimates are based on established theoretical work in the literature about the location of the conjectured vortex-lattice melting lines in the magnetic phase diagram, on Richard's rule [32] to estimate the melting entropy per particle, on the use of the correct "single-vortex length" [33], and on taking the enhancement of the resulting configurational entropy by the strong temperature dependence of relevant model parameters near the upper critical field into account [29,30]. We conclude that a measurement of the melting entropy and a related discontinuity in the magnetization, if they exist in conventional superconductors, should be feasible on selected compounds using state-of-the art techniques provided that vortex pinning is weak enough.

2. Basic melting theory

2.1. The melting lines

The assumptions of the simplest theory about the melting of the vortex lattice are very similar to a basic melting theory for solids. In 1910, Lindemann introduced a melting criterion [34], based on the idea that melting occurs as soon as the thermal mean-square displacements $\langle u_{th}^2\rangle^{1/2}$ of the atoms in a lattice reaches a certain fraction of the lattice constant a, i.e., $\langle u_{th}^2\rangle^{1/2} \approx c_L a$ with the Lindemann number $c_L < 1$. This heuristic argument has proved to be reliable, although the value for c_L may vary widely for different crystal systems. Corresponding quantitative calculations for the vortex-lattice melting lines $B_m(T)$ (by comparing a calculated $\langle u_{th}^2\rangle^{1/2}$ for vortices with the mean vortex distance $a_0 = \sqrt{\Phi_0/B}$) lead to an implicit equation [17,35]

$$\frac{t_m}{\sqrt{1-t_m^2}} = \frac{2\pi c_L^2}{Gi^{1/2} b^{1/2} f(b)}, \tag{1}$$

with $t_m = T_m/T_{c0}$ the reduced melting temperature T_m for $B = B_m$ with respect to the critical temperature T_{c0} in zero magnetic field, $b = B/B_{c2}(T)$ the reduced magnetic induction B with respect to the temperature dependent upper-critical field $B_{c2}(T)$, and $f(b)$ a model-dependent function (see below). The Ginzburg number Gi is a measure for the width of the fluctuation region in zero magnetic field around T_{c0}. We consider here a uniaxial case in which the external magnetic field is applied along the crystal direction with the smallest upper critical field ("c-axis"). In SI-units, Gi is then defined as

$$Gi = \frac{1}{2}\left(\frac{\mu_0 k_B T_{c0}}{4\pi B_c(0)^2 \varepsilon \xi(0)^3}\right)^2 = \frac{\pi \mu_0^2 k_B^2 T_c^2 \kappa^4}{B_{c2GL}(0)\varepsilon^2 \phi_0^3}, \tag{2}$$

where $\mu_0 = 4\pi \times 10^{-7}$ Vs/Am is the permeability of the vacuum, $k_B = 1.38 \times 10^{-23}$ J/K is the Boltzmann constant, κ is the Ginzburg–Landau parameter for $B//c$, $\varepsilon < 1$ is the anisotropy parameter, here defined as the ratio of B_{c2} in the c-direction and in a direction perpendicular to it, ξ is the coherence length relevant for $B//c$ (i.e., the "in-plane coherence length"), and $B_c(0)$ and $B_{c2GL}(0)$ are the thermodynamic and the upper-critical fields within the Ginzburg–Landau theory, respectively, linearly extrapolated from T_{c0} to $T = 0$ K. The assumption of a linear $B_{c2}(T)$ does not account for experimentally determined values of $B_{c2}(0)$ that are often given in the literature, however, and it will not lead to an accurate estimate of the melting lines over the full range of temperatures. Therefore we will assume in the following a relationship of the form

$$B_{c2}(T) = B_{c2}(0)(1-(T/T_{c0})^2) \tag{3}$$

with $B_{c2GL}(0) = 2B_{c2}(0)$. The empiric formula (3) can be made asymptotically correct for low and high fields by modifying the parameter $B_{c2}(0)$. Any deviation from the simple Eq. (3) in a given material can be accounted for, if necessary, by replacing the term $1 - t_m^2$ in Eq. (1) by an appropriate formula [17,35].

The function $f(b)$ in Eq. (1) has been first calculated by Houghton et al. [17] for $\kappa \gg 1$,

$$f_{HPS}(b) = \left(\frac{1.657}{\sqrt{1-b}} + 1\right)/(1-b). \tag{4}$$

In their original work, a linear $B_{c2}(T)$ was assumed, which we have replaced in Eq. (1) by Eq. (3). Mikitik and Brandt calculated $f(b)$, again for $\kappa \gg 1$, within a collective pinning theory [35] to

$$f_{MB}(b) = \frac{2\beta_A}{1-b} \frac{\sqrt{1+(1+c(b))^2}-1}{c(b)(1+c(b))}, \tag{5}$$

valid for all values of b throughout the mixed state, with $c(b) = \sqrt{\beta_A(1-b)/2}$ and $\beta_A = 1.16$ the Abrikosov number. The functions $f(b)$ from Eqs. (4) and (5) only slightly differ between the two approaches. The quantities $f(b)(1-b)^{3/2}$ vary only slowly with b between ≈2.66 for $b = 0$ and ≈1.73 for $b = 1$.

In order to be able to briefly discuss also the important case of an arbitrary κ, it is instructive to consider a simplified version of Eq. (1),

$$k_B T_m = A c_{66} c_L^2 a_0^3 \varepsilon, \tag{6}$$

with the shear modulus c_{66}. To interpret Eq. (6) we consider the result of Brandt [36] within a theory of weak collective pinning,

$$c_{66} \approx \frac{B_{c2}(T)^2}{\mu_0} \frac{b(1-b)^2}{8\kappa^2}\left(1 - \frac{1}{2\kappa^2}\right)(1 - 0.58b + 0.29b^2), \tag{7}$$

which was computed for *all* values of $\kappa > 1/\sqrt{2}$ and b throughout the mixed state. The Eq. (6) together with Eq. (7) asymptotically coincides in the limit $b \to 0$ with the Houghton, Pelcovits and Sudbø formula (Eqs. (1) and (4)) for $A \approx 15$ and with that of Mikitik and Brandt (Eq. (5)) for $A \approx 17$, and in the limit $b \to 1$ within the same approaches for $A \approx 33$ and $A \approx 31$, respectively, if the Volume $a_0^3\varepsilon$ in Eq. (6) is replaced in this limit by V_0 from Eq. (14), see below.

The Eqs. (6) and (7) show in a very transparent way that for a given T_m and $\kappa \to 1/\sqrt{2}$ (i.e., when approaching the type-I limit with $c_{66} \to 0$), the magnetic-flux density $B_m(T)$ approaches zero because $a_0 \to \infty$. In terms of the external magnetic field H, the melting field $H_m(T)$ aligns with the lower-critical field $H_{c1}(T)$ over a wide range of temperatures. In an alternative interpretation of this limit, a $\kappa \to 1/\sqrt{2}$ leads to a decrease of the Lindemann number to an effective value $\tilde{c}_L = c_L(1 - 1/2\kappa^2)^{1/2}$, or, in terms of the Ginzburg number in Eq. (1), to an increase of Gi to an effective $\widetilde{Gi} = Gi(1 - 1/2\kappa^2)^{-2}$.

In the following we will nevertheless use the melting lines obtained by Mikitik and Brandt [35] for $\kappa \gg 1$ because they are explicitly valid for all values of b and Gi and also allow for a temperature dependence of the upper-critical field according to Eq. (3). We choose $c_L = 0.20$ [37], and we will ignore for the moment any possible renormalization of Gi for the limit $\kappa \to 1/\sqrt{2}$, which would only affect Nb and CaC_6 listed in Table 1.

2.2. Distance of B_m from the fluctuation region around B_{c2}

In Fig. 1 we illustrate that besides c_L it is mainly the Ginzburg number Gi (which can vary in different superconductors by orders of magnitude, see Table 1) that determines the distance of the melting line from $B_{c2}(T)$. For most conventional superconductors to be discussed below Gi is small and the melting lines will therefore be close to the upper-critical field. However, even in isotropic superconductors Gi can be large enough so that a vortex-lattice melting transition distinct from $B_{c2}(T)$ might be observed in principle. For this case we have to additionally address the question

Table 1
Literature values for relevant material parameters of various type-II superconductors.

Substance	T_{c0} (K)	$B_{c2}(0)$ (T)	κ	ε	Gi	References
$SmFeAsO_xF_{1-x}$	55	60	99	0.125	1.66×10^{-2}	[39]
$YBa_2Cu_3O_7$	92	120	65	0.125	4.96×10^{-3}	[5,40,41]
Rb_3C_{60}	29	44	90	1	6.70×10^{-5}	[42]
MgB_2	39.0	3.1	11	0.097	4.08×10^{-5}	[43,44]
$Ba(Fe_{1-x}Co_x)_2As_2$	22	50	66	0.666	2.16×10^{-5}	[45]
$K_xBa_{1-x}BiO_3$	34.0	30	36	1	3.46×10^{-6}	[46]
Nb_3Sn	18.3	24.5	34	1	9.77×10^{-7}	[47,48]
V_3Si	16.9	23.5	22	1	1.52×10^{-7}	[47,49,50]
$LuNi_2B_2C$	16.6	9.0	13	0.75	8.31×10^{-8}	[51–53]
$NbSe_2$	7.16	5.3	11	0.31	7.88×10^{-8}	[54,55]
CaC_6	11.5	0.3	2.1	0.37	3.35×10^{-9}	[56,57]
Nb	9.22	0.416	2.2	1	2.56×10^{-10}	[58,59]

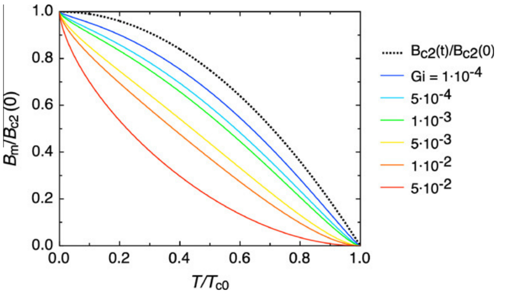

Fig. 1. Melting lines (according to Ref. [35] with c_L = 0.20) for different values of Gi.

whether $B_m(T)$ is located outside the critical-fluctuation region around $B_{c2}(T)$ or not. For the case $b \to 1$, which is of interest here, Mikitik and Brandt [35] have estimated the difference

$$\delta B = B_{c2}(T) - B_m(T) \approx \left(\frac{1.78}{2\pi c_L^2}\right)^{2/3} B_{c2}(0) t^{2/3} Gi^{1/3} (1 - t^2)^{2/3}. \tag{8}$$

The width of the critical-fluctuation region in a magnetic field on the temperature scale, on the other hand, has been estimated to [38]

$$\delta T_{\text{fluct}} \approx T_{c2}(B) Gi^{1/3} \left(\frac{B}{B_{c2}(0)}\right)^{2/3} \tag{9}$$

where $T_{c2}(B)$ is the inverted $B_{c2}(T)$. The corresponding width in B around $B_{c2}(T)$ is

$$\delta B_{\text{fluct}} \approx \left|\frac{dB_{c2}}{dT}\right| \delta T_{\text{fluct}} = 2B_{c2}(0) t^2 Gi^{1/3} (1 - t^2)^{2/3} \tag{10}$$

where we have again made use of Eq. (3). The melting line is outside the critical region if $\delta B > \delta B_{\text{fluct}}$, or

$$t < 0.361/c_L, \tag{11}$$

which is always fulfilled for reasonable values of c_L, *notably independently of the value of Gi*. A tighter condition, $\delta B > n\delta B_{\text{fluct}}$ with $n > 1$, will modify this criterion to $t < 0.361 n^{-3/4}/c_L$, but we may note that a clear first-order transition has been observed in $YBa_2Cu_3O_7$ up to $t \approx 0.98$ [7].

2.3. Discontinuities in entropy and in magnetization

To obtain the melting entropies, we make use of Richard's rule [32] for crystal lattices, in which the configurational melting entropy per particle is assumed to be a constant multiple (or fraction) of k_B. With the volume V_0 occupied by one particle we then have

$$\Delta s_0 V_0 = \eta k_B, \tag{12}$$

where Δs_0 is the configurational melting entropy per volume and η is an unknown and yet to be determined constant (see below).

To obtain the elementary volume V_0 for vortices that is relevant for counting the total number of degrees of freedom in the system, it is essential to use the correct "single-vortex length" L_0. This length has often been erroneously taken as the zero-temperature coherence length ξ [14,31], thereby vastly underestimating it and overestimating Δs_0. Kierfeld and Vinokur [33] calculated L_0 to

$$L_0 = \frac{\varepsilon a_0}{\sqrt{1 - b}} \tag{13}$$

(which is much larger than ξ), and the volume V_0 becomes

$$V_0 = \frac{\varepsilon a_0^3}{\sqrt{1 - b}} \tag{14}$$

which diverges as B approaches the upper-critical field and therefore leads to a substantial reduction of Δs_0 in materials in which the melting lines are located very close to $B_{c2}(T)$.

It turned out that the entropy obtained from applying Richard's rule alone considerably underestimates the measured entropy changes Δs upon vortex-lattice melting both in $YBa_2Cu_3O_7$ and in $Bi_2Sr_2CaCu_2O_8$ [29,30]. Taking the marked temperature dependence of thermodynamic quantities into account, Dodgson et al. arrive at an enhancement of Δs_0 of the form [30]

$$\Delta s = \frac{[1 - \tilde{b} + (2\tilde{b} - t^2)t^2]}{(1 - t^2 - \tilde{b})(1 - t^2)} \Delta s_0 \tag{15}$$

with $\tilde{b} = B/B_{c2}(0)$. Although calculated in the London approximation, Eq. (15) contains corrections to account for the suppression of the order parameter around the vortex cores in the high-field limit $b \to 1$. This enhancement of Δs_0 may be particularly relevant for superconductors with small Gi where $B_{c2}(T) - B_m(T)$ is expected to be small, because it diverges at $B_{c2}(T)$ as $(1 - b)^{-1}$ and therefore overcompensates the reduction of Δs_0 due to the diverging elementary vortex volume V_0, and also partly moderates the effect of the reduction of c_{66} on Δs_0 as $B_m(T)$ approaches $B_{c2}(T)$, see Eqs. (14) and (7). While the $B_m(T)$ line of $YBa_2Cu_3O_7$ itself is, to some extent, also modified by the arguments raised in Ref. [30] because it is located very far from $B_{c2}(T)$ in this particular compound, the $B_m(T)$ in conventional superconductors with small Gi that are under discussion here must remain very close to $B_{c2}(T)$. However, we state that even small errors in estimating $B_m(T)$ may result in substantial

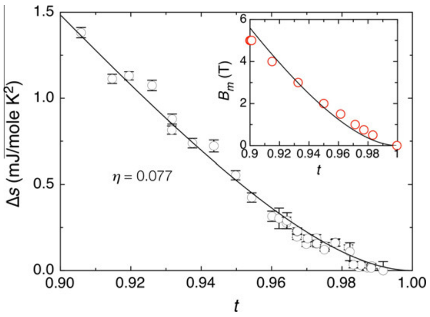

Fig. 2. Melting entropy Δs and melting line $B_m(T)$ of $YBa_2Cu_3O_7$, calculated from the parameters given in Table 1 and Eqs. (1), (5), (12), and (15). The Δs -data fit best for η = 0.077.

uncertainties in Δs (and therefore in ΔM) because these quantities sensitively depend on $(1-b)$. In this sense, the corresponding quantities calculated in the remainder of this paper have to be taken as order-of-magnitude estimates, rather than as exact results.

In the context of vortex-lattice melting, the constant η in Eq. (12) has been estimated to ≈0.16 [29] for $YBa_2Cu_3O_7$. To be consistent within our formalism, we have recalculated $B_m(T)$ and Δs for this compound according to the above rules (Eqs. (1), (5), (12), and (15)) with the material parameters from Table 1 and $c_L = 0.20$, and we obtain the best fit to the Δs data from Ref. [7] for $H//c$ with $\eta = 0.077$ (see Fig. 2). To further justify this rather small value, we can use a crude estimate taken to explain Δs in $Bi_2Sr_2CaCu_2O_8$ in Ref. [3], $T_m\Delta s = c_{66}c_L^2$, which, in combination with Eqs. (12) and (14), yields the correct melting line of Eq. (6) with $\eta = 1/A$. For $b \to 0$, we then have $\eta \approx 0.06$ and for $b \to 1$, $\eta \approx 0.03$. It is possible, however, that η assumes entirely different values in materials with lower Gi, and we therefore do not further specify the value of η in our calculations.

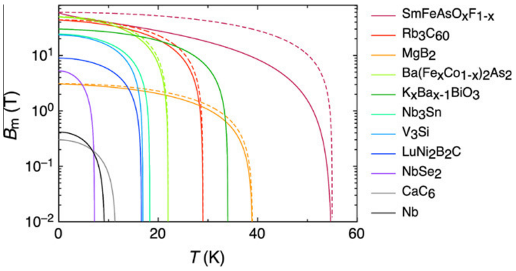

Fig. 3. Expected melting lines $B_m(T)$ for various type-II superconductors, calculated from Eqs. (1) and (5) with $c_L = 0.20$ and the material parameters given in Table 1 (solid lines). The $B_{c2}(T)$-lines (dotted lines) have been plotted only for $SmFeAsO_xF_{1-x}$, Rb_3C_{60}, MgB_2, and $Ba(Fe_xCo_{1-x})_2As_2$ for which they appear distinct from $B_m(T)$ in this representation.

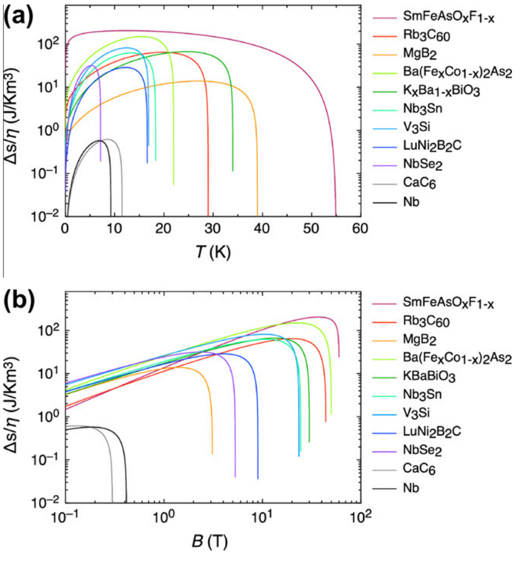

Fig. 4. Vortex-lattice melting entropies $\Delta s/\eta$ for various type-II superconductors at the $B_m(T)$ shown in Fig. 2, (a) as a function of T and (b) as a function of B.

The resulting discontinuities in magnetizations can finally be derived from the Clausius–Clapeyron equation,

$$\Delta s = -\Delta M \frac{dB_m}{dT} \tag{16}$$

with $\Delta M > 0$ i.e., M increases when crossing $B_m(T)$ from the solid to the "liquid" phase.

It is interesting to note that in the limit $\kappa \to 1/\sqrt{2}$ (i.e., when approaching the type-I limit), c_{66} in Eq. (7) vanishes even if the vortex density remains high in large magnetic fields, and so must the discontinuities in s and in M which are related to this energy scale. However, as long as $\kappa > 1/\sqrt{2}$, both Δs and ΔM remain finite even in *isotropic* superconductors with $\varepsilon = 1$ because $B_m(T)$ seems to stay outside the fluctuation region defined by Eq. (9) around $B_{c2}(T)$.

3. Application to real materials

In order to estimate the order of magnitude of the discontinuities in entropy Δs and in magnetization ΔM in real superconduc-

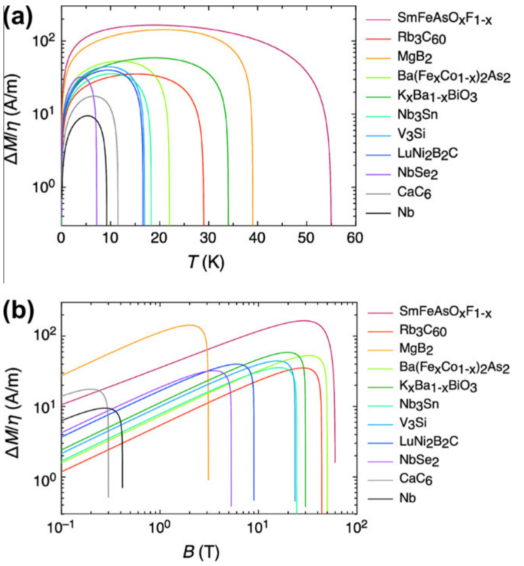

Fig. 5. Discontinuities $\Delta M/\eta$ in magnetization at the $B_m(T)$ of the materials under discussion, (a) as a function of T and (b) as a function of B.. To convert the given ΔM values from SI into cgs unit, the corresponding SI-values have to be multiplied with 10^{-3} to obtain ΔM, and with $4\pi 10^{-3}$ to obtain $4\pi\ \Delta M$ in Gauss.

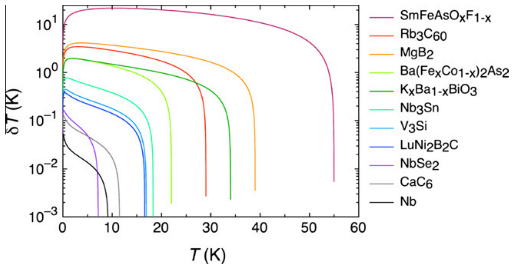

Fig. 6. Distances δT of the melting temperatures T_m from T_{c2} in experiments with fixed magnetic-flux density B.

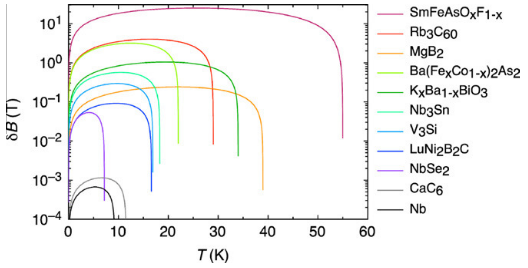

Fig. 7. Difference $\delta B = B_{c2}(T) - B_m(T)$ in experiments with constant temperature T.

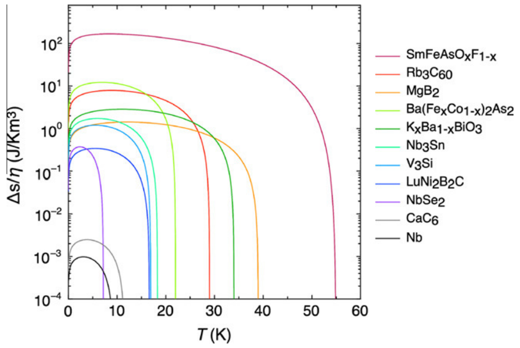

Fig. 8. Vortex-lattice melting entropies $\Delta s/\eta$ calculated as in Fig. 4a, but without the enhancement given by Eq. (15) taken into account.

tors, we have compiled literature values of relevant material parameters for a number of superconductors of contemporary interest (see Table 1). We have then calculated the melting lines $B_m(T)$ according to Eqs. (1) and (5) with $c_L = 0.20$ (see Fig. 3).

In Figs. 4–7 we have plotted the expected values for Δs and ΔM (where we tentatively took the enhancement from Eq. (15) into account, but ignoring a possible influence on B_m and Δs for the limit $\kappa \rightarrow 1/\sqrt{2}$), together with δT and δB, the distances of the melting lines from $B_{c2}(T)$ in T and in B, respectively. In Fig. 8, we also show a corresponding calculation for Δs Vs. T without the factor from Eq. (15) for comparison with Fig. 4a, to illustrate the impact of this correction on the order of magnitude ofΔs.

4. Concluding discussion

As expected, the discontinuities in Δs and ΔM are largest in compounds with a high critical temperature T_{c0} and a large Gi. The maximum possible values for the discontinuities Δs vary by more than two orders of magnitude between the different substances, and they are commonly attained around approximately $B \approx B_{c2}(0)/2$ (see Fig. 4b). The smallest Δs and ΔM values can be expected in low-T_{c0}, low-Gi materials such as Nb and CaC$_6$. Moreover, the latter materials show also low κ values of the order of unity, and they may therefore suffer from an additional reduction of Δs and ΔM as discussed above.

Nevertheless, even with a conservative estimate $\eta \approx 0.03$ and taking a reduction of the form $1 - 1/2\kappa^2$ into account, we obtain for the maximum possible Δs in Nb ≈ 16 mJ/Km^3, which should still be within reach of state-to the art calorimeters [14]. In this context we would like to mention that in Ref. [14], a marked narrowing of the expected fluctuation peak in the heat-capacity $C(T,B)$ data of Nb near $T_{c2}(B)$ has been observed, with a $C(T,B)$ that clearly exceeds the Thouless theoretical prediction [60] to explain the fluctuation contribution to the heat capacity, and notably in a field range where we find Δs to be maximum (around $B \approx 200$ mT, see Fig. 4b). A clear drop a few mK below $T_{c2}(B)$ of the diffracted intensity in corresponding small-angle neutron scattering (SANS) experiments (a quantity which is related to the magnetization M [14]), might be closely related to that anomalous behaviour because both thermodynamic quantities M and C can be derived from the same Gibb's potential $G(T,H)$. The narrowing and enhancement of the heat capacity beyond standard expectations have been explained in Ref. [14] as possibly stemming from either fluctuation contributions that are not accounted for in Thouless' original theory, or from a coupling of the vortex system to the crystal lattice, while the sharp drop in intensity (i.e., the sudden increase in M with increasing T) remained unexplained. It is conceivable that the observed heat-capacity contribution *in excess* to standard fluctuation theory is, along with the increase in M, in fact related to the missing vortex-melting entropy. A rough estimate of the excess entropy based on the $C(T,B)$ data presented in Ref. [14] is in line with the order of magnitude that we have calculated forΔs.

For Nb$_3$Sn, distinct peaks in $C(T,B)$ have been reported to occur in certain range of magnetic fields and for temperatures T near $T_{c2}(B)$ [31], which appeared only with the aid of an additional externally applied "shaking" magnetic field. Such "shaking" techniques have been very successful to reveal the ΔM in YBa$_2$Cu$_3$O$_7$ [61] because they help the vortex lattice to come to an equilibrium state [62]. The related magnetocaloric experiments on Nb$_3$Sn yield an estimate of $\Delta s \approx 2$ mJ/g-at K ≈ 180 J/Km^3 in $B = 7$T, while the published $C(T,B)$ data suggest a $\Delta s \approx 0.3$ mJ/g-at $K \approx 27$ J/Km^3 in $B = 6T$ [31]. Inspecting our Fig. 4b we estimate that under these conditions and with $\eta \approx 0.06$, $\Delta s \approx 4$ J/Km^3 at most, which is much smaller than what has been reported in Ref. [31]. We have to state, however, that Nb$_3$Sn shows a particularly strong "peak-effect" near $T_{c2}(B)$ that becomes even more pronounced upon "vortex-shaking", with a very sharp onset as T is increased towards $T_{c2}(B)$ [63]. This peak-effect is believed to be a manifestation of enhanced vortex pinning right below the upper-critical field, and the vortex lattice is therefore expected to be prone to disorder and non-equilibrium effects.

We finally want to state that the order-of magnitude estimates that we have calculated for the magnetization discontinuities, $\Delta M/\eta \approx 10$–150 A/m (with $\eta \approx 0.06$, $4\pi\Delta M \approx 8$ mG to 0.11 G in cgs units) are small, but should still be within the sensitivity specifications of commercial SQUID magnetometers. Nevertheless, unlike the heat capacity which is a measure of a bulk property of the vortex lattice (i.e., probing the total magnetic flux density B), the magnetization M very is sensitive to tiny variations in B because $\mu_0 M = B - \mu_0 H$ and usually $|\mu_0 M| \ll B$. While non-equilibrium effects due to vortex pinning may change the total flux density B only slightly, they can have disastrous consequences on attempts to measure the tiny equilibrium $\Delta M < |M| \ll B/\mu_0$.

In the above approach to obtain reasonable estimates for the expected melting entropies Δs and the associated discontinuities in magnetization ΔM we have deliberately ignored vortex pinning, although such an effect, if strong enough, can make a reliable measurement impossible because thermodynamic equilibrium is not reached on laboratory time scales. In addition, strong pinning makes the identification of the thermodynamic melting line $B_m(T)$ very difficult [64]. Moreover, we have not considered other possible peculiarities in the B–T phase diagrams, such as a dimensional crossover as observed in the cuprates [65], which would affect the occurrence of a first-order melting transition of the vortex lattice as well. We have also made assumptions that should be further backed up by theory. It should in particular be clarified to what extent the enhancement of the configurational entropy Δs_0 near $B_{c2}(T)$ in Eq. (15) is really applicable in conventional superconductors. Without such an enhancement (see Fig. 8) both the expected Δs and ΔM can be significantly smaller (by up to two orders of magnitude) than the above estimates (see Fig. 4) and may fall beyond the detection limit of an experiment. Nevertheless we believe that our considerations may serve as guideline for searching signatures of a vortex-lattice melting transition in conventional and novel superconductors, and for estimating the correct order of magnitude to be expected for the related thermodynamic quantities.

Acknowledgments

We thank to V.B. Geshkenbein and S. Weyeneth for valuable discussions. This work was supported by the Schweizerische Nationalfonds zur Förderung der wissenschaftlichen Forschung, Grant No. 20-131899.

References

[1] U. Welp, J.A. Fendrich, W.K. Kwok, G.W. Crabtree, B.W. Veal, Phys. Rev. Lett. 76 (1996) 4809–4812.
[2] A. Schilling, M. Willemin, C. Rossel, H. Keller, R.A. Fisher, N.E. Phillips, U. Welp, W.K. Kwok, R.J. Olsson, G.W. Crabtree, Phys. Rev. B 61 (2000) 3592.
[3] E. Zeldov, D. Majer, M. Konczykowski, V.B. Geshkenbein, V.M. Vinokur, H. Shtrikman, Nature 375 (1995) 373.
[4] A. Schilling, R.A. Fisher, N.E. Phillips, U. Welp, D. Dasgupta, W.K. Kwok, G.W. Crabtree, Nature 382 (1996) 791.
[5] A. Schilling, R.A. Fisher, N.E. Phillips, U. Welp, W.K. Kwok, G.W. Crabtree, Phys. Rev. Lett. 78 (1997) 4833.
[6] A. Schilling, R.A. Fisher, N.E. Phillips, U. Welp, W.K. Kwok, G.W. Crabtree, Phys. Rev. B 58 (1998) 11157–11160.
[7] A. Schilling, U. Welp, W.K. Kwok, G.W. Crabtree, Phys. Rev. B 65 (2002) 054505.
[8] F. Bouquet, C. Marcenat, E. Steep, R. Calemczuk, W.K. Kwok, U. Welp, G.W. Crabtree, R.A. Fisher, N.E. Phillips, A. Schilling, Nature 411 (2001) 448.
[9] M. Roulin, A. Junod, A. Erb, E. Walker, J. Low Temp. Phys. 105 (1996) 1099.
[10] M. Roulin, A. Junod, E. Walker, Science 273 (1996) 1210.
[11] M. Roulin, A. Junod, A. Erb, E. Walker, Phys. Rev. Lett. 80 (1998) 1722.
[12] C. Marcenat, F. Bouquet, R. Calemczuk, U. Welp, W.K. Kwok, G.W. Crabtree, R.A. Fisher, N.E. Phillips, A. Schilling, Physica C 341–348 (2000) 949.
[13] A. Junod, M. Roulin, J.-Y. Genoud, B. Revaz, A. Erb, E. Walker, Physica C 275 (1997) 245.
[14] C.J. Bowell, R.J. Lycett, M. Laver, C.D. Dewhurst, R. Cubitt, E.M. Forgan, Phys. Rev. B 82 (2010) 144508.
[15] A.A. Abrikosov, JETP 5 (1957) 1174.
[16] D.R. Nelson, Phys. Rev. Lett. 60 (1988) 1973–1976.
[17] A. Houghton, R.A. Pelcovits, A. Sudbø, Phys. Rev. B 40 (1989) 6763.
[18] P.L. Gammel, L.F. Schneemeyer, J.V. Wasczak, D.J. Bishop, Phys. Rev. Lett. 61 (1988) 1666–1669.
[19] D.E. Farrell, J.P. Rice, D.M. Ginsberg, Phys. Rev. Lett. 67 (1991) 1165–1168.
[20] H. Safar, P.L. Gammel, D.A. Huse, D.J. Bishop, J.P. Rice, D.M. Ginsberg, Phys. Rev. Lett. 69 (1992) 824–827.
[21] R. Cubitt et al., Nature 365 (1993) 407–411.
[22] D.S. Fisher, M.P.A. Fisher, D.A. Huse, Phys. Rev. B 43 (1991) 130–159.
[23] G. Blatter, B. Ivlev, Phys. Rev. Lett. 70 (1993) 2621.
[24] G. Blatter, M.V. Feigel'man, V.B. Geshkenbein, A.I. Larkin, V.M. Vinokur, Rev. Mod. Phys. 66 (1994) 1125.
[25] H. Pastoriza, M.F. Goffman, A. Arribére, F. de la Cruz, Phys. Rev. Lett. 72 (1994) 2951–2954.
[26] M.P.A. Fisher, Phys. Rev. Lett. 62 (1989) 1415.
[27] B. Revaz, A. Junod, A. Erb, Phys. Rev. B. 58 (1998) 11153–11156.
[28] H. Iwasaki, T. Chigira, T. Naito, S. Moriyama, Y. Iwasa, T. Nishizaki, N. Kobayashi, Physica C 366 (2002) 129–134.
[29] M.J.W. Dodgson, V.B. Geshkenbein, H. Nordborg, G. Blatter, Phys. Rev. Lett. 80 (1998) 837–840.
[30] M.J.W. Dodgson, V.B. Geshkenbein, H. Nordborg, G. Blatter, Phys. Rev. B 57 (1998) 14498–14506.
[31] R. Lortz, F. Lin, N. Musolino, Y. Wang, A. Junod, B. Rosenstein, N. Toyota, Phys. Rev. B 74 (2006) 104502.
[32] A.R. Ruffa, Phys. Rev. B 25 (1982) 5895.
[33] J. Kierfeld, V. Vinokur, Phys. Rev. B 69 (2004) 024501.
[34] F.A. Lindemann, Z. Phys. 11 (1910) 609.
[35] G.P. Mikitik, E.H. Brandt, Phys. Rev. B 64 (2001) 184514.
[36] E.H. Brandt, Phys. Rev. B 34 (1986) 6514.
[37] S. Ryu, S. Doniach, G. Deutscher, A. Kapitulnik, Phys. Rev. Lett. 68 (1992) 710.
[38] P.A. Lee, S.R. Shenoy, Phys. Rev. Lett. 28 (1972) 1025.
[39] U. Welp, C. Chaparro, A.E. Koshelev, W.K. Kwok, A. Rydh, N.D. Zhigadlo, J. Karpinski, S. Weyeneth, Phys. Rev. B 83 (2011) 100513.
[40] H. Nakagawa, N. Miura, Y. Enomoto, J. Phys.: Condens. Matter. 10 (1998) 11571.
[41] U. Welp, W.K. Kwok, G.W. Crabtree, K.G. Vandervoort, J.Z. Liu, Phys. Rev. Lett. 62 (1989) 1908–1911.
[42] A.I. Sokolov, Y.A. Kufaev, E.B. Sonin, Physica C 212 (1993) 19–22.
[43] C. Bueza, T. Yamashita, Supercond. Sci. Technol. 14 (2001) R115.
[44] M. Angst, R. Puzniak, A. Wisniewski, J. Jun, S.M. Kazakov, J. Karpinski, J. Roos, H. Keller, Phys. Rev. Lett. 88 (2002) 167004.
[45] A.S. Sefat, R. Jin, M.A. McGuire, B.C. Sales, D.J. Singh, D. Mandrus, Phys. Rev. Lett. 101 (2008) 117004.
[46] B.A. Baumert, J. Supercond. 8 (1995) 175.
[47] G. Otto, E. Saur, H. Wizgall, J. Low Temp. Phys. 1 (1969) 19.
[48] M.N. Khlopkin, Sov. Phys. JETP 63 (1986) 164.
[49] M.N. Khlopkin, JETP Lett. 39 (1984) 358.
[50] D. Eckert, K.H. Berthel, Cryogenics 15 (1975) 479.
[51] W.E. Pickett, D.J. Singh, Phys. Rev. Lett. 72 (1994) 3702.
[52] M.R. Eskildsen, P. Gamel, B.P. Barber, A.P. Ramirez, D.J. Bishop, N.H. Andersen, K. Mortensen, C.A. Bolle, C.M. Lieber, P.C. Canfield, Phys. Rev. Lett. 79 (1997) 487.
[53] G.M. Schmiedeshoff, C.D. Boer, M.V. Tompkins, W.P. Beyermann, A.H. Lacerda, J.L. Smith, P.C. Canfield, J. Supercond. Nov. Magn. 13 (2000) 847.
[54] D.E. Prober, M.R. Beasley, R. Schwall, Phys. Rev. B 15 (1977) 5245.
[55] F. Soto, H. Berger, L. Cabo, C. Carballeira, J. Mosqueira, D. Pavuna, P. Toimil, F. Vidal, Physica C 460–462 (2007) 789.
[56] E. Jobiliong, H.D. Zhou, J.A. Janik, Y.-J. Jo, L. Balicas, J.S. Brooks, C.R. Wiebe, Phys. Rev. B 76 (2007) 052511.
[57] F. Muranányi, M. Bendele, R. Khasanov, Z. Guguchia, A. Shengelaya, C. Balnes, H. Keller, J. Supercond. Nov. Magn. 25 (2012) 159.
[58] N.Y. Alekseyevskiy, V.I. Nizhankovskiy, K.-H. Bertel, Fiz. Metal. Metalloved. 37 (1974) 53.
[59] S.P. Farrant, C.E. Gough, Phys. Rev. Lett. 34 (1975) 943.
[60] D.J. Thouless, Phys. Rev. Lett. 34 (1975) 946.
[61] M. Willemin, A. Schilling, H. Keller, C. Rossel, J. Hofer, U. Welp, W.K. Kwok, R.J. Olsson, G.W. Crabtree, Phys. Rev. Lett. 81 (1998) 4236.
[62] E.H. Brandt, G.P. Mikitik, Phys. Rev. Lett. 89 (2002) 027002.
[63] M. Reibelt, A. Schilling, N. Toyota, Phys. Rev. B 81 (2010) 094510.
[64] D. Majer, E. Zeldov, M. Konczykowski, Phys. Rev. Lett. 75 (1995) 1166–1169.
[65] M.V. Feigel'man, V.B. Geshkenbein, A.I. Larkin, Physica C 167 (1990) 177.

5. The AC calorimeter

In order to measure the signature of the vortex lattice melting in the specific heat, we employed the AC calorimeter technique pioneered by Corbino [91, 92], more specifically an improved version first described by Sullvian and Seidel [93]. The latter work describes the application of Corbino's AC calorimetry technique [91] optimized for low temperature measurements. The main advantages are the high precision exceeding previous techniques by an order of magnitude, and the fact that it is a steady state measurement, which allows one to measure the variation of the heat capacity at a quasi-constant temperature as a function of an external parameter like the magnetic field. For a topical review of the AC calorimetry technique, the reader is referred to Ref. [94].

5.1. Challenges

As we have demonstrated in Chapter 4 the thermodynamic signature of vortex lattice melting is fairly weak in certain low temperature superconductors, especially if the enhancement due to fluctuations turns out to be smaller than predicted by the theory of Dodgson *et al.* [55]. Furthermore, the vortex melting transition is predicted to be only a few millikelvin away from the transition to the superconducting state for many substances. This poses two challenges for samples of milligram size: achieving a specific heat resolution better than approximately $1\,\mathrm{mJ}\cdot\mathrm{K}^{-1}$ and at least a $20\,\mathrm{mK}$ temperature accuracy at temperatures $\approx 10\,\mathrm{K}$, so that the melting signature can be clearly distinguished from the transition to the superconducing state.

5.2. Principle of AC calorimetry

An AC calorimeter consists of a sample holding platform, which is equipped with an electrical heater of resistance R and a defined heat link k to a thermal bath, temperature stabilized at temperature T_{bath}. A thermometer is attached to the platform continuously monitoring the temperature (see Fig. 5.1).

If we assume the sample to be in perfect thermal contact with the sample platform (and therefore forming a unit of common heat capacity C), the differential equation describing the temperature $T(t)$ under the influence of a varying heating power $P(t)$ is

$$\dot{T}(t) = \frac{P(t) - k(T(t) - T_{\mathrm{bath}})}{C}. \tag{5.1}$$

A sinusoidal voltage $U = U_0 \cos \frac{\omega}{2} t$ applied to the heater with resistance R results in a heating power $P(t) = P_0 (1 + \cos \omega t)$, where $P_0 = \frac{U_0^2}{2R}$. We can then rewrite Eq. (5.1) as the real part of a complex differential equation:

$$\Re\left\{\dot{T}(t)\right\} = \Re\left\{-\frac{k}{C} T(t) + \frac{P_0}{C} e^{i\omega t} + \frac{P_0 + k T_{\mathrm{bath}}}{C}\right\}. \tag{5.2}$$

The solution is the real part of

$$\Re\{T(t)\} = \Re\left\{\frac{P_0}{k} + T_{\mathrm{bath}} + \frac{P_0}{i\omega C + k} e^{i\omega t} + \Delta T_0 e^{-\frac{k}{C} t}\right\}. \tag{5.3}$$

The last term describes how the temperature approaches the steady state solution given an initial deviation ΔT_0 from it at $t = 0$. After a time given by some large multiple of $\tau_0 = \frac{C}{k}$, this term becomes negligible and the temperature oscillates around the temperature $\langle T \rangle = \frac{P_0}{k} + T_{\mathrm{bath}}$ with an amplitude and a phase shift $-\delta$ given by the coefficient T_0,

$$T_0 = \frac{P_0}{i\omega C + k}, \tag{5.4}$$

$$\delta = \arctan \frac{-\omega C}{k}, \tag{5.5}$$

$$|T_0| = \frac{P_0}{\sqrt{\omega^2 C^2 + k^2}}. \tag{5.6}$$

If the heat link k is known, one can thus calculate the heat capacity from the temperature measurement, either through the amplitude T_0 or through the phase

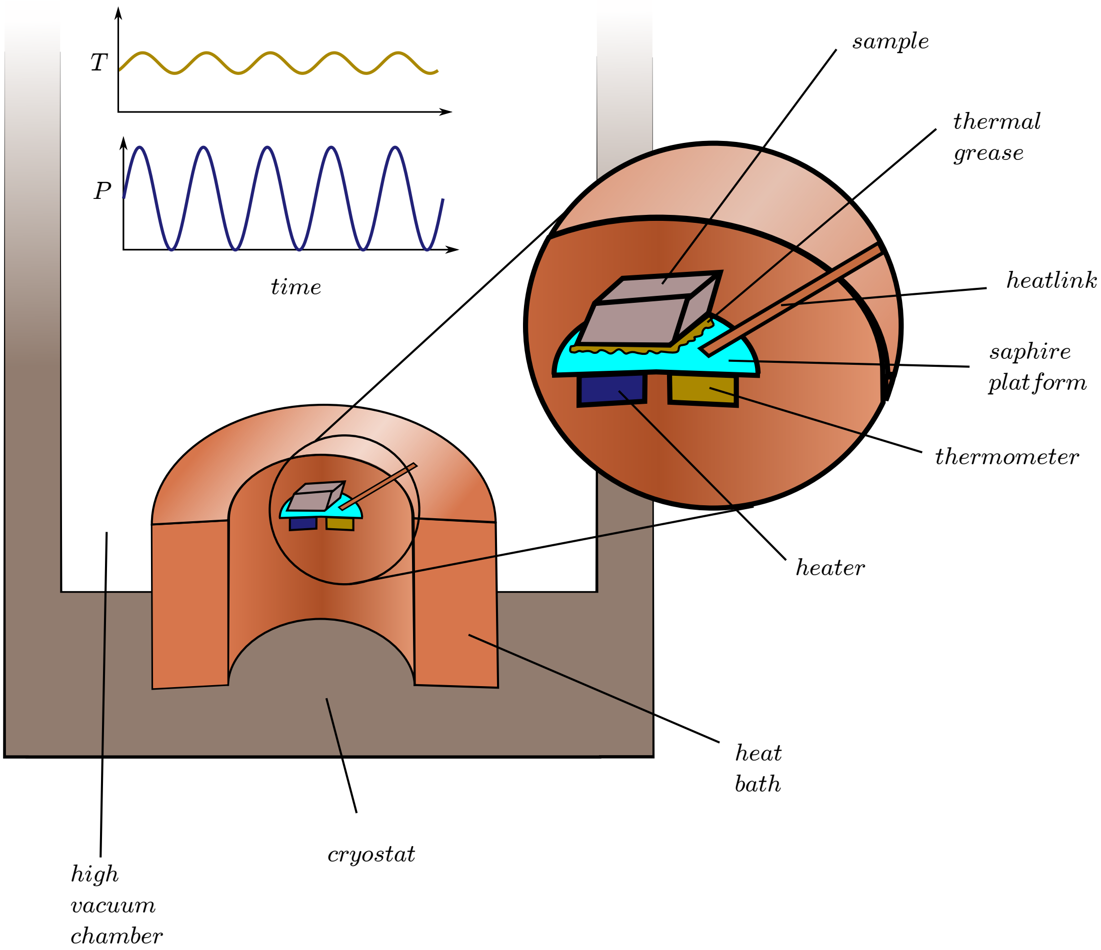

Figure 5.1.: Working principle of the AC calorimeter: A sample platform equipped with a thermometer and a heater is connected to a heat bath by a heat link. The platform is heated sinusoidally with power $P(t)$. The heat capacity of the platform and the attached sample can be determined from the amplitude and the phase shift of the resulting temperature oscillation.

shift δ

$$C = \frac{1}{\omega}\sqrt{\frac{P_0^2}{T_0^2} - k^2} = \frac{-k\tan\delta}{\omega}. \tag{5.7}$$

If the heat link is unknown, one can calculate k and C from the phase and the amplitude alone

$$C = \frac{-P_0 \sin\delta}{|T_0|\,\omega}, \tag{5.8}$$

$$k = \frac{P_0 \cos\delta}{|T_0|}. \tag{5.9}$$

Since a knowledge of the heat link is not required in Eq. (5.8) and Eq. (5.9), this method seems to be preferable at first sight. However the phase is much more sensitive to an imperfect thermal coupling of the sample to the thermometer (as shown by Sullivan and Seidel in Ref. [93]) which may therefore produce a measurement of poorer quality than using Eq. (5.7) with a known calibrated heat link k. The amplitude and phase error can be characterized by a finite equilibration time τ [93]. Using the error term Eqs. (5.5) and (5.6) become:

$$|T_0| = \frac{P_0}{\sqrt{\omega^2 C^2 + k^2 + \omega^2 C^2 \left(\omega\tau\right)^2}} \tag{5.10}$$

$$\delta = \operatorname{arccot}\left(\frac{k}{\omega C} - \omega\tau\right). \tag{5.11}$$

Because our measurements are in a frequency region where $k \ll \omega C$ the argument of the arccot function of Eq. (5.11) is close to 0 and therefore at the point of the largest slope of the arccot function, making the phase much more susceptible to error then the temperature amplitude.

5.3. Vortex lattice shaking effects

When measuring thermodynamic effects of the vortex matter, sample dependent vortex pinning usually prevents the system from reaching the thermodynamic equilibrium. In order to alleviate the effects of pinning Willemin *et al.* used a *vortex shaking* method in magnetic torque measurements [32], i.e. the application of a small oscillating magnetic field in addition to the main magnetic field (see section 3.2).

Whether the vortex shaking technique is helpful in heat capacity measurements depends to a large extent on the amount of *self heating* that it induces in a sample. While the AC technique is by design immune to artifacts from temperature offsets caused by a constant or slowly varying self heating power, a strong dependence of the self heating power on the temperature will produce artifacts if the data analysis is done according to (5.7). With the added heating power of the magnetic shaking, Equation (5.1) becomes

$$\dot{T}\,(t) = \frac{P\,(t) - k(T(t) - T_{\text{bath}}) + P_s(T(t))}{C}, \tag{5.12}$$

where $P_s(T(t))$ is the magnetic heating power in the "shaking" field according to Eq. (6.14). If we assume that $P_s(T)$ is a smooth function of T, we can approximate it linearly around our measurement temperature T_m,

$$P_s(T(t)) \approx P_{s0} + \left.\frac{\mathrm{d}P_S(T)}{\mathrm{d}T}\right|_{T_m} (T(t) - T_m)\,. \tag{5.13}$$

Inserting in (5.12) yields

$$\begin{aligned} \dot{T}\,(t) &= \frac{P\,(t) - k(T(t) - T_{\text{bath}}) + P_{s0} + \left.\frac{\mathrm{d}P_s(T)}{\mathrm{d}T}\right|_{T_m} (T - T_m)}{C} && (5.14) \\ &= \frac{P\,(t) - \left(k - \left.\frac{\mathrm{d}P_s(T)}{\mathrm{d}T}\right|_{T_m}\right) T(t)}{C} + \text{const.} && (5.15) \end{aligned}$$

The constant term will only produce an offset in the temperature solution $T(t)$ (which needs to be measured), but does not produce any different result in the evaluation of the heat capacity. On the other hand, it is important to realize that we can reproduce the old form of the differential equation (5.1) by redefining k

$$k_{\text{eff}} = k - \left.\frac{\mathrm{d}P_s(T)}{\mathrm{d}T}\right|_{T_m}\,. \tag{5.16}$$

Since the heat link does not affect Eq. (5.8) we could in principle still calculate the heat capacity using the phase, but Eq. (5.7) will produce false results if the

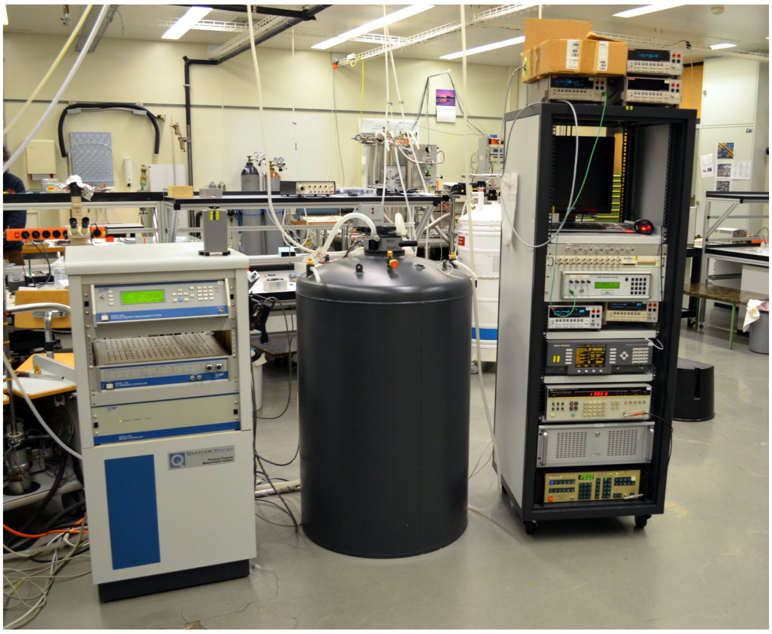

Figure 5.2.: From left to right: Model 6000 control unit for the PPMS cryostat (middle) and the 19 inch rack for additional electronic devices including the controlling computer

thermal link is not corrected according to Eq. (5.16). This is particularly relevant if $\mathrm{d}P_s(T)/\mathrm{d}T$ depends on temperature.

5.4. Device setup in a PPMS

5.4.1. PPMS

For cryogenic measurements of heat capacities a good temperature control and high vacuum conditions are imperative. A Physical Properties Measurement System (PPMS, *Quantum Design*) served as the base platform for our experiments (see Fig. 5.2). This cryostat offers measurement options for a number of different physical properties of materials, like electric resistance, Hall effect, magnetic susceptibility, and the Seebeck effect. This top loader design deviates from most standard designs by the fact that the main electrical leads to the sample space are connected with a plug on the bottom of the sample chamber. The cryostat uses a layer design, with a super-insulated vacuum on the outside, followed by a liquid nitrogen shield, and an internal liquid helium vessel. The temperature is PID sta-

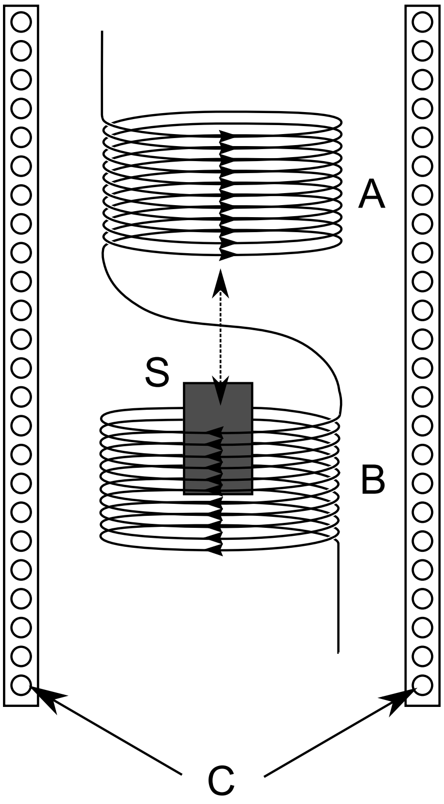

Figure 5.3: The AC magnetization setup. The main coil C superimposes an alternating magnetic field on top of the main field. The pickup coils A and B are wound in the opposite sense and cancel each others signal unless a sample S is present. Moving the sample between coil A and B changes the polarity of the sample.

bilized, and the system reaches its minimum temperature of about $T_{\mathrm{min}} \approx 1.8\,\mathrm{K}$ within 90 minutes, if only the standard sample pucks are used. The temperature stability depends on the temperature set point and is $\approx 5\,\mathrm{mK}$ at cryogenic temperatures, with occasional stronger fluctuations of up to $\approx 20\,\mathrm{mK}$. The PPMS is equipped with a superconducting magnet that allows for magnetic fields up to $9\,\mathrm{T}$, and field ramping rates up to $20\,\mathrm{mT}\cdot\mathrm{s}^{-1}$. The vacuum system is implemented with a cryopump using activated charcoal at liquid helium temperatures to reach high vacuum conditions within about 15 minutes. The temperature, the magnetic field as well as the pressure can be computer controlled using commands on a GPIB bus.

AC magnetization option

The PPMS is equipped with an AC magnetization option. It is used to measure the alternating current magnetic susceptibility of a sample. The measurement principle is depicted in Fig. 5.3. In addition to the main field of the PPMS an AC magnetic field is superimposed using a primary coil C. Inside the main coil there are two secondary counter-wound pickup coils A and B. If there is no sample present, the induced e.m.f. in these two coils ideally cancels completely. When a sample is moved through the two coils the respective coil's inductance changes according to $L' = \mu L$ where μ is the effective magnetic permittivity of the sample. The coils are not matched anymore, and a non-zero total voltage is induced. When the sample is moved from coil A to coil B the signal changes polarity, and thus the differential signal can be used to cancel any offset noise. The coil setup is calibrated by factory, and the PPMS software automatically calculates the real and imaginary part of a differential magnetization

$$m = \frac{\mathrm{d}M}{\mathrm{d}H} H_0, \tag{5.17}$$

where H_0 is the amplitude of the AC magnetic field.

The differential susceptibility

$$\chi = \frac{\mathrm{d}M}{\mathrm{d}H}, \tag{5.18}$$

is not always equal to the DC susceptibility $\chi_{\mathrm{DC}} = M/H$, which should be kept in mind when interpreting the measurement data.

5.4.2. AC calorimetry pucks

Custom measurement pucks were constructed for AC calorimetry experiments that also allow for additional *shaking fields* parallel and transverse to the main magnetic field direction (see Section 3.2). A drawing of such a measurement puck with the main components exposed is shown in Fig. 5.4.

Body

The main body of the pucks is made of a Beryllium-Copper (Berylco 25) alloy with a particularly low magnetic susceptibility, which was well suited for machining in the workshop of the Physics Institute of the University of Zürich. Its thermal conductivity is similar to that of low grade copper. The surfaces were gold plated to prevent the typical corrosion of copper alloys. A relatively high mass of approximately 30 g acts as a heat reservoir and buffers thermal fluctuations of the cryostat. Thermal contact of the puck with the cryostat is accomplished in

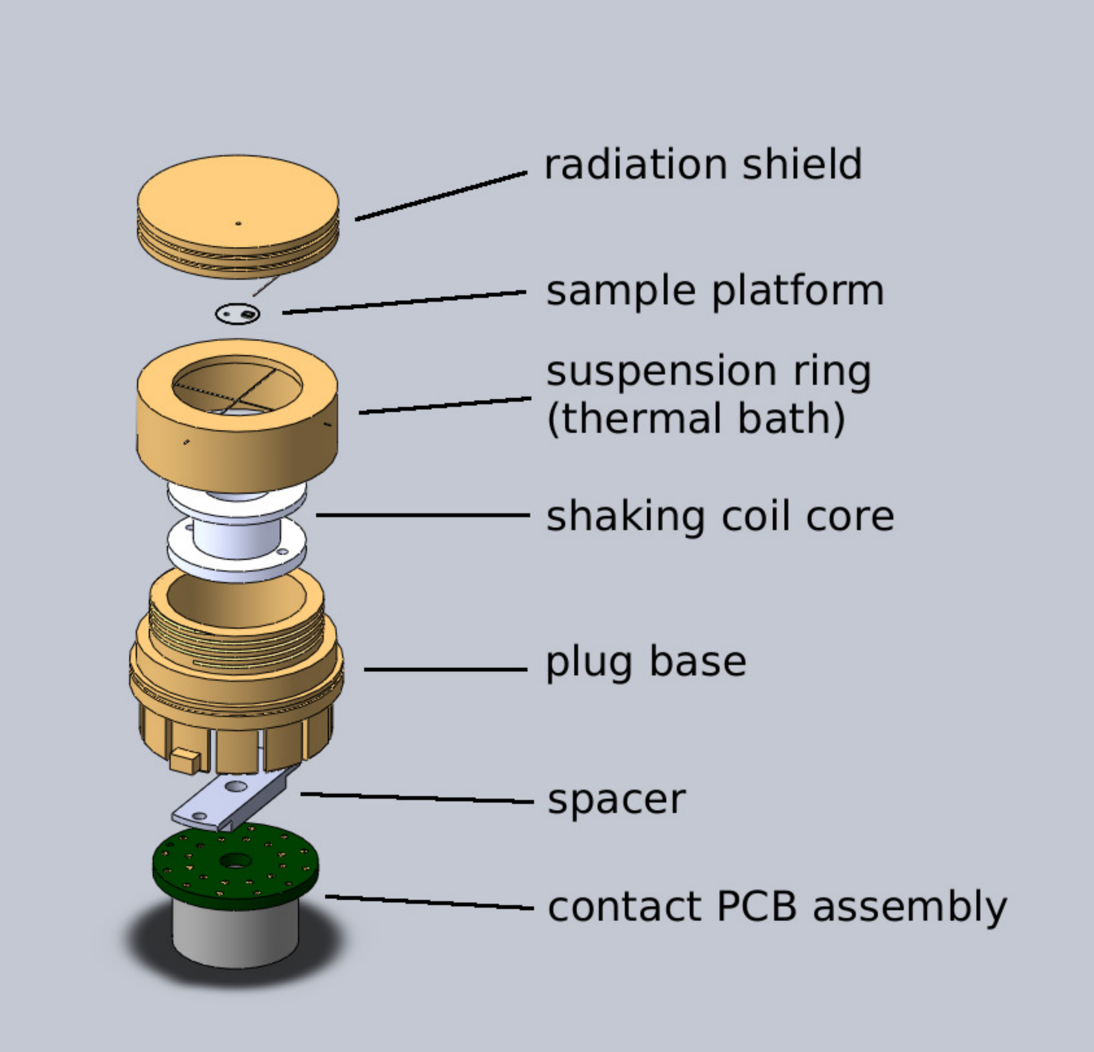

Figure 5.4.: Explosion drawing of the puck for parallel shaking

the same way as for the commercial PPMS pucks, namely by twelve very tightly fitting metal segments.

Electrical contacts

Electrical contacts to the puck are realized using the internal PPMS leads accessible via the Lemo B314 sample space connector of the PPMS. Inside the sample space a plug (made of twelve pin sockets encased in a holder made of spun fiberglass epoxy) is mounted to a printed circuit board (PCB). The PCB is providing soldering pads for the attachment of wires to all electrical components of the puck. The plug assembly is attached to the base with a screw held in place by a spacer. A Berylco pin is used for keying to ensure matching pins on each assembly.

Suspension ring

The sample platform is suspended inside a Berylco ring on top of the puck with nylon threads. The ring holds a second PCB with a thickness of 25 µm. It is glued in using GE 7031 varnish to ensure good thermal and mechanical contact and is inaccessible from the outside, allowing for mechanical protection of the contacts. In addition to the electrical wiring a heat link can be provided by gluing additional metal wires in between the thermal bath ring and the sample platform to optimize the oscillation frequency for a given temperature range.

Sample platform

The sample platform was made of a sapphire disk with diameter of 4.9 mm and a thickness of 100 µm. A 1 kΩ size 0201 SMD resistor for heating and a Cernox CX-1050-BC resistance thermometer are attached to the disk with GE 7031 varnish. The electrical contacts to these elements to the suspension ring PCB are made of 30 µm thick manganin wire. The resulting weak heat link ensures that the internal equilibration time of the sample platform is always much smaller than the time constant for the equilibration with the thermal bath.

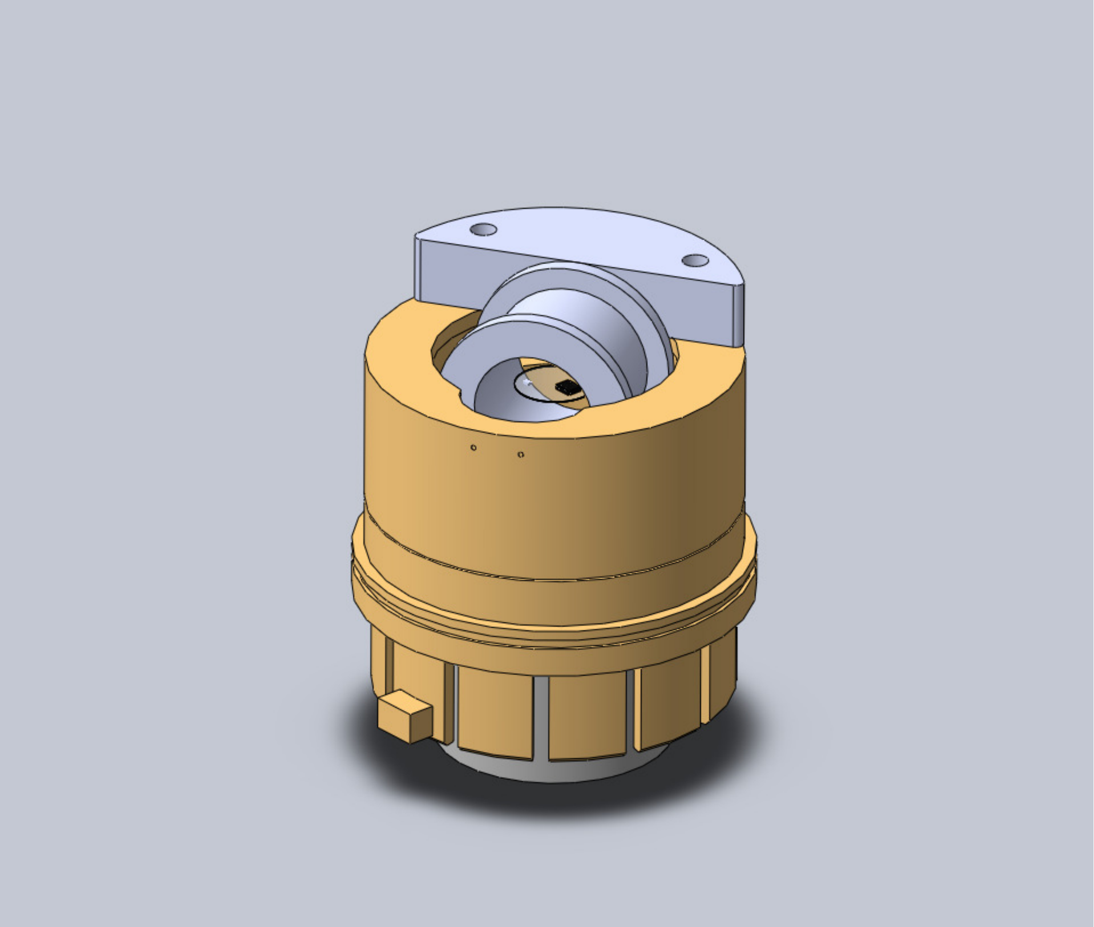

Figure 5.5.: Drawing of the assembled puck for shaking with field perpendicular to main field

Shaking coil

The two fabricated pucks allow for an electrical shaking field either in parallel or perpendicular to the applied external field. The parallel shaking coil has approximately 1000 turns and is wound on a base made of POM plastic. The perpendicular coil is made of Vespel plastic, has 700 turns and is glued into place by potting it with Stycast epoxy, in order to prevent vibrations due to the torque of the crossed magnetic fields. A sketch of the puck without wiring is displayed in Fig. 5.5.

Radiation shield

A 2 mm thick lid made of Berylco is shielding the sample from thermal radiation in case of the parallel shaking puck, whereas the same shielding is accomplished with a piece of aluminum foil in case of the perpendicular shaking puck. Additionally the bevel insert of the PPMS is used to prevent a direct path for thermal radiation from the room temperature flange.

5.4.3. Measuring electronics design

Heat capacity measurements are subject to noise of numerous sources. Some of this noise stems from thermal fluctuations of the measurement puck and the sample platform, induced by thermal radiation, gas flows the high vacuum chamber, and mechanical tension producing heat or changing thermal conductivities.

The puck is designed to mitigate these effects by enclosing the sample inside the measurement puck, and by buffering external effects through a fairly large heat capacity. Another source of measurement noise is of electronic nature. Thermal EMFs from contacts at different temperatures, electrical interference and intrinsic component noise degrades the signal quality. In order to reduce this noise, a number of measures were taken.

Wheatstone bridge

As the AC calorimetry method is measuring temperature oscillations around a base temperature, this type of measurement is facilitated by a Wheatstone bridge setup. This makes the corresponding voltage signal bipolar around zero with respect to a reference value. As a reference we use a computer controlled M-602 resistance decade (*Orbit controls*). The device was retrofitted with a BNC connector instead of the banana plugs in order to reduce noise. The main relay switchboard was encased in a 5 mm thick copper box, to reduce electrical noise and also to dampen temperature swings of the reference resistors. We have added an adjustable parallel capacitor to compensate differences in the cables capacities. The choice of the external reference resistor breaks the usual fully differential balanced design for this type of setup, but it keeps all reference resistors under stable room temperature conditions, and thus the thermometer resistance is the only unknown quantity.

Lock in amplifier

The differential signal of the Wheatstone Bridge is measured using a *Signal Recovery* 7280 Lock in Amplifier running at 45 kHz. It uses a low pass filter with a time constant of approximately 20 ms for integration. This removes slow drifts from thermal voltages, audio frequencies and effectively all types of $1/f$-noise from the measurement signal. Because of the large integration time the bandwidth of the signal is reduced to 500 Hz and therefore only the noise components within this frequency window are relevant.

kHz preamplifier

Part of the signal noise is due to electrical interference. Techniques for a reduction of the effects of interference are shielding, differential design and early amplification. The result of our efforts is an amplifier which is plugged directly into the PPMS. Its aluminum casing completes the shield with the PPMS dewar. Thus all wires from the sample to the preamplifier have a 4π sr metal shielding enclosure. After a high pass filter with a corner frequency of 16 Hz the signal passes into a fully differential amplifier with a fixed gain of 100. Then it is high pass filtered again, since the DC voltage offset from the previous stage was already strongly amplified. A second stage with a gain of 10 feeds into a voltage controlled voltage source (VCVS) low pass filter design, which is configured as a 2-pole Butterworth filter. The total gain of the setup at the measurement carrier frequency of 45 kHz is $G = 419$. The purpose of filtering is conditioning the signal for the input stage of the lock in amplifier, and it has a negligible effect on noise cancellation. The lock in technique by itself will do the actual frequency filtering with a very high Q-factor, but only when the input stage is not driven into overload. The effect of the amplifier is a reduction of the relative noise stemming from electromagnetic pick up on the cable to the lock in amplifier by the factor G.

5.4.4. Computer control

The computer control is done entirely through the GPIB bus. All programming was done in the programming language python, using the `pyvisa` module, and the *National Instruments* `visa` library. The programs are platform independent and run on Windows or Linux.

Typical measurement sequence

1. set appropriate heating amplitude
2. wait for PPMS status “temperature stable”
3. wait for 100 seconds for the sample to reach thermal equilibrium
4. run subroutine to equilibrate the Wheatstone bridge
5. start acquisition of 8000 data points with the lock in amplifier
6. make auxiliary measurements until data acquisition is completed
7. set next PPMS temperature
8. download lock in data
9. get readings from all other devices
10. write readings to file
11. calculate next heating amplitude
12. go to 1

6. Measurements on Nb_3Sn

6.1. History and properties of Nb_3Sn

The high field superconductor Nb_3Sn with a critical temperature of $T_c = 18.05\,\mathrm{K}$ was discovered in 1954 by Matthias *et al.* [95], one year after V_3Si (the first compound of the A-15 crystal class) shown to be superconducting with a $T_c = 16.9\,\mathrm{K}$. This class of materials held the record ($T_c = 23\,\mathrm{K}$ for Nb_3Ge) for the highest critical temperature of any superconductor before the discovery of the high temperature cuprate superconductors by Müller and Bednorz in 1986.

A-15 superconductors are generally formed in a A_3B stoichiometry, where the A atoms represent the transition metal elements Ti, Zr, V, Nb, Ta, Cr, and Mo, while the B atoms are mostly from periodic groups IIIB and IVB. The A-atoms form chains along the crystallographic axes of the cubic crystal lattice depicted in Fig. 6.1. These chains are one dimensional structures and thus produce a divergence of the density of states at the Fermi level in the form of van Hoove singularities, resulting in the high critical temperature according to Eq. (2.15). If the chains are disturbed by radiation induced defects or alloying, T_c generally decreases.

In addition to the transition to the superconducting state many A-15 compounds undergo a martensitic transition at a temperature $T_m > T_c$. The crystal stretches in one of the three main axes turning the crystal structure into orthorhombic. Whether this transition takes place or not depends on the crystal specimen at hand even for one particular material. The effect of the changed crystal lattice symmetry on the superconducting properties is not completely understood, but the transition temperature to the superconducting state seems to stay within a range of a few Kelvin, regardless of the appearance of the martensitic transition. For an in-depth discussion of the A-15 compounds the reader is referred to the review by Dew-Hughes [96]. Today, superconducting solenoids made of Nb_3Sn are still the dominant choice for high field magnet applications, for example in

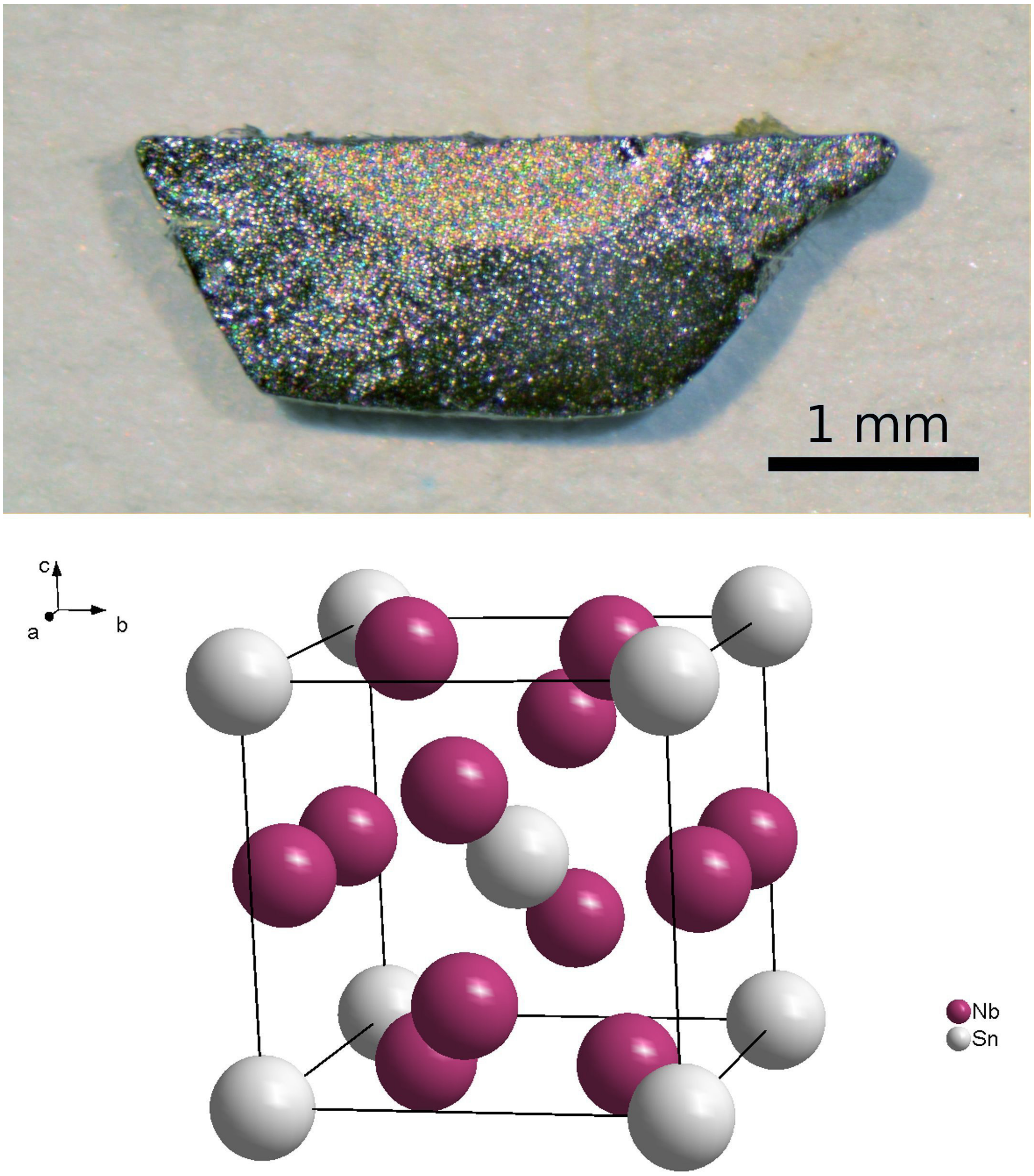

Figure 6.1.: The Nb$_3$Sn sample which was studied and its unit cell. The camera facing side of the sample is in the (1 1 0) lattice direction. The thickness is about 0.4 mm.

the planned ITER fusion reactor, due to the high critical current densities of $j_c \approx 7 \times 10^8\,\mathrm{A/m^2}$ which this material provides. [97]

6.2. A $\mathrm{Nb_3Sn}$ crystal showing a peak effect near H_{c2}

The sample of $\mathrm{Nb_3Sn}$, which was examined by us, is a single crystal with the dimensions of 3.6 mm(long side)×1.3 mm×0.4 mm and with a mass of $m \approx 11.9\,\mathrm{mg}$. The flat surface depicted in Fig. 6.1 is in the crystallographic [1 1 0] direction which will generally be the direction in which we apply the main magnetic field unless otherwise stated. The sample was grown by Toyota *et al.* using the chemical vapor deposition technique by Harnak and Berman [98] with some modifications [99]. It was cut using spark erosion and further characterized in Refs. [100, 101], where it was shown by x-ray measurements to have a martensitic transformation temperature of $T_m = 38.84\,\mathrm{K}$. Adesso *et al.* measured the AC magnetic susceptibility on the sample [102], where a single peak was found near $T_c(H)$ in magnetic fields $\mu_0 H = 5\,\mathrm{T}$ and $9\,\mathrm{T}$, which disappeared for fields of $\mu_0 H = 13\,\mathrm{T}$ and above. This is a manifestation of the *peak effect*.

The peak effect in superconductors was first discovered in 1961, when both Berlincourt *et al.* and LeBlanc and Little found a strong increase of the critical-current density near the upper critical field H_{c2} [24, 25]. Pippard explained this behavior by a "softening" of the vortex lattice at elevated temperatures [25]. With increasing temperature T, the shear modulus vanishes as $(T_c - T)^2$ near the critical temperature $T_\mathrm{c}(H)$, while the pinning interactions vary linearly with $(T - T_\mathrm{c})$, thereby leading to an enhanced vortex pinning in a certain narrow range of temperatures near T_c. The peak effect in $\mathrm{Nb_3Sn}$ has attracted much interest, because of the importance to achieve high critical-current densities in $\mathrm{Nb_3Sn}$ for technical applications.

Further studies on the nature of the peak effect in this crystal were communicated by Lortz *et al.* [103], who studied the DC magnetization, and found a noticeable hysteresis in the peak effect region. Additionally, Lortz *et al.* revealed a small peak in the specific heat right before the transition to the normal state by using specific heat measurements with an applied vortex lattice "shaking" field [26] (see Section 3.2). This peak was interpreted as a sign of vortex lattice melting inside the peak effect region. Finally Reibelt *et al.* [88] showed that a small AC magnetic

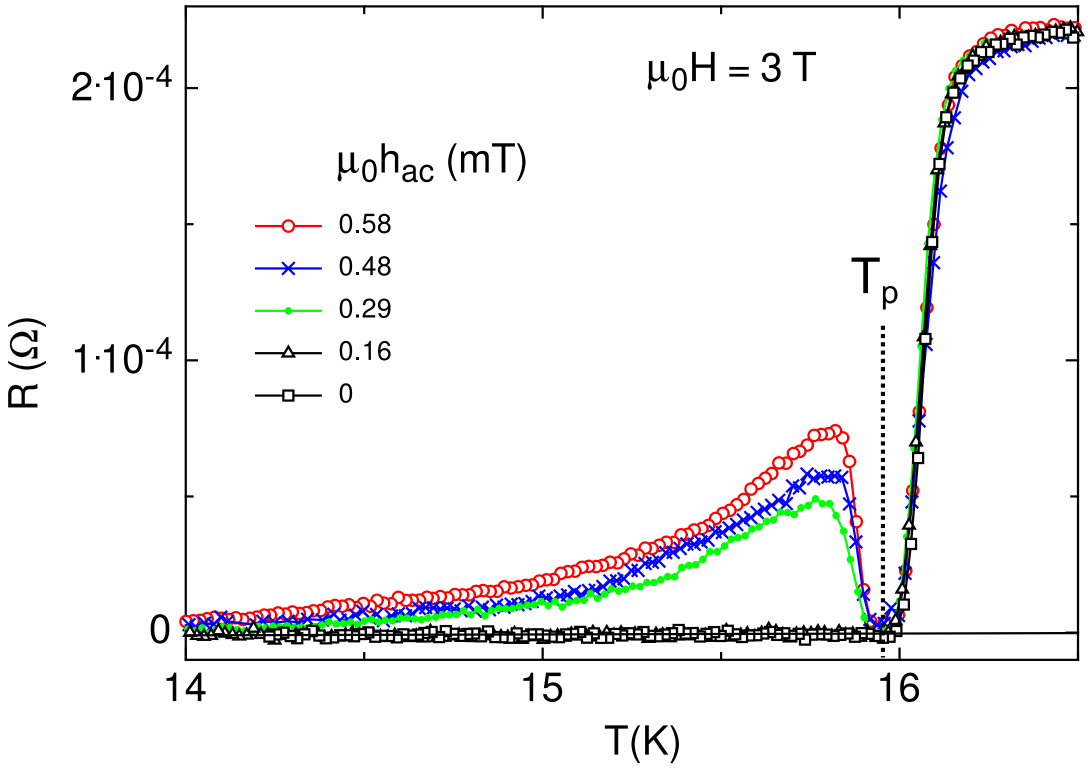

Figure 6.2.: Temperature sweeps $R(T)$ for $\mu_0 H = 3\,\mathrm{T}$, fixed frequency $f = 1\,\mathrm{kHz}$, $I_m = 5\,\mathrm{mA}$, but different amplitudes of the oscillating magnetic field H_0. A dip in the resistivity before the transition to the normal state appears as soon as a threshold amplitude of the "shaking" field H_0 is exceeded. T_p marks the center of the dip in resistance. Adapted from Reibelt *et al.* [88].

"shaking" field can also reveal the peak effect in resistivity measurements, as shown in Fig. 6.2.

6.3. AC Magnetization measurements

We performed a systematic investigation of the AC magnetic susceptibility of the Nb$_3$Sn sample described in the last section in order to refine the results that were reported in Ref. [102]. To summarize; the peak effect manifests itself in a single, distinct peak in the real part $\chi'(T)$ of the AC magnetic susceptibility as a function of temperature T in external magnetic fields above $\mu_0 H \approx 3\,\mathrm{T}$, the size of which continuously increases with increasing magnetic field H (see Fig. 6.5 left column in Section 6.3.6). In the imaginary part $\chi''(T)$ of the AC magnetic susceptibility, on the other hand, a single peak initially grows with increasing H up to a well-defined value, and then splits into two sharp peaks which separate when H is further increased (see Fig. 6.5 left column in Section 6.3.6). We explain this surprising behavior by a flux-creep model and the Bean critical-state model, and taking into account the enhancement of the critical-current density in the peak-effect region near T_c, which we will explain in the following Sections 6.3.1 – 6.3.6.

6.3.1. AC magnetic susceptibility

The strong intrinsic field expulsion of superconductors and the fact that remnant screening currents do not decay through resistive losses makes superconductors ideally suited for magnetization measurements. The magnetic susceptibility χ is defined by the auxiliary Maxwell equation connecting the magnetic flux density $\mathbf{B}$, the magnetic field $\mathbf{H}$, and the magnetization response $\mathbf{M}$ of the sample

$$\begin{aligned} \mathbf{B} &= \mu_0(\mathbf{H} + \mathbf{M}) && (6.1) \\ &= \mu_0(1+\chi)\mathbf{H} && (6.2) \end{aligned}$$

In general χ is a second order tensor unless $\mathbf{M}$ and $\mathbf{H}$ are aligned and if $\mathbf{M}(\mathbf{M})$ is not linear, one can define a differential susceptibility $\chi = \mathrm{d}M/\mathrm{d}H$.

For the following discussion we will treat χ as a scalar, which is justified for isotropic substances. For type I superconductors $\chi = -1$ due to the Meissner-Ochsenfeld effect, but in type II superconductors $\mathbf{M}$ is generally history dependent due to flux pinning (see Section 3.2) and the hysteretic nature of the screening currents. In this case χ is commonly defined as a frequency dependent complex quantity

$$\chi(\omega) = \chi'(\omega) + i\chi''(\omega), \tag{6.3}$$

i.e. using a periodic excitation of the form $\mathbf{H}(t) = \mathbf{H}_0 \cos\omega t$, where ω is the field's angular frequency, we can express Eq. (6.2) as the real part of a complex susceptibility relation

$$\Re\left\{\mathbf{B}_0 \exp i\omega t\right\} = \Re\left\{\mu_0(1+\chi(\omega))\mathbf{H}_0 \exp i\omega t\right\}, \tag{6.4}$$

thereby taking into account both the amplitude difference and the phase shift of $\mathbf{B}(t)$ and $\mu_0\mathbf{H}(t)$ in one complex parameter $\chi(\omega)$.

6.3.2. Demagnetization

The Eq. (6.1) is correct microscopically, but superconducting bodies influence the magnetic field which they are placed in, and therefore the external magnetic field $\mathbf{H}_{\text{ext}}$ and the microscopic $\mathbf{H}_i$ field differ from each other. This can be described by using an additional demagnetization field $\mathbf{H}_D \sim \mathbf{M}$, e.g.

$$\begin{aligned} \mathbf{H}_i &= \mathbf{H}_{\text{ext}} - \mathbf{H}_D \qquad (6.5)\\ &= \mathbf{H}_{\text{ext}} - D\mathbf{M}, \qquad (6.6)\\ \chi &= \frac{\mathrm{d}M}{\mathrm{d}H_i}, \qquad (6.7) \end{aligned}$$

with D the real-valued demagnetization factor, which depends on the sample geometry. For the magnetization, which is measured by an apparatus, the apparent magnetic susceptibility χ_{meas} is then

$$\begin{aligned} \chi_{\text{meas}} &= \frac{\mathrm{d}M}{\mathrm{d}H_{\text{ext}}} = \frac{\mathrm{d}M}{\mathrm{d}H_i}\frac{\mathrm{d}H_i}{\mathrm{d}H_{\text{ext}}}, \qquad (6.8)\\ \frac{\mathrm{d}H_i}{\mathrm{d}H_{\text{ext}}} &= 1 - D\frac{\mathrm{d}M}{\mathrm{d}H_{\text{ext}}}, \qquad (6.9)\\ \Rightarrow \chi_{\text{meas}} &= \chi\left(1 - D\chi_{\text{meas}}\right). \qquad (6.10) \end{aligned}$$

Therefore, one can calculate the actual magnetic susceptibility χ from the measured magnetic susceptibility χ_{meas}, if the demagnetization factor D for the sample geometry is known

$$\chi = \frac{\chi_{\text{meas}}}{1 - D\chi_{\text{meas}}}. \qquad (6.11)$$

By construction, this relationship also holds when both χ and χ_{meas} are complex numbers with real and imaginary parts χ' and χ'', respectively [104].

6.3.3. Magnetic heating

The differential of the free energy density in the presence of a magnetic field is

$$\mathrm{d}f = \frac{\partial f}{\partial T}\mathrm{d}T + \frac{\partial f}{\partial V}\mathrm{d}V - \mu_0 M \mathrm{d}H. \tag{6.12}$$

When the magnetic field H is cycled in the presence of a material with $\chi'' \neq 0$ the change of the free energy density Δf in the material per cycle is given by the enclosed area of the $M(H)$ curve. The $M(H)$ relationship of the form given in Eq. (6.4) is an ellipsis and the energy per cycle can be calculated to

$$\Delta f = -\mu_0 \oint\limits_{\text{cycle}} M(H)\,\mathrm{d}H = \mu_0 \pi \chi'' H_0^2. \tag{6.13}$$

This energy is transferred to the sample with the frequency given by the exciting magnetic field, therefore the heating power due to hysteresis in a sample of volume V is

$$P = \mu_0 \pi f H_0^2 \chi'' V, \tag{6.14}$$

where P is the dissipated power and $f = \omega/2\pi$ is the excitation frequency [105].

6.3.4. Modeling the AC magnetic susceptibility

The existence of a functional relationship between the real and the imaginary part of the AC magnetic susceptibility of superconductors is well known, and explained by a number of theories [106] three of which we will present here.

Resistive model

In the “resistive model” considered by Geshkenbein *et al.* [107], one assumes the sample to be homogeneously resistive with resistivity ρ. The magnetic response of the sample is then caused by eddy currents. Accordingly the in-phase response χ' increases monotonically with ω, but the out-of-phase response is largest when the skin-penetration depth according to the skin effect is on the order of the sample dimensions. For an infinite slab of thickness d, resistivity ρ, and the probing AC magnetic field in parallel to the surface of the slab, the resulting AC magnetic susceptibility is given by [107]

$$\chi' = \frac{\sinh u + \sin u}{u\,(\cosh u + \cos u)}, \tag{6.15a}$$

$$\chi'' = \frac{\sinh u - \sin u}{u\,(\cosh u + \cos u)}, \tag{6.15b}$$

$$\text{with} \quad u = \left(\frac{\mu_0 \omega d^2}{2\rho}\right)^{1/2}, \tag{6.15c}$$

where $\omega = 2\pi f$ is the angular frequency of the ac magnetic field. Both χ' and χ'' are uniquely determined by the dimensionless parameter u, and as such fulfill a universal relationship $\chi''(\chi')$ for all Ohmic slabs of this geometry. This relationship is represented by the green line in Fig. 6.3.

Critical-state model

The resistive model works well for high temperature type II superconductors which stay resistive for a large portion of their phase diagram, but it does not describe the hysteresis effects in superconductors that show zero DC resistance but still have a certain hysteresis due to vortex pinning. A successful model to quantitatively explain the magnetic hysteresis in type II superconductors was introduced by Bean in 1964 [108]. The model assumes that magnetic flux enters a superconductor from the outside, thereby inducing a shielding surface current with critical-current density j_c. When the external magnetic field is reduced or reversed, corresponding surface currents with magnitude j_c but with opposite orientation develop from the surface. The corresponding magnetic susceptibility derived from this model, again for an infinite slab parallel to the AC magnetic excitation field, takes the form [109]

$$\chi' = -1 + \frac{H_0}{j_c d}, \qquad \text{for} \quad H_0 < H^\star \tag{6.16a}$$

$$\chi'' = \frac{4H_0}{3\pi j_c d}, \tag{6.16b}$$

and

$$\chi' = \frac{-j_c d}{4H_0}, \qquad \text{for} \quad H_0 > H^\star \tag{6.16c}$$

$$\chi'' = \frac{j_c d}{\pi H_0} - \frac{j_c^2 d^2}{3\pi H_0^2}, \tag{6.16d}$$

with $H^\star = j_c d/2$. Using Eqs. (6.16) we can express χ'' as a function of χ', thereby eliminating the explicit dependence on j_c, d and H_{ac},

$$\chi'' = \frac{4}{3\pi}\left(\chi' + 1\right), \qquad \text{for} \quad \chi' < -\frac{1}{2} \tag{6.17a}$$

$$\chi'' = -\frac{4}{\pi}\chi' - \frac{16}{3\pi}\chi'^2, \qquad \text{for} \quad \chi' > -\frac{1}{2} \tag{6.17b}$$

This relationship is depicted in Fig. 6.3 as a red line.

Flux-creep model

Brandt noticed that the resistive model and the Bean model can be interpolated using a flux-creep model with a non Ohmic power-law dependence of the electric field E on the current density j [110, 111], i.e.,

$$E{\sim}[j/j_c\left(B\right)]^n, \tag{6.18}$$

where $j_c\left(B\right)$ is the field-dependent critical-current density and n a creep exponent. Eq. (6.18) reproduces Ohms law for $n = 1$, and Bean's critical-state model corresponds to a sudden onset of resistive behaviour for $n \to \infty$ and $j = j_c(B)$. While the complex χ is independent of the amplitude of the probing field H_0 for the resistive model and independent of the frequency of the probing field ω in the Bean model, one can show with a scaling argument that in the case of flux creep χ' and χ'' only depend on a parameter $u \sim \frac{\omega}{B^{n-1}}$ and the geometry of the sample [110], as a consequence the graph of $\chi''(\chi')$ is universal for a given geometry and only depends on the exponent n.

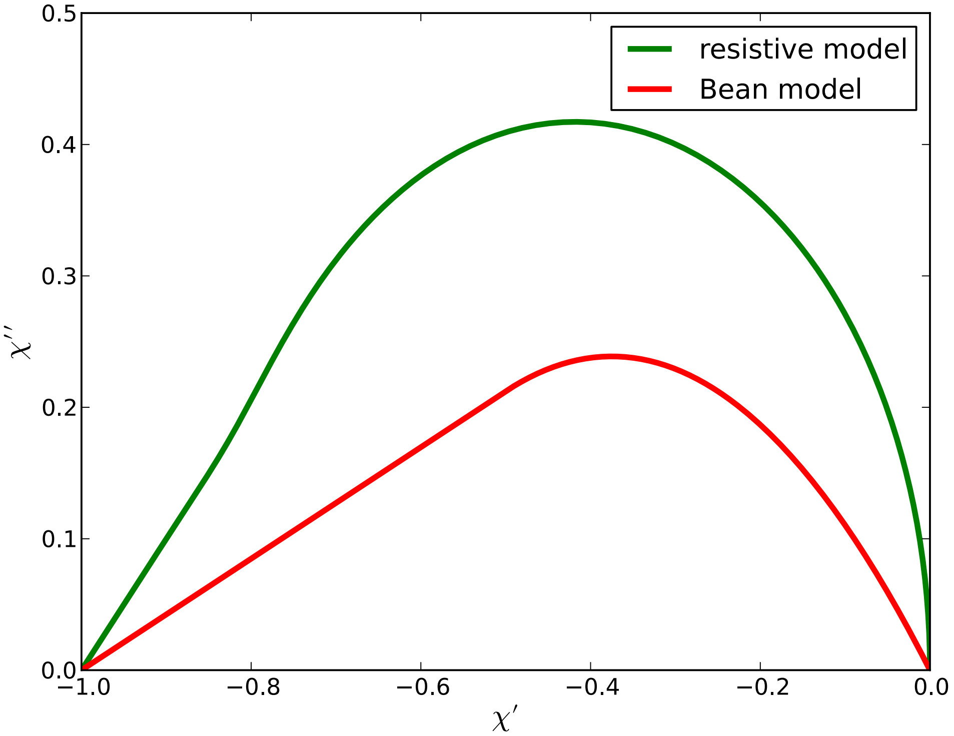

Figure 6.3.: Real part χ' and imaginary part χ'' calculated for an infinite slab in a purely resistive model and according to Bean's critical state model [109]

6.3.5. AC magnetic susceptibility in the peak effect region

Without any peak effect near T_c, the critical-current density $j_c(T)$ would decrease monotonically with increasing temperature T and vanishes at $T = T_c$. As a result, the real part χ' of the magnetic susceptibility also monotonically increases with T before reaching zero at T_c (see Fig. 6.4a, left panel). In the Bean model with a slab geometry, the imaginary part χ'' has a maximum $\chi''_m = \frac{3}{4\pi} \approx 0.239$ for $\chi'_m = -0.375$ (Fig. 6.4a, right panel). For different geometries and creep exponents, different values χ''_m are assumed for slightly different values of χ'_m (e.g., $\chi''_m \approx 0.32$ for $\chi'_m \approx 0.36$ as numerically estimated by Brandt for a finite rectangular bar with a height-to-width ratio of 1 and a creep exponent of $n = 3$ [111], or $\chi''_m \approx 0.417$ for $\chi'_m \approx 0.417$ in the resistive model for a slab geometry.)

If the sample displays a peak effect near T_c, however, the critical-current density increases sharply before dropping to zero at the transition to the normal state. This causes a sudden decrease in $\chi'(T)$, i.e., a peak in $|\chi''(T)|$ (Figs. 6.4b and 6.4c). Depending on the magnitude of this peak (i.e., the pinning strength in the peak-effect region), this will either lead to a single peak in the imaginary part $\chi''(T)$ of the susceptibility if $|\chi'| \leq |\chi'_m|$ (Fig. 6.4b), or to a double-peak structure as soon as $|\chi'| > |\chi'_m|$ in the peak effect region (Fig. 6.4c). The height of these double peaks corresponds to χ''_m (Fig. 6.4c, left panel.)

This remains qualitatively correct even if other models to calculate the AC magnetic susceptibility are used, as long as χ'' is a single-valued function of χ' with a single maximum at some intermediate value of χ'_m as sketched in the right panel of Fig. 6.4a.

6.3.6. AC magnetic susceptibility of Nb_3Sn

To test our scenario we have performed a systematic study of the AC magnetic susceptibility on the $\mathrm{Nb_3Sn}$ sample in external magnetic fields ranging from zero up to $\mu_0 H = 9\,\mathrm{T}$ in steps of $1.5\,\mathrm{T}$, with excitation amplitudes $\mu_0 H_0 = 0.5\,\mathrm{mT}, 1.0\,\mathrm{mT}, 1.5\,\mathrm{mT}$, and $17.0\,\mathrm{mT}$, frequencies $f = 200\,\mathrm{Hz}$ and $f = 1\mathrm{kHz}$, and in a temperature range between $T = 4\,\mathrm{K}$ and $T_\mathrm{c} = 18.2\,\mathrm{K}$. These measurements were done using the ACMS option of a PPMS as described in Section 5.4.1.

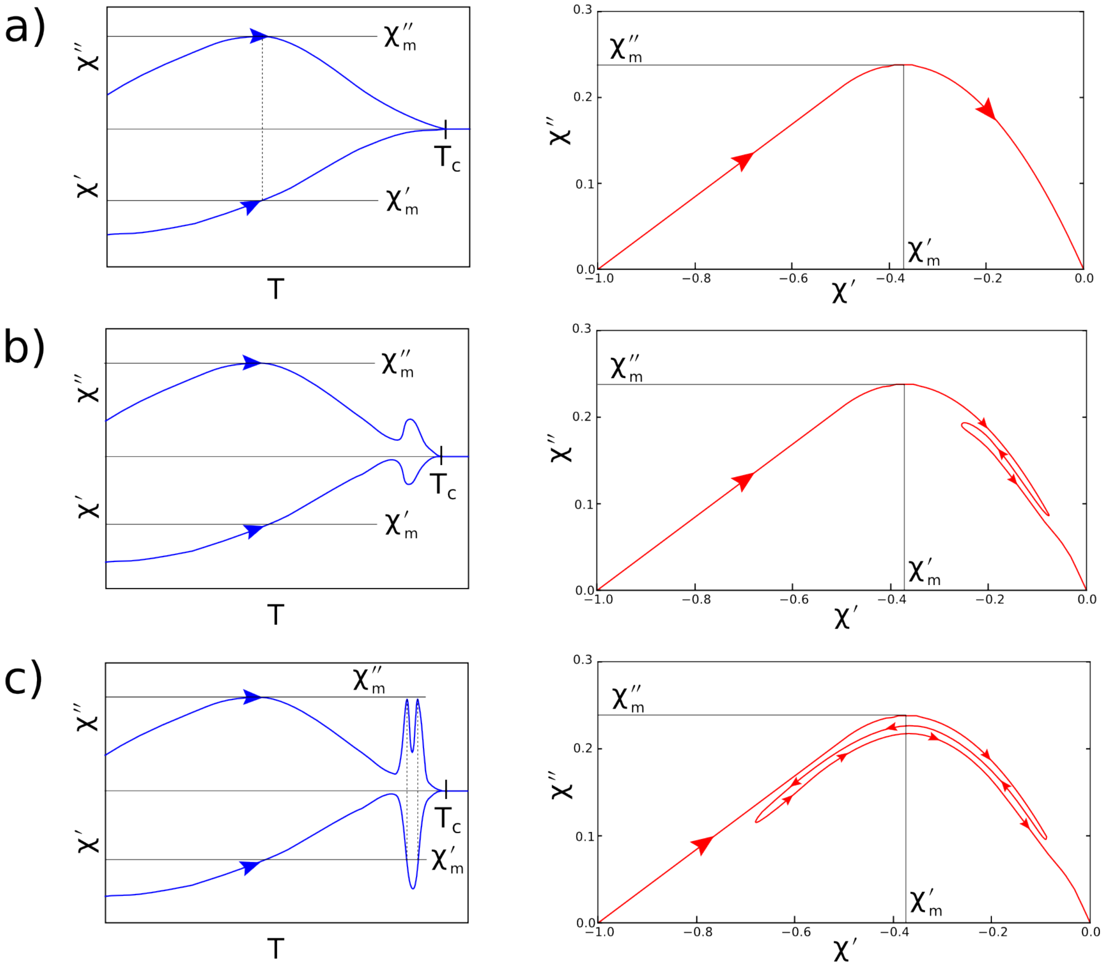

Figure 6.4.: Left panels: Real and imaginary parts of the AC magnetic susceptibility for a superconductor displaying a peak effect. Right panels: corresponding χ'' vs. χ' representations. Arrows indicate an experiment with increasing temperature, for a): a type II superconductor without peak effect; b): a type II superconductor with a weak peak effect, producing single peaks in both real and imaginary parts of the ac magnetic susceptibility; c): a type II superconductor showing a strong peak effect, leading to a single peak in the real part but a double-peak structure in the imaginary part.

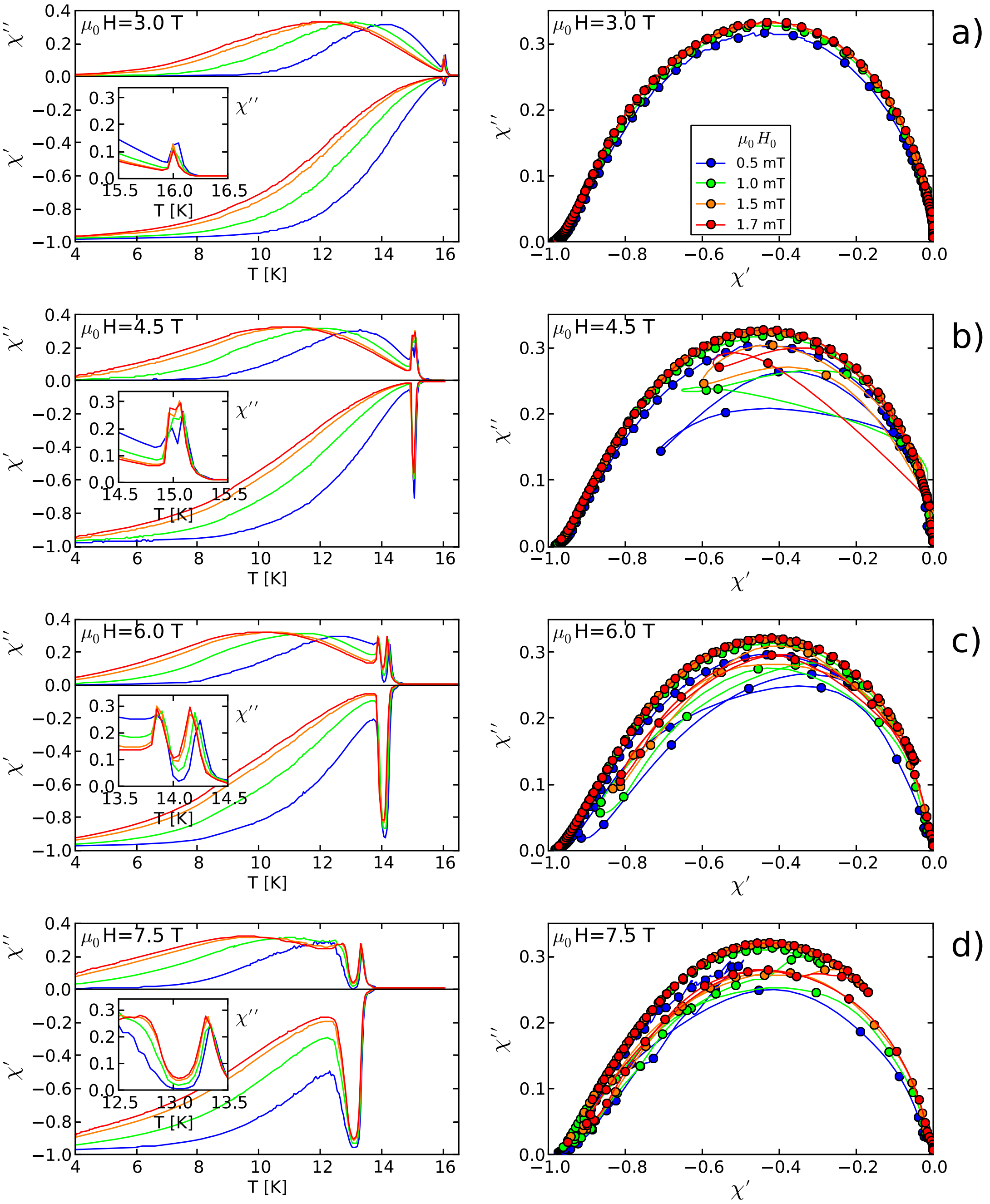

Figure 6.5.: Left panels: AC magnetic susceptibility data of a Nb_3Sn single crystal. The magnetic field $\mu_0 H = 3.0\,\mathrm{T}$ corresponds to case b) in Fig. 6.4, and the data taken in $\mu_0 H = 4.5\,\mathrm{T}$ and above to case c) from Fig. 6.4. Right panels: Corresponding $\chi''(\chi')$ representations, together with interpolating spline fits to guide the eye.

Representative magnetic-susceptibility data of this study are shown in Figs. 6.5. The measured complex AC magnetic susceptibility χ_{meas}-raw-data were corrected according to Eq. (6.11). The factor $D \approx 0.66$ for our crystal was obtained from corresponding AC magnetic susceptibility measurements taken in zero external magnetic field at $T = 4\,\mathrm{K}$ with $\mu_0 H_0 = 1.7\,\mathrm{mT}$ and assuming complete magnetic-flux expulsion, i.e., $\chi' = -1$. This value for D is in reasonable agreement with the geometry of the crystal for which we can estimate $D \approx 0.6 - 0.8$ as calculated for a rectangular prism [112]. Our results for the real part of the AC magnetic susceptibility agree well with the results of Adesso *et al.* [102]. Above $\mu_0 H \approx 3T$, a peak in $\chi'(T)$ starts to form close to T_c, indicating the increase of the critical-current density due to the peak effect (Figs. 6.5, left panels). A corresponding single peak in the imaginary part $\chi''(T)$ appears along with this peak in $\chi'(T)$ and grows with H up to $\mu_0 H = 4.5\,\mathrm{T}$, beyond which it is indeed splitting into two peaks (left panels of Figs. 6.5b - 6.5d.) In the right panels of Fig. 6.5 we have plotted the corresponding χ'' vs. χ' representations. While the results show a negligible dependence on the frequency, there is a considerable dependence on the amplitude as is evident in the data taken in $\mu_0 H = 9\,\mathrm{T}$ and shown in Fig. 6.6.

The overall behavior of $\chi''(\chi')$ outside the peak-effect region can be quite well explained by a universal $\chi''(\chi')$ relationship, particularly for $\mu_0 H = 3\mathrm{T}$. In the narrow peak-effect region for $\mu_0 H = 4.5\,\mathrm{T}$ and above, however, this relationship does not hold exactly, and $\chi''(\chi')$ becomes multi-valued. We can attribute this behavior to the fact that the two regimes inside and outside the peak-effect region belong to two different categories, i.e. different creep exponents n. In Fig. 6.7 we show the quantity $j_c d$ as deduced from the $\chi'(T)$ data within the Bean model and using Eqs. (6.16a) and (6.16c).

Published detailed calculations of and values by Brandt [111] for various sample geometries and creep exponents n had been normalized to -1 in the limit $T \to 0$ using a constant factor instead of applying Eq. (6.11) [111, 113]. To directly compare our measurements with these calculations, we have therefore normalized our χ' and χ'' data in the same way, i.e., by multiplying χ_{meas} with $(1 - D)$. The resulting data for $\chi''(\chi')$ outside the peak effect region reasonably well follows an interpolation by Brandt [111] for a finite bar geometry with a creep exponent $n = 5$ (see Fig. 6.8). Therefore, the $\mathrm{Nb_3Sn}$ crystal must be in a flux-creep regime below the peak effect region, which is also suggested by the investigations

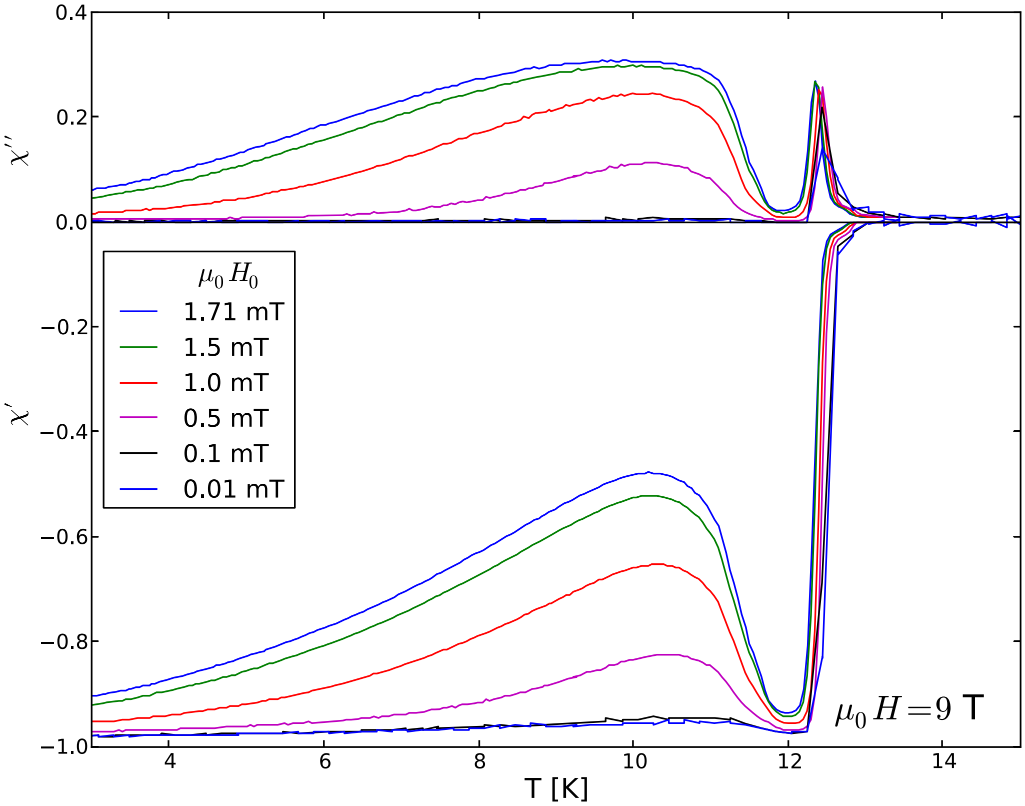

Figure 6.6.: Amplitude dependence of the AC magnetic susceptibility of the Nb_3Sn sample in $\mu_0 H = 9\,\mathrm{T}$. With growing amplitude of the excitation field H_0, the peak effect becomes more and more pronounced.

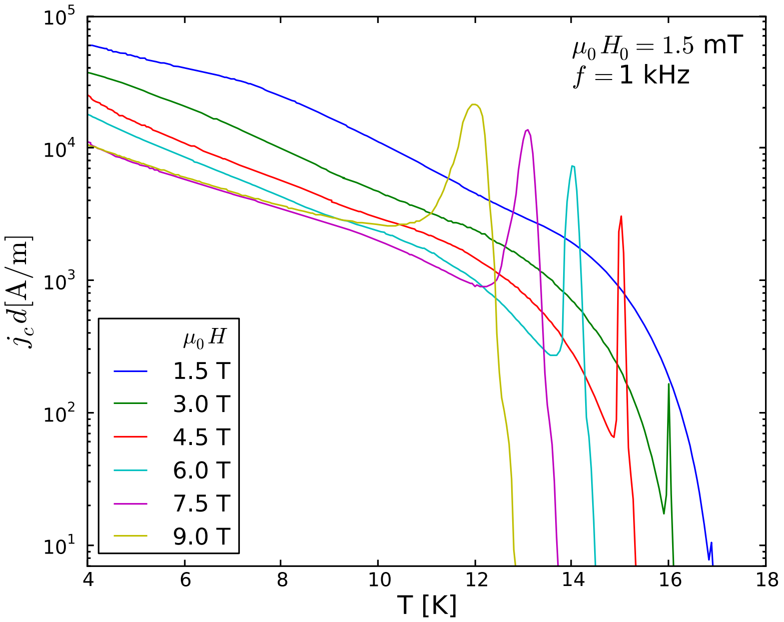

Figure 6.7.: $j_c d$ as calculated according to Eqs. (6.16a) and (6.16c) from the $\chi'(T)$ data displayed in Fig. 6.5 for various external magnetic fields. The peak effect increases j_c by an order of magnitude.

of Reibelt *et al.* on the same sample [88], where the appearance of a finite resistance in an external AC magnetic-excitation field was observed. Once the excitation was removed the resistance dropped again to zero, a behavior which is characteristic for the flux-creep regime [114, 115]. In the peak-effect region, by contrast, the $\chi''(\chi')$ data are closer to the prediction of the Bean model (see again Figs. 6.8), and are reasonably well approximated by a large creep exponent $n = 51$ for a finite bar geometry.

We note here that similar multiple peaks in the pendulum data of several type II superconductors [116, 117] have been explained by D'Anna *et al.* within the critical-state model of Bean for a non-monotonous $j_c(T)$ [116], and our measurements of $\chi''(T)$ partially support this scenario also for Nb$_3$Sn. In Section 6.4.2 we will show that this peculiar double-peak structure in $\chi''(T)$ can also manifest itself in thermal data by the presence of an associated dissipated power according to Eq. (6.14).

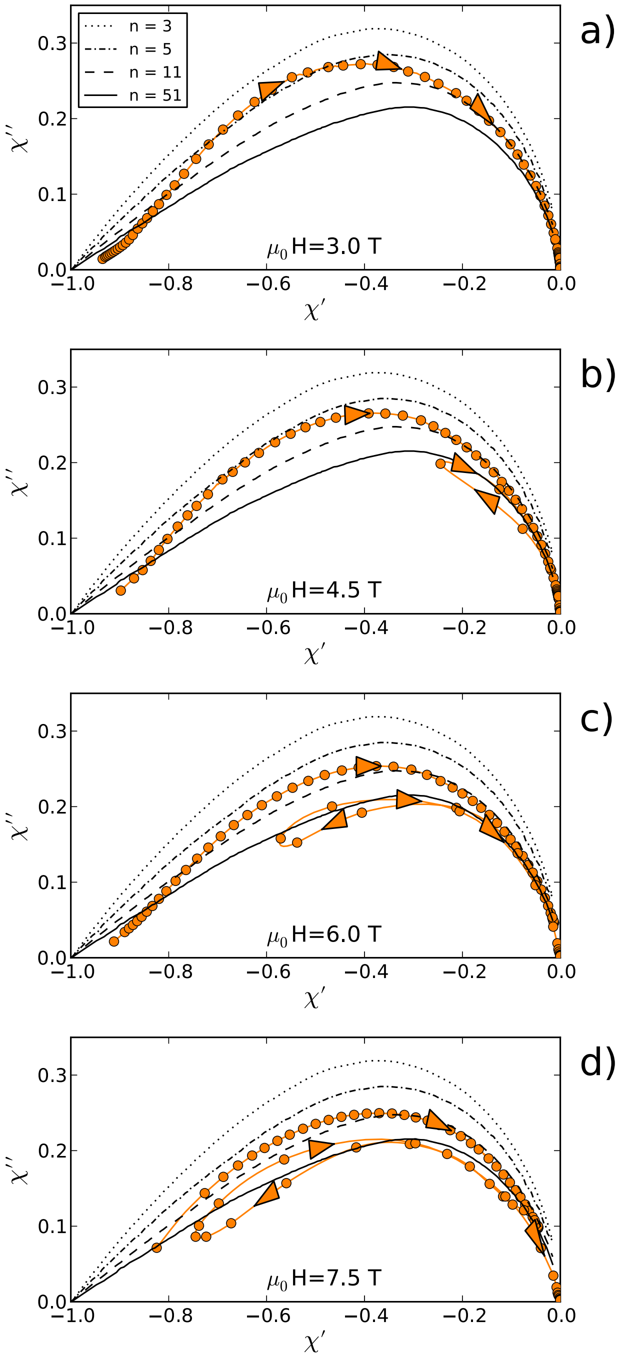

Figure 6.8.: Theoretical expectations for $\chi''(\chi')$ from interpolations according to Brandt [111] for a finite-bar geometry with creep exponents ranging from $n = 3$ to $n = 51$. Only the data for $\mu_0 H_0 = 1.5\,\mathrm{mT}$ are shown here for clarity, together with an interpolating spline fit with arrows to visualize the sequence of the data points.

6.4. Heat capacity measurements

In order to detect a possible vortex lattice melting transition, as claimed by Lortz *et al.* to occur in the same Nb$_3$Sn sample [26], we performed a systematic study of the heat capacity in magnetic fields $\mu_0 H = 0\,\mathrm{T}$ to $9\,\mathrm{T}$. Because the vortex lattice melting transition is of first order, the heat capacity should ideally diverge at the melting temperature $T_m(H)$. Due to the non-ideality of the system, a somewhat broadened peak of finite height is expected to appear, the area of which in a c/T vs. T representation corresponds to the expected melting entropy Δs (see Fig. 3.4).

6.4.1. Heat capacity measurements without vortex shaking

Since it was reported that the melting transition was not detectable in heat capacity measurements without vortex "shaking" [26], we performed similar heat capacity measurements for magnetic fields $\mu_0 H = 0\,\mathrm{T}, 3\,\mathrm{T}, 6\,\mathrm{T}, 9\,\mathrm{T}$, the results of which are depicted in Fig. 6.9. We can confirm that no sign of a first order transition can be detected within the instrumental limits, neither at the temperatures reported for the melting transition [26] nor at the onset of the peak effect region as determined by our AC magnetic susceptibility measurements (see Section 6.3). The sample shows a very narrow transition to the superconducting state $\Delta T(0\,\mathrm{T}) < 0.02\,\mathrm{K}$ and $\Delta T(9\,\mathrm{T}) < 0.5\,\mathrm{K}$, indicating a high crystal quality. In the absence of magnetic fields, the specific heat discontinuity between the specific heat of the superconducting state c_s and that of the normal state c_n, $(c_s - c_n)/c_n \approx 1.33$, which is comparable to the literature value of 1.5 [118] and close to the prediction 1.43 of Eq. (2.18). To evaluate c_n a phononic T^3 term was subtracted. The resulting upper critical field $H_{c2}(T)$ is linear in T, as indicated by the blue line in the phase diagram depicted in Fig. 6.10. The location of the single and double peaks in the χ'' data from the previous section is included in the same phase diagram, as well as complementary data from Reibelt *et al.* showing the peak in DC magnetic hysteresis curves and the center of the peak effect in the resistivity data T_p (see Fig. 6.2).

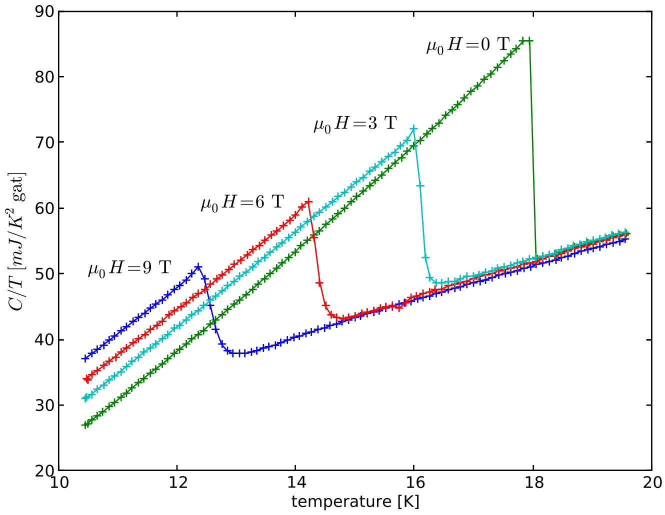

Figure 6.9.: Heat capacity of the Nb_3Sn crystal, measured without vortex lattice "shaking". The specific heat discontinuity associated with the transition to the superconducting state as given by Eq. (2.18) is clearly visible, and shifts with increasing magnetic field linearly to lower temperatures, as expected.

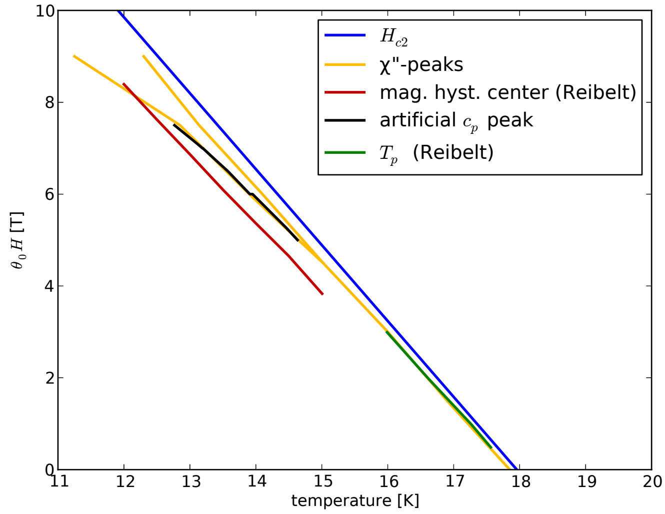

Figure 6.10.: Phase diagram of Nb_3Sn including the "artificial peak in c_p" as discussed in Section 6.4.2, the peaks in χ'', the center of the hysteresis loop in DC magnetic susceptibility measurements, the transition to the superconducting state at the upper critical field H_{c2}, and the center temperature of the peak effect T_p in resistance measurements [88] (see Fig. 6.2).

6.4.2. Heat capacity measurements with vortex lattice “shaking”

We performed an AC calorimetry experiment in magnetic fields $\mu_0 H = 0\,\mathrm{T}$ to $9\,\mathrm{T}$ with an additional “shaking” field H_{ac} perpendicular to the main field, which has been predicted bring the vortex system faster to equilibrium (see Section 3.2). For low “shaking” field amplitudes ($\mu_0 H_0 \lesssim 1\,\mathrm{mT}$) the measured heat capacity is identical to that without “shaking”, but once H_{ac} exceeds a field dependent threshold value $\mu_0 H_0 \approx 4\,\mathrm{mT}$, a peak appears in the calculated heat capacity data calculated according to Eq. (5.7) together with a strong increase of the heat capacity at the transition to the superconducting state. An example of this behaviour is shown in Fig. 6.11. The location of these peak-like structures in the magnetic phase diagram is indicated in Fig. 6.10, and turns out to lie close to the two χ'' peaks in the double peak region of the AC magnetic susceptibility. At a first glance this might be taken as a support for successful detection of a melting entropy analogous to that measured in Ref. [26], but from the analysis data of Chapter 4 using a width at the base of the peak of 60 mK we would expect a peak height of $\approx 2\,\mu\mathrm{J}\cdot\mathrm{K}^{-1}$ about $\approx 30\,\mathrm{mK}$ away from the transition. to the normal state. Not only is the measured peak an order of magnitude higher than expected, but it also depends linearly on the “shaking” field frequency and it increases strongly when the amplitude of the “shaking” field is increased without any sign of saturation. Furthermore, a close inspection of the heat capacity data reveals that the data points are further apart in temperature below the peak than on the peak itself. To understand the origin of these sharp peaks in the heat capacity, we refer to Section 5.2 in which we showed that the strongly temperature dependent self-heating power, $\mathrm{d}P_s/\mathrm{d}T$, affects AC calorimetry data according to Eqs. (6.14) and (5.7). We have therefore measured the corresponding heating power in the calorimeter described in Chapter 5 using an excitation field $\mu_0 H_0 \approx 6.5\,\mathrm{mT}$ in $\mu_0 H = 6\,\mathrm{T}$ for various frequencies f. The results of these measurements are shown in Fig. 6.12 and compared with simulated data according to Eq. (6.14). As the magnetic susceptibility could not be measured in such a large excitation field, we have extrapolated the expected heating power from the measured χ_{meas}-raw-data with $\mu_0 H_0 \approx 1.7\,\mathrm{mT}$ and $f = 200\,\mathrm{Hz}$ using Eq. (6.14), and we reach a reasonable agreement with the measured heating powers.

The strong variation $\mathrm{d}P_s/\mathrm{d}T$ becomes indeed of the same order of magnitude as the heat link k, and leads to an effective k_{eff} as described in Eq. (5.16). If the

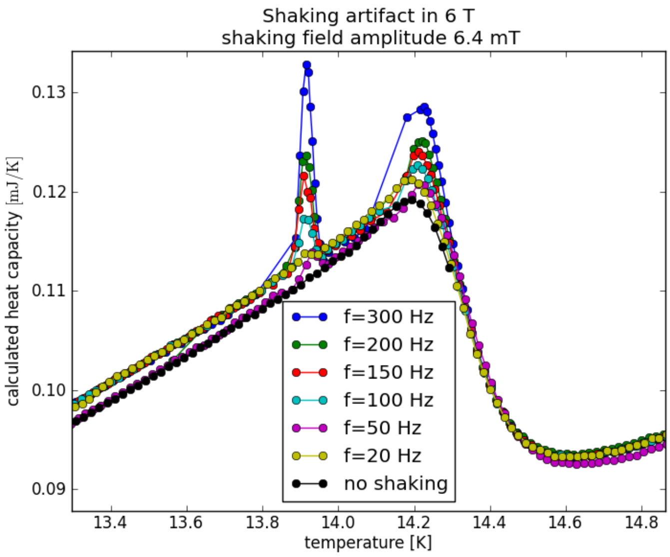

Figure 6.11.: Artificial peak like structure in the heat capacity data calculated according to Eq. (5.7), for measurements on Nb_3Sn sample using vortex lattice shaking. The height of the peak depends linearly on the "shaking" frequency.

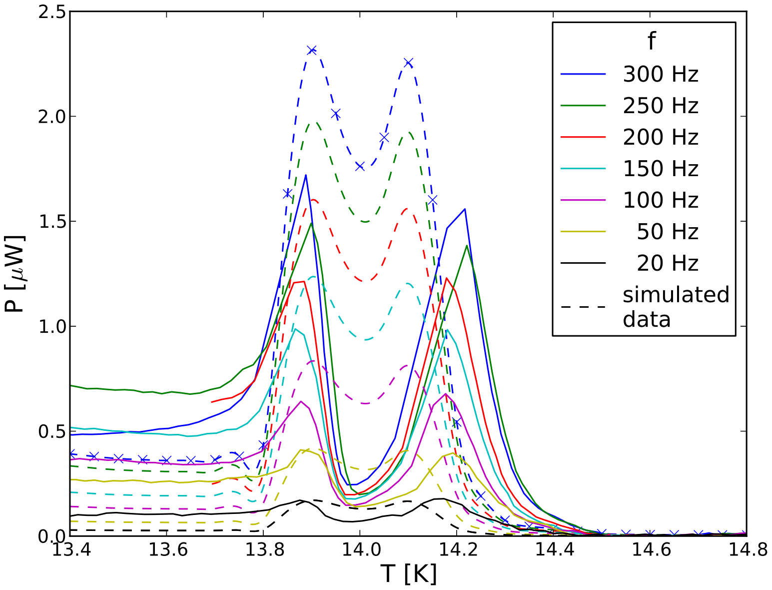

Figure 6.12.: Measured dissipative self-heating power in a Nb_3Sn crystal exposed to a superimposed AC magnetic field with $\mu_0 H \approx 6.5\,\mathrm{mT}$ in $\mu_0 H = 6\,\mathrm{T}$ (solid lines). Corresponding simulated data (dashed lines) were obtained by extrapolation from AC magnetic susceptibility data taken with $\mu_0 H_0 \approx 1.7 mT$ using a B-spline fit through the sampling points indicated by crosses in the simulated data for $f = 300\,\mathrm{Hz}$, and using Eq. (6.14).

heat capacity is then calculated using Eq. (5.7) the unadjusted k will produce artifacts. We expect peaks in regions with large negative $\mathrm{d}P_s/\mathrm{d}T$ and dips in regions with large positive $\mathrm{d}P_s/\mathrm{d}T$. A positive $\mathrm{d}P_s/\mathrm{d}T$ can on the other hand also lead to a runway of the temperature, thereby skipping the temperature region where a dip in the heat capacity would otherwise be measured. Therefore, such dips may escape detection, because the corresponding data points are skipped. This interpretation is also in line with our observation that the data-point density below these artificial peaks is much lower than usual.

If we want to take the self heating into account it is possible to calculate the heat capacity from the amplitude and the phase data of the temperature signal alone using Eq. (5.8), for which we do not need to know k_{eff} as this information is already contained in the phase.

To circumvent the problem that the phase is subject to large errors, we model the unknown finite internal equilibrium time τ to be linear in T (see Section 6.3), and adjust this linear function to a measurement without vortex shaking in such a way that the true physical heat link $k(T)$ calculated using Eq. (5.9) becomes field independent, because the thermal conductivity of copper should show a negligible field dependence below the maximum field $\mu_0 H = 9\,\mathrm{T}$ (see Fig. 6.13).

After applying the correction to the measurement data with “shaking” employed, the heat capacity artifacts almost completely disappear (see Fig. 6.14), verifying our assumption that they are due to the “shaking” induced self heating of the sample.

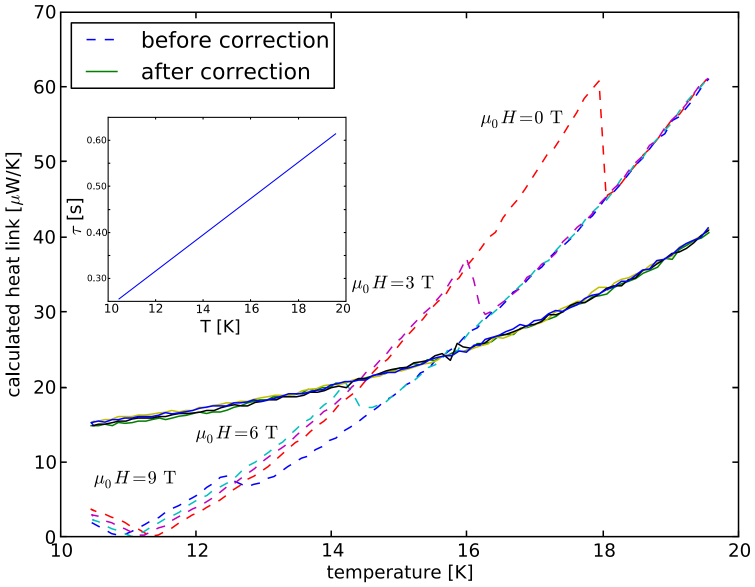

Figure 6.13.: The heat link k calculated using Eq. (5.9) before and after a correction of the phase and the amplitude of the temperature signal for a finite internal equilibrium time $\tau(T)$.

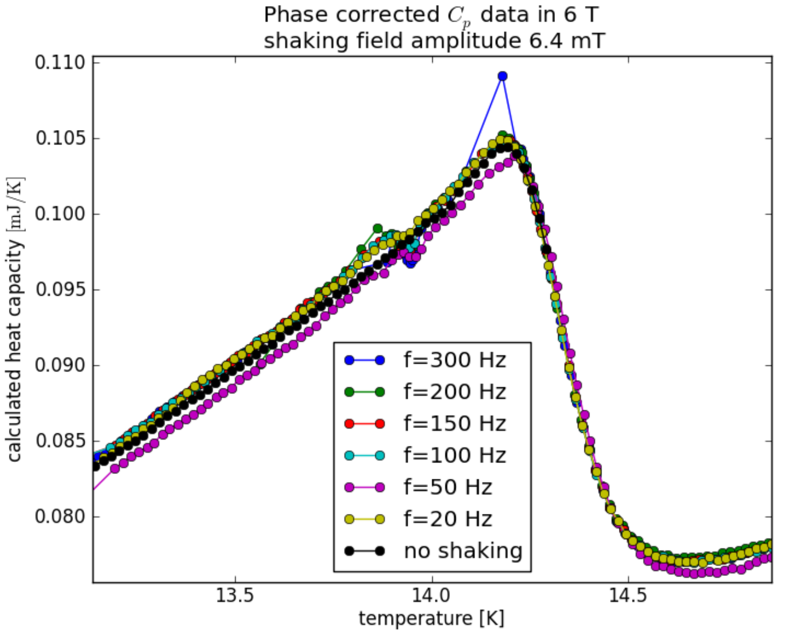

Figure 6.14.: Heat capacity of Nb_3Sn, as calculated from the same data as in Fig. 6.11 and using Eq. (5.8) after a phase correction as described in the text. The first order like peak at 13.9 K has almost completely disappeared.

Physica C 492 (2013) 133–137

Contents lists available at SciVerse ScienceDirect

Physica C

journal homepage: www.elsevier.com/locate/physc

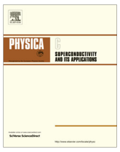

Ac-magnetic susceptibility in the peak-effect region of Nb$_3$Sn

O. Bossen [a,*], A. Schilling [a], N. Toyota [b]

[a] Physik-Institut University of Zurich, Winterthurerstrasse 190, CH-8057 Zurich, Switzerland
[b] Physics Department, Graduate School of Science, Tohoku University, 980-8571 Sendai, Japan

ARTICLE INFO

Article history:
Received 17 April 2013
Accepted 10 May 2013
Available online 28 June 2013

Keywords:
Nb$_3$Sn
Peak effect
Ac magnetic susceptibility
Magnetic properties
Critical current
Vortex pinning

ABSTRACT

We performed a systematic study of the ac magnetic-susceptibility on a Nb$_3$Sn single crystal which displays a strong peak effect near the upper critical field H_{c2}. In external magnetic fields above $\mu_0 H \approx 3$ T, the peak effect manifests itself in a single, distinct peak in the real part $\chi'(T)$ of the ac susceptibility as a function of temperature T, the size of which continuously increases with increasing magnetic field H. In the imaginary part $\chi''(T)$ of the ac susceptibility, on the other hand, a single peak initially grows with increasing H up to a well-defined value, and then splits into two sharp peaks which separate when H is further increased. We explain this surprising behavior by a flux-creep model and taking into account the enhancement of the critical-current density in the peak-effect region near T_c in which Bean's critical-state model seems to apply. Outside this region, the crystal is clearly in a flux-creep regime with finite creep exponent n.

1. Introduction

The peak effect in superconductors was first discovered in 1961, when both Berlincourt et al. and LeBlanc and Little found a strong increase of the critical-current density near the upper critical field H_{c2} [1,2]. Pippard explained this behavior by a "softening" of the vortex lattice at elevated temperatures [3]. With increasing temperature T, the shear modulus vanishes as $(T_c - T)^2$ near the critical temperature $T_c(H)$, while the pinning interactions vary linearly with $(T - T_c)$, thereby leading to an enhanced vortex pinning in a certain narrow range of temperatures near T_c. In 2006 Adesso et al. [4] measured for the first time a corresponding peak effect in the superconductor Nb$_3$Sn. This work was performed on the same single crystal that is under study here, and it has attracted much interest because of the importance to achieve high critical-current densities in Nb$_3$Sn for technical applications. Further studies on the nature of the peak effect in this crystal were communicated by Lortz et al. [5] who studied the dc magnetization and the specific heat in the peak effect region, and by Reibelt et al. [6] who showed that an additional small ac magnetic "shaking" field can reveal the peak effect in resistivity measurements as well.

2. Modelling the ac susceptibility

In ac magnetic-susceptibility measurements a sample is subject to a small oscillating magnetic excitation field with amplitude H_{ac} and frequency f, and the magnetic response of the sample is determined from the induced e.m.f. in a secondary pick-up coil. Both the in-phase response (real part) and the out-of-phase response (imaginary part) of the recorded signal are of interest. Type I superconductors are in the Meissner state and therefore expel the applied magnetic field completely. The ac magnetic-susceptibility $\chi = \chi' + i\chi''$ then has no imaginary part (i.e. no dissipative losses), and the real part is $\chi' = -1$. Type II superconductors in the mixed state, on the other hand, do not expel the magnetic field completely, and they can show considerable magnetic hysteresis due to vortex pinning. Therefore, $|\chi'| < 1$ and $\chi'' > 0$ as soon as $H > H_{c1}$, with H_{c1} the lower critical field. The hysteretic losses are related to χ'' via

$$P = \mu_0 \pi f H_{ac}^2 \chi'' V, \tag{1}$$

where P is the dissipated power and V the sample volume [7].

2.1. Resistive model

For a sample showing Ohmic behavior, the ac magnetic losses stem from the resistive losses of the induced electrical eddy currents. They reach a maximum when the skin penetration depth is of the order of the magnitude of the sample size. For an infinite slab of thickness d, resistivity ρ, and the probing ac magnetic field $H_{ac}(t)$ in parallel to the surface of the slab, the resulting ac magnetic-susceptibility is given by [8]

$$\chi' = \frac{\sinh u + \sin u}{u(\cosh u + \cos u)}, \tag{2a}$$

---

* Corresponding author. Tel.: +41 446355778; fax: +41 446355704.
E-mail address: obossen@physik.uzh.ch (O. Bossen).

0921-4534/$ - see front matter © 2013 Elsevier B.V. All rights reserved.
http://dx.doi.org/10.1016/j.physc.2013.05.028

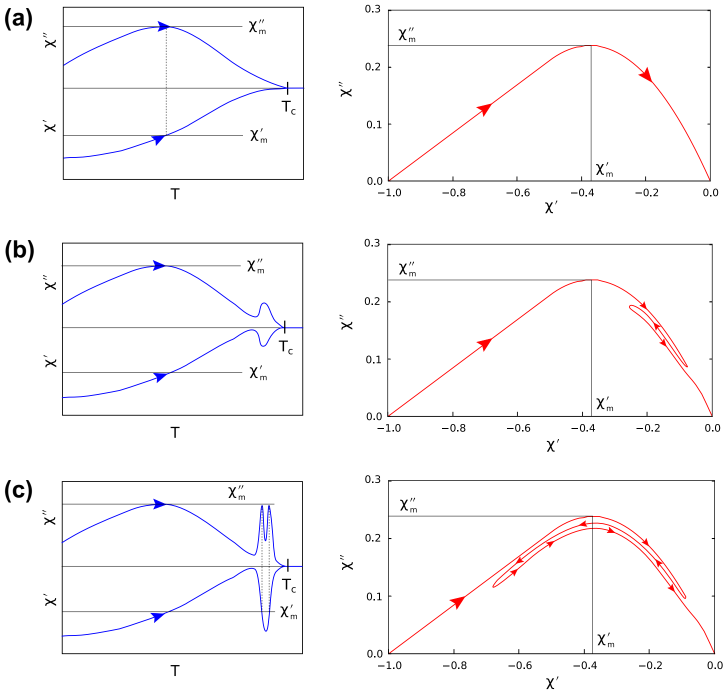

Fig. 1. Left panels: Real and imaginary parts of the ac magnetic-susceptibility for a superconductor displaying a peak effect. Right panels: corresponding χ'' vs. χ' representations. Arrows indicate an experiment with increasing temperature, for (a) a type II superconductor without peak effect; (b) a type II superconductor with a weak peak effect, producing single peaks in both real and imaginary parts of the ac susceptibility; (c) a type II superconductor showing a strong peak effect, leading to a single peak in the real part but a double-peak structure in the imaginary part.

$$\chi'' = \frac{\sinh u - \sin u}{u(\cosh u + \cos u)}, \tag{2b}$$

with

$$u = \left(\frac{\mu_0 \omega d^2}{2\rho}\right)^{1/2}, \tag{2c}$$

where $\omega = 2\pi f$ is the angular frequency of the ac magnetic field. Both χ' and χ'' are uniquely determined by the dimensionless parameter u, are independent of the amplitude H_{ac}, and as such fulfill a universal relationship $\chi''(\chi')$ for all Ohmic slabs of this geometry.

2.2. Critical-state model

A successful model to quantitatively explain the magnetic hysteresis in type II superconductors was introduced by Bean in 1964 [9]. The model assumes that magnetic flux enters a superconductor from the outside, thereby inducing a shielding surface current with critical-current density j_c. When the external magnetic field is reduced or reversed, corresponding surface currents with magnitude j_c but with opposite orientation develop from the surface. The corresponding magnetic susceptibility derived from this model, again for an infinite slab parallel to the ac excitation field, takes the frequency-independent form [10]

$$\chi' = -1 + \frac{H_{ac}}{j_c d}, \tag{3a}$$

$$\chi'' = \frac{4H_{ac}}{3\pi j_c d}, \quad H_{ac} \leqslant H^* \tag{3b}$$

and

$$\chi' = -\frac{j_c d}{4H_{ac}}, \tag{3c}$$

$$\chi'' = \frac{j_c d}{\pi H_{ac}} - \frac{j_c^2 d^2}{3\pi H_{ac}^2}, \quad H_{ac} > H^* \tag{3d}$$

with $H^* = j_c d/2$. Using Eqs. (3a)–(3d) we can express χ'' as a function of χ', thereby eliminating the explicit dependence on j_c, d and H_{ac},

$$\chi'' = \frac{4}{3\pi}(\chi' + 1), \quad \chi' \leqslant -\frac{1}{2} \tag{4a}$$

$$\chi'' = -\frac{4}{\pi}\chi' - \frac{16}{3\pi}\chi'^2, \quad \chi' > -\frac{1}{2} \tag{4b}$$

2.3. Flux-creep model

Brandt [12] noticed that the resistive model and the Bean model discussed above can be interpolated using a flux-creep model with a non Ohmic power-law dependence of the electric field E on the current density j, i.e.,

$$E \propto [j/j_c(B)]^n, \tag{5}$$

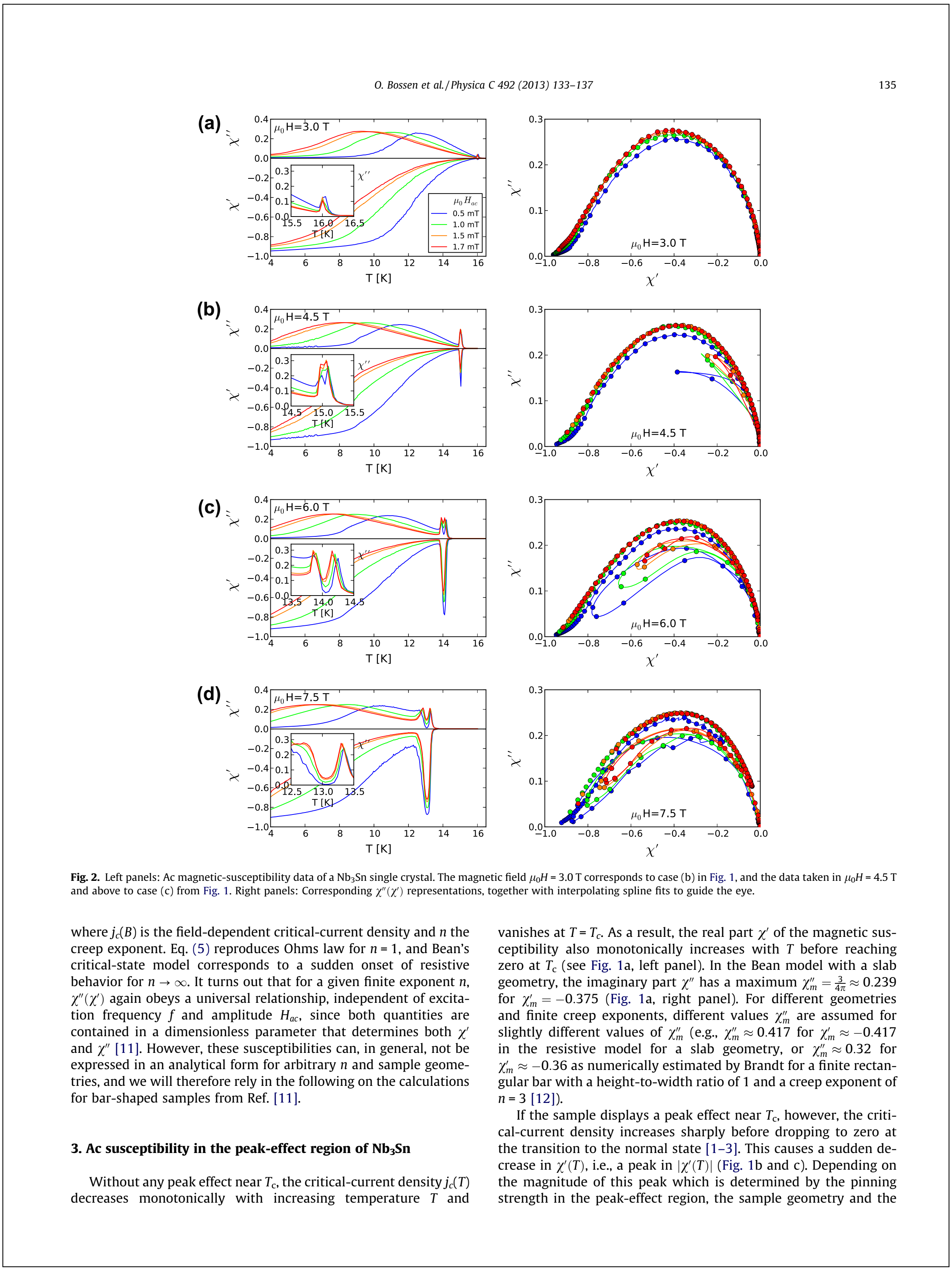

O. Bossen et al. / Physica C 492 (2013) 133–137 135

Fig. 2. Left panels: Ac magnetic-susceptibility data of a Nb$_3$Sn single crystal. The magnetic field $\mu_0 H$ = 3.0 T corresponds to case (b) in Fig. 1, and the data taken in $\mu_0 H$ = 4.5 T and above to case (c) from Fig. 1. Right panels: Corresponding $\chi''(\chi')$ representations, together with interpolating spline fits to guide the eye.

where $j_c(B)$ is the field-dependent critical-current density and n the creep exponent. Eq. (5) reproduces Ohms law for $n = 1$, and Bean's critical-state model corresponds to a sudden onset of resistive behavior for $n \to \infty$. It turns out that for a given finite exponent n, $\chi''(\chi')$ again obeys a universal relationship, independent of excitation frequency f and amplitude H_{ac}, since both quantities are contained in a dimensionless parameter that determines both χ' and χ'' [11]. However, these susceptibilities can, in general, not be expressed in an analytical form for arbitrary n and sample geometries, and we will therefore rely in the following on the calculations for bar-shaped samples from Ref. [11].

3. Ac susceptibility in the peak-effect region of Nb$_3$Sn

Without any peak effect near T_c, the critical-current density $j_c(T)$ decreases monotonically with increasing temperature T and vanishes at $T = T_c$. As a result, the real part χ' of the magnetic susceptibility also monotonically increases with T before reaching zero at T_c (see Fig. 1a, left panel). In the Bean model with a slab geometry, the imaginary part χ'' has a maximum $\chi''_m = \frac{3}{4\pi} \approx 0.239$ for $\chi'_m = -0.375$ (Fig. 1a, right panel). For different geometries and finite creep exponents, different values χ''_m are assumed for slightly different values of χ''_m (e.g., $\chi''_m \approx 0.417$ for $\chi'_m \approx -0.417$ in the resistive model for a slab geometry, or $\chi''_m \approx 0.32$ for $\chi'_m \approx -0.36$ as numerically estimated by Brandt for a finite rectangular bar with a height-to-width ratio of 1 and a creep exponent of $n = 3$ [12]).

If the sample displays a peak effect near T_c, however, the critical-current density increases sharply before dropping to zero at the transition to the normal state [1–3]. This causes a sudden decrease in $\chi'(T)$, i.e., a peak in $|\chi'(T)|$ (Fig. 1b and c). Depending on the magnitude of this peak which is determined by the pinning strength in the peak-effect region, the sample geometry and the

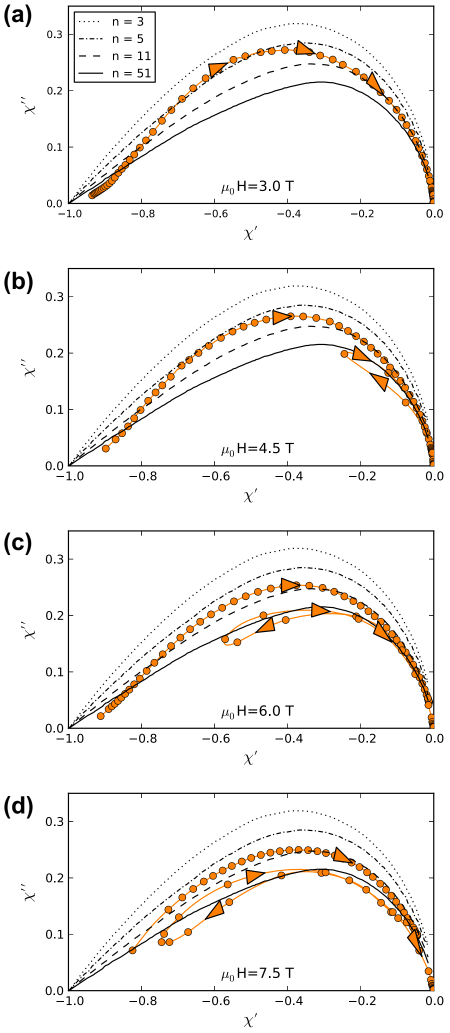

Fig. 3. Theoretical expectations for $\chi''(\chi')$ from interpolations according to Brandt [12] for a finite-bar geometry with creep exponents ranging from $n = 3$ to $n = 51$. Only the data for $\mu_0 H_{ac} = 1.5$ mT are shown here for clarity, together with an interpolating spline fit with arrows to visualize the sequence of the data points.

probing ac magnetic field, this will either lead to a single peak in the imaginary part $\chi''(T)$ of the susceptibility if $|\chi'| \leqslant |\chi'_m|$ (Fig. 1b), or to a double-peak structure as soon as $|\chi'| > |\chi'_m|$ in the peak effect region (Fig. 1c). The height of these double peaks corresponds to χ''_m (Fig. 1c, left panel).

This is the main result of our paper. It remains qualitatively correct even if other models to calculate the ac susceptibility are used, as long as χ'' is a single-valued function of χ' with a single maximum at some intermediate value of χ'_m as sketched in the right panel of Fig. 1a.

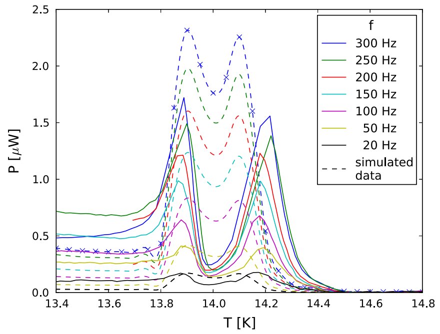

Fig. 4. Measured dissipative self-heating power in a Nb_3Sn crystal exposed to a superimposed ac magnetic field with $\mu_0 H_{ac} \approx 6.5$ mT (solid lines) in $\mu_0 H = 6$ T. Corresponding simulated data (dashed lines) were obtained by extrapolation from ac-susceptibility data taken with $\mu_0 H_{ac} \approx 1.7$ mT using a *B*-spline fit through the sampling points indicated by crosses in the simulated data for $f = 300$ Hz, and using Eq. (1).

To test our scenario we have performed a systematic study of the ac magnetic susceptibility in external magnetic fields ranging from zero up to $\mu_0 H = 9$ T in steps of 1.5 T, with excitation amplitudes $\mu_0 H_{ac} = 0.5$ mT, 1.0 mT, 1.5 mT, and 17.0 mT, frequencies $f = 200$ Hz and $f = 1$ kHz, and in a temperature range between $T = 4$ K and $T_c = 18.2$ K. These measurements were done using the ACMS option of a Physical Properties Measurement System *(Quantum Design)*. The Nb_3Sn crystal was of rectangular shape with dimensions $\approx 3 \times 1.3 \times 0.4$ mm^3.

The measured complex ac-susceptibility χ_{meas}-raw-data must, in principle, be corrected according to

$$\chi = \frac{\chi_{meas}}{1 - D\chi_{meas}} \qquad (6)$$

with D the real-valued demagnetization factor, where both χ and χ_{meas} are complex numbers with real and imaginary parts χ' and χ'', respectively [13]. The factor $D \approx 0.66$ for our crystal was obtained from corresponding ac-susceptibility measurements taken in zero external magnetic field at $T = 4$ K with $\mu_0 H_{ac} = 1.7$ mT and assuming complete magnetic-flux expulsion, i.e., $\chi' = -1$. This value for D is in reasonable agreement with the geometry of the crystal for which we can estimate $D \approx 0.6$–0.8 as calculated for a rectangular prism [14].

Published detailed calculations of χ' and χ'' values by Brandt [12] for various sample geometries and creep exponents n had been normalized to $\chi' = -1$ in the limit $H_{ac} \to 0$ but rather using a constant factor instead of applying Eq. (6) [12,15]. To directly compare our measurements with these calculations, we had therefore to normalize our χ' and χ'' data in the same way, i.e., by multiplying χ_{meas} with $(1 - D)$.

Representative susceptibility data of this study are shown in Fig. 2. Our results for the ac magnetic susceptibility show negligible dependence on frequency, and the real part agrees well with the results of Adesso et al. [4]. Above $\mu_0 H \approx 3$ T, a peak in $\chi'(T)$ starts to form close to T_c indicating the increase of the critical-current density due to the peak effect (Fig. 2, left panels). A corresponding single peak in the imaginary part $\chi''(T)$ appears along with this peak in $\chi'(T)$ and grows with H up to $\mu_0 H \approx 4.5$ T, beyond which it is indeed splitting into two peaks (left panels of Fig. 2b–d.) In the right panels of Fig. 2 we have plotted the corresponding χ'' vs. χ' representations. To compare these data with theoretical predictions and to better visualize the sequence of the data points, we have plotted χ'' vs. χ' for $\mu_0H_{ac} \approx 1.5$ mT in a separate graph for clarity (Fig. 3a–d).

The overall behavior of $\chi''(\chi')$ in the peak-effect region can be quite well explained by a universal $\chi''(\chi')$ relationship, particularly for $\mu_0H \approx 3$ T. In the narrow peak-effect region for $\mu_0H \approx 4.5$ T and above, however, this relationship does not hold exactly, and $\chi''(\chi')$ becomes multi-valued (see right panels of Figs. 2 and 3). We can attribute this behavior to the fact that the two regimes inside and outside the peak-effect region belong to two different categories, i.e. different creep exponents n. The Nb$_3$Sn crystal must be in a flux-creep regime below the peak effect region, which is suggested by the investigations of Reibelt et al. on the same sample [6], in which the appearance of a finite measurable resistance for $\mu_0H_{ac} > 0.3$ mT and $f > 1$ kHz was observed. Once the excitation was removed, the resistance dropped again to zero, a behavior which is characteristic for the flux-creep regime [16,17]. This interpretation is supported by the fact that $\chi''(\chi')$ outside the peak effect region reasonably well follows an interpolation by Brandt [12] for a finite-bar geometry with a creep exponent ranging from $n \approx 5$ in $\mu_0H = 3$ T to $n \approx 11$ in $\mu_0H = 7.5$ T (see Fig. 3, dash-dotted and dashed lines). In the peak-effect region, by contrast, the $\chi''(\chi')$ data are very close to the prediction of the Bean model with a large exponent $n \approx 51$ (see again Fig. 3, solid line [12]).

We note here that similar multiple peaks in the pendulum data of several type II superconductors [18,19] have been explained by D'Anna et al. within the critical-state model of Bean for a non-monotonous $j_c(T)$ [18], and our measurements of $\chi''(T)$ partially support this scenario also for Nb$_3$Sn.

Finally we briefly show that the peculiar double-peak structure in $\chi''(T)$ can also manifest itself in thermal data by the presence of an associated dissipated power according to Eq. (1). We have measured the corresponding heating power in a homebuilt calorimeter using an excitation field $\mu_0H_{ac} > 6.5$ mT in $\mu_0H > 6$ T for various frequencies f. The results of these measurements are shown in Fig. 4. As the magnetic susceptibility could not be measured in such a large excitation field, we have extrapolated the expected heating power from the measured χ_{meas}-raw-data with $\mu_0H_{ac} \approx 1.7$ mT and $f = 200$ Hz using Eq. (1), and we reach a reasonable agreement with the measured heating powers. It must be noted here that the strong variation of the magnetic-heating power with temperature in the peak-effect region ought to be considered in thermal experiments using a simultaneous "vortex-shaking" field in order to prevent artifacts in the resulting heat-capacity data.

4. Conclusion

We have shown that the ac magnetic-susceptibility data of a Nb$_3$Sn sample displaying a peak effect near T_c can be well explained using a flux-creep model with a varying creep exponent n. While an n ranging from 5 to 11 fits our data outside the peak-effect region reasonably well, a large exponent $n \approx 51$ which is close to Bean's critical-state model (i.e., $n \to \infty$) applies within the narrow peak-effect region near T_c. Since the value of the creep exponent does not alter the qualitative behavior of the $\chi''(\chi')$ relationship (with a single maximum at some intermediate value of χ'_m between -1 and 0), a single peak in the critical-current density always produces a single peak in the real part $\chi'(T)$ of the ac magnetic-susceptibility, which is accompanied by either a single peak in the imaginary part $\chi''(T)$ (for $|\chi'| \leqslant |\chi'_m|$) or a double peak (for $|\chi'| > |\chi'_m|$ in the peak effect region), respectively. Depending on the magnitude of the critical-current density in the peak-effect region, the sample geometry and the probing ac magnetic field, single or double peaks in $\chi''(T)$ may occur that are nevertheless manifestations of the same underlying physical phenomenon.

Acknowledgements

This work was supported by the Schweizerische Nationalfonds zur Förderung der wissenschaftlichen Forschung, Grant. No. 20-131899.

References

[1] T.G. Berlincourt, R.R. Hake, D.H. Leslie, Phys. Rev. Lett. 6 (1961) 671.
[2] M.A.R. LeBlanc, W.A. Little, In: Proceedings of the 7th International Conference on Low Temperature Physics, University of Toronto Press, 1961.
[3] A.B. Pippard, Philos. Mag. 19 (1969) 217.
[4] M.G. Adesso, D. Uglietti, R. Flükiger, M. Polichetti, S. Pace, Phys. Rev. B 73 (2006) 092513.
[5] R. Lortz, N. Musolino, Y. Wang, A. Junod, N. Toyota, Phys. Rev. B 75 (2007) 094503.
[6] M. Reibelt, A. Schilling, N. Toyota, Phys. Rev. B 81 (2010) 094510.
[7] J.R. Clem, in: R.A. Hein, T.L. Francavilla, D.H. Liebenberg (Eds.), Magnetic Susceptibility of Superconductors and Other Spin Systems, Plenum Press, New York, 1991, pp. 177–211.
[8] V.B. Geshkenbein, V.M. Vinokur, R. Fehrenbacher, Phys. Rev. B 43 (1991) 3748.
[9] C.P. Bean, Rev. Mod. Phys. 36 (1964) 31.
[10] X. Ling, J.I. Budnick, in: R.A. Hein, T.L. Francavilla, D.H. Liebenberg (Eds.), Magnetic Susceptibility of Superconductors and Other Spin Systems, Plenum Press, New York, 1991, pp. 377–388.
[11] E.H. Brandt, Phys. Rev. B 58 (1998) 6506.
[12] E.H. Brandt, Phys. Rev. B 58 (1998) 6523.
[13] D.-X. Chen, E. Pardo, A. Sanchez, J. Magn. Magn. Mater. 306 (2006) 135.
[14] E. Pardo, D. Chen, A. Sanchez, J. Appl. Phys. 96 (2004) 5365.
[15] E.H. Brandt, Phys. Rev. B 55 (1997) 14513.
[16] D.N. Matthews, G.J. Russell, K.N.R. Taylor, Physica C 171 (1990) 301.
[17] L.P. Ma, H.C. Li, R.L. Wang, L. Li, Physica C 279 (1997) 79.
[18] G. D'Anna, M.-O. André, W. Benoit, Europhys. Lett. 25 (1994) 539.
[19] Y. Kopelevich, A. Gupta, P. Esquinazi, Phys. Rev. Lett. 70 (1993) 666.

7. Thermo-electrical oscillators

In Chapter 4 we have discussed the expected melting entropy of the vortex lattice in common low temperature superconductors. We saw that in certain cases the melting entropy might not be within the resolution limits of todays measurement equipment. Therefore we have decided to explore a radically different experimental design that has the potential to surpass the accuracy of current methods by orders of magnitude.

Calorimetry is an old field in experimental physics, and numerous experimental techniques have been developed for the accurate measurement of heat capacities [94, 119, 120] which we discuss in Chapter 5. The frequently used AC calorimetry technique invented by Corbino [91, 92] and modified by Sullivan and Seidel [93], for example, measures a heat capacity by monitoring the temperature amplitude of a sample that is subject to an oscillating heating power, or, although less common, by measuring an oscillating heat current produced by a Peltier element [121, 122]. Such AC techniques have numerous advantages over other methods, e.g., heat-pulse, differential-thermal-analysis [123] or relaxation techniques [94, 119, 120]. A certain robustness to noise and the possibility to use very small temperature amplitudes stems from the fact that the signal of interest can be separated from the instrumental noise by using a frequency selective filter, such as a lock-in amplifier. To increase the total accuracy even further, the duration of a measurement t_m can be increased at will, and the resulting statistical uncertainty decreases as $t_\mathrm{m}^{-1/2}$ (see Section 7.5).

If a calorimeter could be built where the heat capacity is related to the frequency instead of the amplitude of an oscillation one would retain most of the advantages of the conventional AC techniques, but the statistical uncertainty would decrease much more rapidly [124], i.e., as $t_\mathrm{m}^{-3/2}$. Therefore, the accuracy of such a method would be mainly limited by the stability of the oscillator components, rather than by statistical constraints.

In the following we describe the realization of an oscillating thermo-electrical

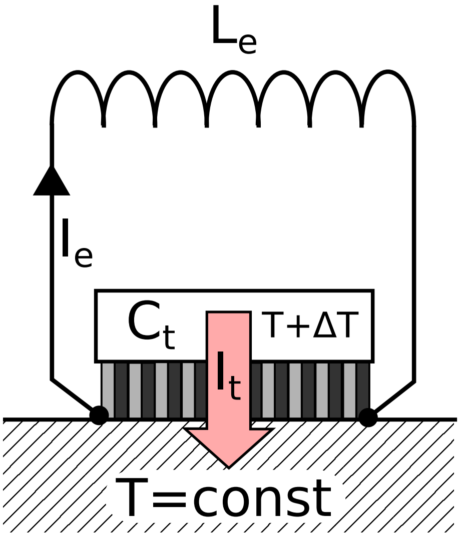

Figure 7.1.: An electrical inductor L_{e} is connected to a Peltier element that separates a heat capacity C_{t} from a thermal bath T. Changes in the electrical current I_{e} induce a temperature difference $\Delta T = L_{\mathrm{e}}\dot{I}_{\mathrm{e}}/\alpha$ (where α denotes the Seebeck coefficient) across the Peltier element that counteracts the variation in the flow of heat $\dot{I}_{\mathrm{t}}$.

circuit using Peltier elements which makes an electrical inductor to effectively act as a “thermal inductor“. The heat capacity can be calculated from the measured resonance frequency of the circuit, and its statistical uncertainty drops according to $t_{\mathrm{m}}^{-3/2}$ as expected.

7.1. Operating principle of a thermo-electrical oscillator

It is known that the flow of heat Q_{t} (with a corresponding heat current $I_{\mathrm{t}} = \dot{Q}_{\mathrm{t}}$) between entities with a certain heat capacity C_{t} through links with a finite thermal conductivity can be mapped onto the flow of charge Q_{e} (with the electrical current $I_{\mathrm{e}} = \dot{Q}_{\mathrm{e}}$) in electrical circuits that is composed of capacitors C_{e} and resistors, respectively, where the temperature T in the thermal case corresponds to the electrostatic potential V in the equivalent electrical circuit. The differential equations describing the time evolution of $Q_{\mathrm{t}}(t)$ or $Q_{\mathrm{e}}(t)$, respectively, are of first order in time t. However, a simple thermal analogue of an electrical inductor involving a higher derivative $\ddot{Q}_{\mathrm{t}} = \dot{I}_{\mathrm{t}}$ does not exist, although the inclusion of terms including $\dot{I}_{\mathrm{t}}$ is justified in certain rare cases [125–128]. Therefore it is impossible to realize autonomously oscillating thermal circuits by using only standard thermal elements.

In our experiment we connect an electrical inductor L_e to a Peltier element as shown in Fig. 7.1. If the heat current I_t through the Peltier element to the thermal bath varies with time, an associated electrical current I_e in the circuit changes according to $\Pi\dot{I}_\mathrm{e} = \dot{I}_\mathrm{t}$, where Π is the Peltier coefficient of the Peltier element. It induces a voltage drop $L_\mathrm{e}\dot{I}_\mathrm{e}$ across the inductor that opposes the changes in the heat current I_t through the Peltier element via the Seebeck effect, i.e., a resulting additional temperature difference $\Delta T = L_\mathrm{e}\dot{I}_\mathrm{e}/\alpha$ (where α denotes the Seebeck coefficient) across the Peltier element is imposed that counteracts the variation in the flow of heat, $\dot{I}_\mathrm{t}$. We can therefore define an effective thermal inductance

$$L_\mathrm{t} := \frac{\Delta T}{\dot{I}_\mathrm{t}} = \frac{L_\mathrm{e}}{\alpha\Pi}\ . \tag{7.1}$$

However, as a consequence of the significant losses produced by the non-zero thermal conductivity and electrical resistance of the Peltier element, the idealized element shown in Fig. 7.1 allows in general only for an over-damped variation of the heat current. This obstacle can be avoided by including an amplifier with a suitable gain in the electrical circuit, and autonomous oscillations can eventually be achieved in this way. In the ideal case of a stationary oscillation with constant amplitude where all losses are exactly compensated by the amplifying element, the electrical circuit behaves like a simple LC circuit with thermal inductance L_t and a heat capacity C_t, or with an electrical inductance L_e and an equivalent electrical capacitance

$$C_\mathrm{e} = \frac{Q_\mathrm{e}}{V} = \frac{\int I_\mathrm{e}\,\mathrm{dt}}{\alpha\Delta T} = \frac{C_\mathrm{t}\int I_\mathrm{e}\,\mathrm{dt}}{\alpha\int \Pi I_\mathrm{e}\,\mathrm{dt}} = \frac{C_\mathrm{t}}{\alpha\Pi} \tag{7.2}$$

and with resonance frequency $\omega^2 = 1/L_\mathrm{t}C_\mathrm{t} = 1/L_\mathrm{e}C_\mathrm{e}$. Therefore, the heat capacity can be derived from ω according to

$$C_\mathrm{t} = \frac{\alpha\Pi}{L_\mathrm{e}\omega^2}\ , \tag{7.3}$$

notably without any need to quantify the thermal and electrical losses in the Peltier element. To the best of our knowledge, the correspondences between an L_e and a thermal analogue L_t, or C_t and a C_e as expressed in Eqs. (7.1) and (7.2), respectively, are novel and have also never been exploited in any calorimetric technique.

7.2. Simulation using the LT-Spice software

LT-SPICE by the company *Linear Technology* is a software from the SPICE *(Simulation Program with Integrated Circuit Emphasis)* family. It allows for the simulation of electrical circuits using solvers for non-linear differential equations, adding typical effects like electrical noise. A plethora of models for commercially available electrical components is available on-line so most conceivable circuits can be tested digitally before production. We have chosen to simulate the interplay of electrical circuits and ”thermal circuits“ using electrical substitute circuits for the latter in order to simulate possible thermal oscillators before building them.

For the simulation of thermo-electrical circuits a model is split into a thermal and an electrical part, set up with the respective electrical and thermal simulation components, and then the thermal components are simulated along with the electrical ones. To connect the electrical and the thermal part of the circuit without unnecessary interference one can construct gateways between the two circuits using virtual current and voltage sources. The most important virtual components of the LT-SPICE software for this type of simulation are the ”voltage dependent current source“, the ”arbitrary current source“, and the ”voltage dependent voltage source“.

For the simulation, the thermal system is set up as an electrical equivalent system. Heat capacities are replaced by electrical capacities that are grounded on one side; heat links are replaced by resistors, and thermal bathes are replaced by voltage sources. The main electro thermal effects that need to be accounted for in an electro thermal simulation are resistive heating, the Peltier effect and the Seebeck effect. Resistive heating can be simulated using an arbitrary current source producing a thermal current from a current through the heating resistor I_R,

$$I_{\text{source}} = RI_R^2. \tag{7.4}$$

This current source is inserted between the ground and the non grounded side of a heat capacity. Seebeck voltages are set up as voltage controlled voltage sources. Using the Seebeck coefficient as a proportionality factor between the "thermal voltage" representing the temperature and the electrical voltage,

$$U_e = SU_T. \tag{7.5}$$

Finally a Peltier effect is simulated by an arbitrary current source where a thermal current is proportional to an electrical current,

$$I_T = \Pi I_e. \tag{7.6}$$

In Fig. 7.2 the full simulation of a system of two Peltier elements with a heat capacity in the center is shown. One Peltier element is used to exploit the Peltier effect, where the source impedance of the rest of the system is much lower than that of the Peltier element, and a second Peltier element is used for a temperature measurement using a high impedance operational amplifier. Therefore the Peltier effect and the resistive heating is simulated only on the input side, and the Seebeck effect is simulated on the output side.

7.3. Experimental setup for a thermal LC oscillator

The actual circuit shown in Fig. 7.3 contains two Peltier elements (MPC-D701, *Micropelt Inc.*) based on Bi_2Te_3, with lateral dimensions of $\approx 3.5\,\mathrm{mm}$ and a thickness of $\approx 1\,\mathrm{mm}$. While the left element acts, together with the sample to be measured, as the equivalent electrical capacitance as described above, the right element is used to compensate for thermal and electrical losses and to maintain a constant amplitude of the temperature oscillation. For this purpose, the voltage across the right element is amplified and then fed onto the electrical contacts of the left element. To achieve a stable oscillation of the desired amplitude, the gain of the amplifier can be controlled using a voltage-controlled gain amplifier (AD630, *Analog Devices*). An additional clamp with Schottky diodes (BAT43) and two potentiometers forms a nonlinear resistor that reduces the gain at large oscillation amplitudes and therefore forces the circuit to self-stabilize.

For a design heat capacity $C_\mathrm{t} \approx 20\,\mathrm{mJ/K}$ to be measured near room temperature

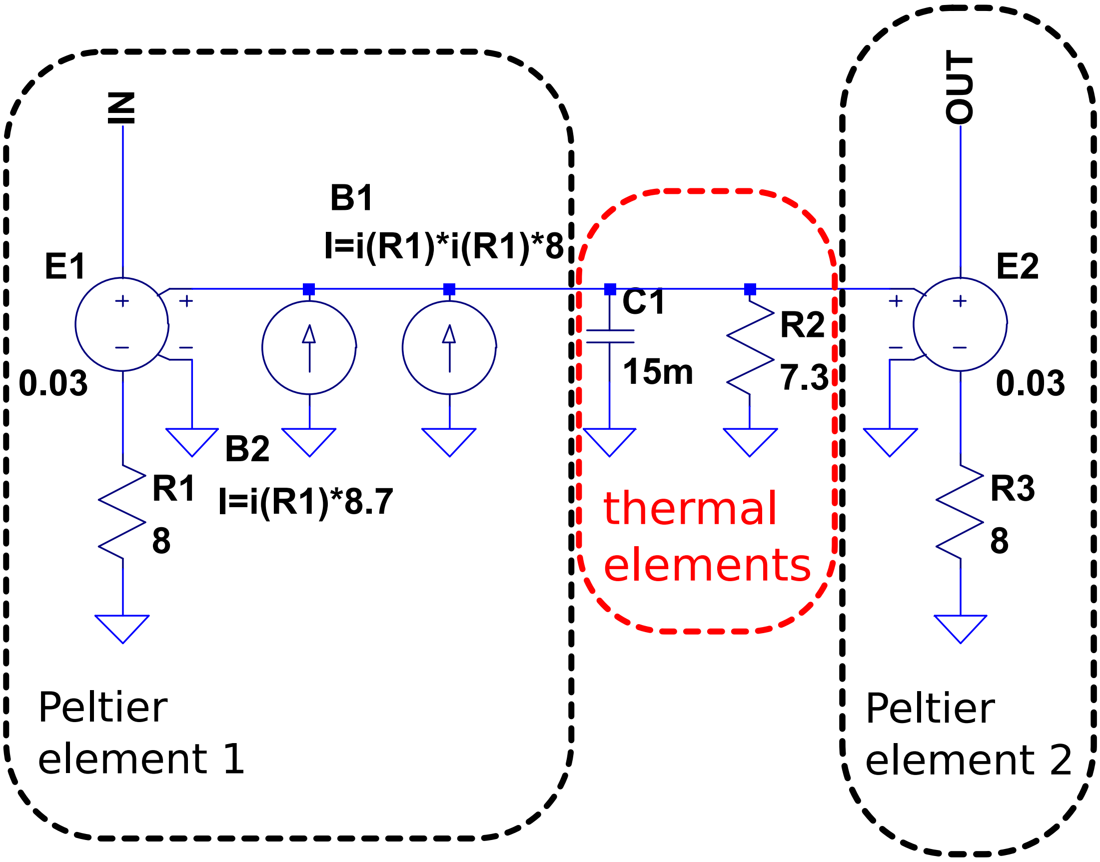

Figure 7.2.: A SPICE simulation of a sample sandwiched between two Peltier elements. On the left side the Peltier element that drives the thermal currents is simulated by a VCVS (voltage controlled voltage source) E1 to simulate the Seebeck effect, a resistor R1 to represent the internal electrical resistance, and two arbitrary current sources B1 and B2 to simulate the resistive heating and the Peltier effect. In the middle, the capacity C1 and the resistor R2 represent the heat capacity of the sample and a thermal link, respectively. On the right side a sensing Peltier element is simulated by a VCVS E2 only, because the electrical currents extracted from it are negligible. The electrical input and output ports are marked as IN and OUT.

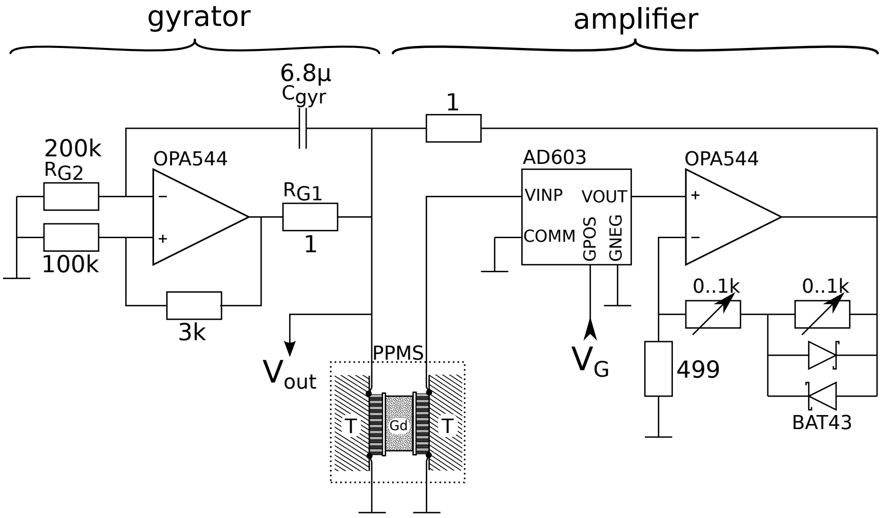

Figure 7.3.: Circuit diagram showing the Peltier element system, the Gyrator to mimic a large electrical inductance, and the amplifier to compensate for thermal and electrical losses (see text). The voltage V_G controls the gain of the amplifier. The two Peltier elements have the same polarity, and the sample is attached to their “top side“. The measured signal is tapped at V_{out}. For the simulation, the parts marked with PPMS are replaced by the circuit in Fig. 7.2.

(which corresponds to $2.87 \cdot 10^{-4}$ mol of a Dulong-Petit solid), and using $\alpha \approx 29\,\mathrm{mV/K}$ and $\Pi \approx \alpha T \approx 8.4\,\mathrm{W/A}$ for the used Peltier elements, the equivalent electrical capacitance becomes $C_e \approx 82\,\mathrm{mF}$. Depending on the heat capacities and the thermal conductivities involved in the thermal part of the system, the frequency of the temperature oscillation must be small enough to allow for a quasi-stationary thermal equilibrium. If we choose $f = \omega/2\pi \approx 0.18\,\mathrm{Hz}$ we need an inductance $L_e \approx 10\,\mathrm{H}$ which would require impractically large passive elements. Therefore we replaced the inductance by a gyrator, the circuit diagram of which is also shown in Fig. 7.3. The effective induction of the gyrator is given by [129] $L_e = (R_P + R_{G1})R_{G2}C_{gyr}$, where the internal resistance $R_P \approx 6.5\,\Omega$ of the Peltier element has to be included here. With $R_{G1} = 1\,\Omega$, $R_{G2} = 200\,\mathrm{k}\Omega$ and $C_{gyr} = 6.8\,\mu\mathrm{F}$ we indeed obtain $L_e \approx 10\,\mathrm{H}$. The gyrator circuit was simulated in LT-SPICE as described in Section 7.2 before being built to ensure that autonomous oscillations are possible, and to study the effects of the non-linear diode stage for the amplitude stabilization. Results of the simulation and a display of actual measurement data of the oscillator is shown in Fig. 7.4.

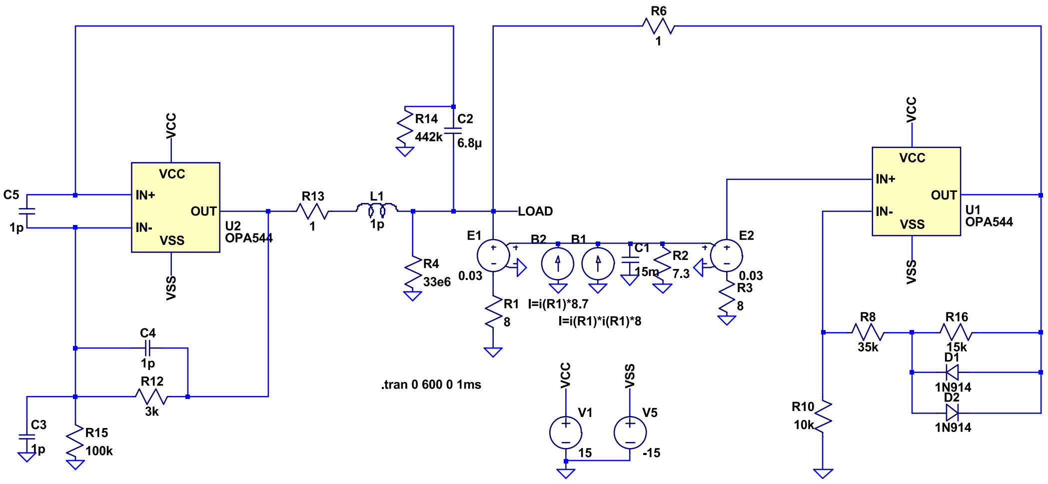

(a) LT-Spice schematic of the gyrator circuit including adjustments for parasitic capacitance and inductance

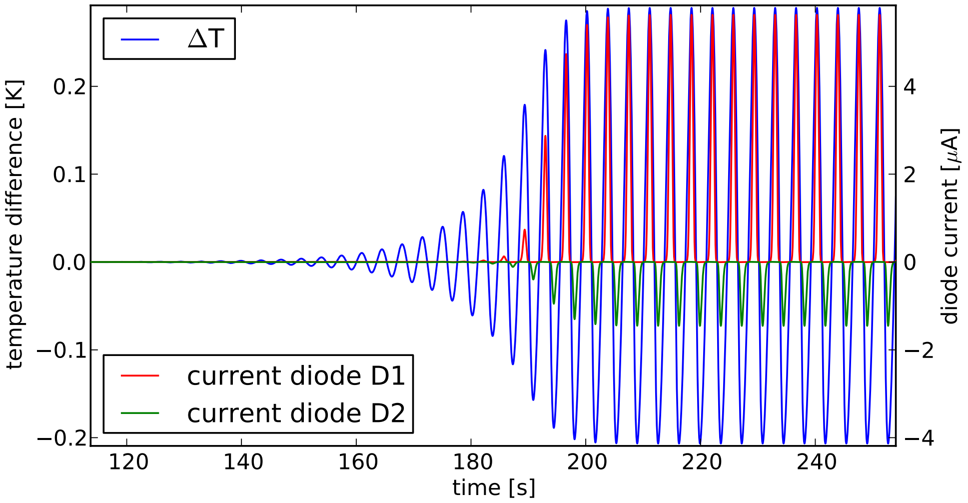

(b) Simulation results: The round trip gain is overunity and causes the oscillations to grow out of random fluctuations until appreciable diode current starts to flow in the diode clamp, reducing the gain to 1 and thus stabilizing the amplitude.

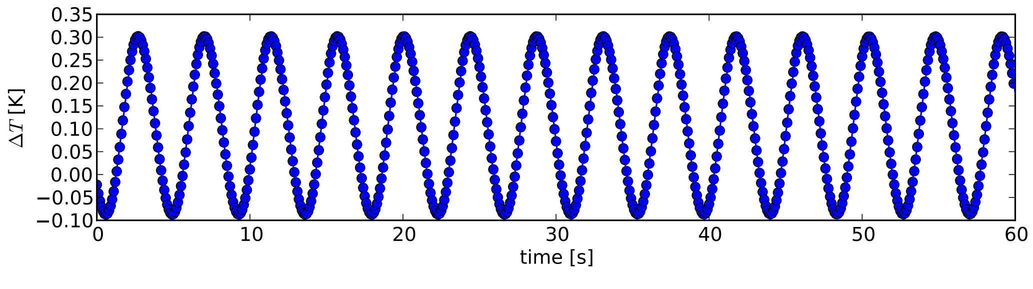

(c) Measured oscillations of the LC-circuit. The solid line is a least-squares fit to a sinusoidal variation of ΔT in time around an offset value that is caused by heat dissipated in the Peltier elements.

Figure 7.4.: The LT-SPICE Simulation of the gyrator compared with an actual measurement.

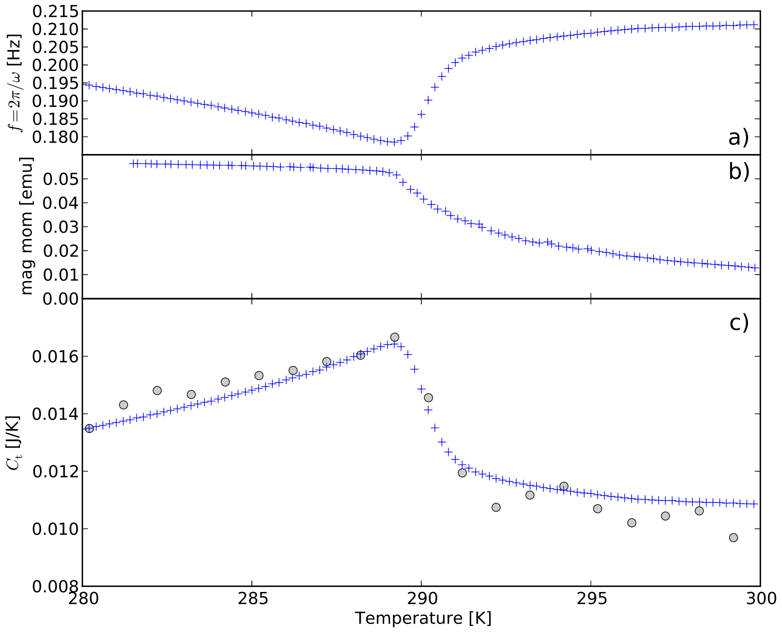

Figure 7.5.: a) Measured frequency of the oscillator b) magnetic moment of the sample measured in a magnetic properties measurement system *(Quantum Design)* illustrating the Curie point of the sample and c) heat capacity of a Gd sample, as functions of temperature. Crosses represent the data that we obtained by the present thermal *LC*-method, while circles denote the values from a measurements on the same sample using a commercial heat capacity system (see text).

7.4. Test measurements

A test sample (45.2 mg or $2.87 \cdot 10^{-4}$ mol of gadolinium with 99.99% purity that had been previously annealed at $T = 1123\,\mathrm{K}$ in vacuum to reduce lattice strains [130]) was sandwiched between the two Peltier elements and placed into a commercial PPMS system (Physical Property Measurement System, *Quantum Design*) for control of the base temperature. The gain of the amplifier was chosen in a way to achieve temperature oscillations with an amplitude of the order of 0.2 K. For each data point, the oscillating voltage was read out during 1200 s with a 10 Hz-triggered Keithley 2001 Multimeter in equal time intervals of 0.1 s (see Fig. 7.4c), and the resulting data were then least-squares fitted to obtain the oscillation frequency (see Fig. 7.5a). To compensate for the heat capacity of the empty system ($\approx$ 15% of the total heat capacity), corresponding measurements have been done without the sample installed. The resulting values of the heat capacity are shown in Fig. 7.5c, together with heat-capacity data obtained on the same sample using the commercial heat-capacity option of the PPMS system and with temperature steps of $\approx 0.5\,\mathrm{K}$. While the heat-capacity data using our thermal *LC*- method are neither smoothed nor further averaged, the PPMS data were averaged over 6 individual measurements. The data-acquisition time for each of the *LC*- method data points was 1200 s, while collecting an averaged PPMS data point took about one hour of time, and the temperature amplitudes for both techniques were comparable, 0.3 K to 0.5 K). The transition of the Gd sample to the ferromagnetic state takes place at the Curie temperature $T_\mathrm{C} \approx 290\,\mathrm{K}$, which is visible in the DC magnetization measurement data which was measured on a MPMS SQUID magnetometer (Magnetic Property Measurement System, *Quantum Design*), and the absolute values for the heat capacity agree well with the PPMS data (see Fig. 7.5b and c).

7.5. Accuracy considerations

The statistics behind the problem of estimating the amplitude A, the frequency ω and the phase φ of an oscillation $A\sin(\omega t + \varphi)$ out of a set of N samples of finite length T has been analyzed in detail in Ref. [124]. Assuming a white noise with variance σ^2, the resulting relative standard deviation σ_A/A in the amplitude A from a measurement of N oscillation cycles with length $T = 2\pi/\omega$ is

$$\frac{\sigma_A}{A} \geq \frac{\sigma}{A\sqrt{N}} \; . \tag{7.7}$$

In a conventional AC technique to measure heat capacities, the relative standard deviation in the heat capacity C_t from the mean value is proportional to the respective standard deviation in the measured amplitude A of a temperature oscillation [91], and therefore the statistical uncertainty in C_t decreases with $t_\mathrm{m}^{-1/2}$ where $t_\mathrm{m} = NT$ is the total time to take such a measurement (in all other conventional methods, the statistical uncertainty also decreases as $N^{-1/2}$, where N is the number of measurements to calculate the average of a data point).

The corresponding relative standard deviation σ_ω/ω in the frequency ω , however,

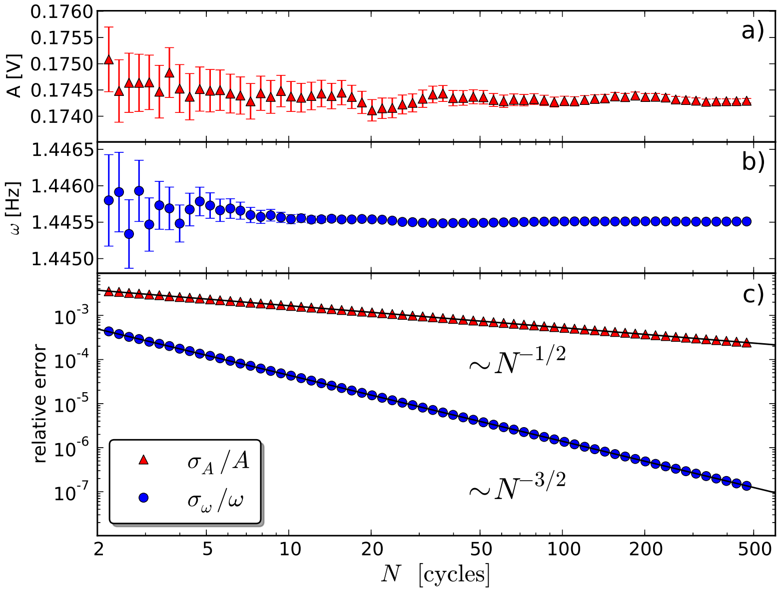

Figure 7.6.: a) Amplitudes and b) frequencies for a selected data point together with the respective standard deviations from the Levenberg-Marquardt fit, as functions of measurement time t_m. c) The respective relative standard deviations on a log-log scale to illustrate the power-law behavior discussed in the text. Solid lines are fits according to $N^{-1/2}$ for σ_A/A and to $N^{-3/2}$ for the σ_ω/ω data, respectively.

varies with N according to

$$\frac{\sigma_\omega}{\omega} \geq \frac{\sqrt{3}\sigma}{\pi A\sqrt{N(N^2-1)}}\,, \tag{7.8}$$

i.e., it decreases with $N^{-3/2}$ (or $t_\mathrm{m}^{-3/2}$) for large N. As the heat capacity in our technique is proportional to ω^{-2} (see Eq. 7.3), the relative standard deviation $\sigma_{C_\mathrm{t}}/C_\mathrm{t} \approx 2\cdot\sigma_\omega/\omega$ also decreases with N in the same fashion. In Fig. 7.6 we show the amplitudes and the frequencies for a selected data point, together with the respective relative standard deviations, as functions of the measurement time t_m which is proportional to the number of oscillation cycles N. The standard deviations σ_A and σ_ω have been taken from a standard Levenberg-Marquardt routine used for least-squares fitting the experimental data. The σ_A/A data decrease relatively slowly with $N^{-1/2}$, while the σ_ω/ω data (and along with them $\sigma_{C_\mathrm{t}}/C_\mathrm{t}$) drop much faster with $N^{-3/2}$ as expected.

Therefore, very high accuracies for C_t can, in principle, be achieved in a comparably very short measuring time. For example, to reduce the statistical uncertainty in C_t by a factor of 10, conventional methods require a 100 times longer duration of a measurement, while the thermal LC method needs only a ≈ 5 times longer data acquisition time. As both σ_A/A and σ_ω/ω are proportional to the same quantity σ/A, there is no hidden drawback in the equation 7.8 that would put this tremendous statistical advantage into perspective. However, in order to tap the full potential of this technique it is essential that the oscillation frequency ω is sufficiently stable during the time of the measurement so that the potentially minuscule statistical uncertainty is not impaired by extrinsic fluctuations, e.g., by an insufficient stabilization of the temperature of the sample or by an unwanted variability in the electronic circuit. While a Levenberg-Marquardt fit always finds some least-squares minimum, with a σ_ω that decreases for increasing t_m, the actual oscillator frequency can be unstable in such a way that repeated measurements under identical experimental conditions lead to different results for the fitted parameters. The quantity σ_ω can therefore not be readily interpreted as the true measurement error of ω.

A standard measure for the stability of an oscillator is provided by the Allan deviation σ_y [131], which is described in the next section. Assuming white noise in the oscillator frequency ω, for example, σ_y is expected to drop as $\tau^{-1/2}$, where τ denotes the time over which the frequency is observed. At large observation times σ_y can saturate or even increase again as soon as other sources of noise (Flicker noise, random-walk noise) become dominant [132]. In our demonstration experiment, no special care has been taken to minimize extrinsic sources for variations in ω. Such sources of error are the decisive factors that are limiting the maximum achievable accuracy in the present thermal LC technique but they are to a large extent controllable, while the intrinsic statistical uncertainty should play a significantly less important role than in conventional techniques to measure heat capacities.

7.5.1. Oscillator noise theory

Phase noise

While the naive treatment of an oscillator signal as a sinusoid plus some white noise ε of the form

$$v(t) = V_0 \sin\left(\omega_0 t + \phi\right) + \varepsilon\left(t\right) \tag{7.9}$$

is instructive, and will also be realized on sufficiently short intervals if the noise introduced between the oscillator setup and the voltmeter dominates, it does not capture large classes of common oscillator noise scenarios, in which noise is included in the feedback loop. For example if we have a wheel spinning around a pivot point with a marker somewhere along the edge, we can regard the vertical position of this marker as an oscillation. If this wheel gets random kicks, turning it faster or slower, or even just moving it by some random angle, this oscillator noise is not well described by an additive contribution to the vertical position, because the amplitude cannot change. In order to describe this type of phase noise one splits the noise into the *amplitude noise* $\alpha(t)$ and the *phase noise* $\phi(t)$ contribution,

$$v(t) = V_0\left(1 + \alpha(t)\right)\sin\left(\omega_0 t + \phi(t)\right) \quad |\alpha(t)| \ll 1, \quad |\phi(t)| \ll 1. \tag{7.10}$$

All autonomous oscillators have a nonlinear element that counteracts the unavoidable energy losses due to electrical resistance or friction. Therefore the amplitude tends to stay very stable after some settling time. For most noise discussions one only restricts oneself to the zero crossings of oscillators, due to the fact that for a typical quartz oscillator the frequency is in the MHz range, and noise effects manifest themselves only over very long time-spans (e.g. several days), making a significant data reduction necessary. To this end the phase noise is written in two new forms, the phase time fluctuation

$$x(t) = \frac{\phi(t)}{\omega_0} \tag{7.11}$$

as well as the fractional-frequency fluctuation

$$y(t) = \dot{x}(t) = \frac{\dot{\phi}(t)}{\omega_0}. \tag{7.12}$$

The advantage of this approach is that with an accurate time signal at hand on can count the time necessary for some fixed number of cycles and obtain $x(t)$ or an average $y(t)$ for a given interval. The temporal development of this parameter can then be recorded over large time spans. To specify the frequency stability of an oscillator one may be tempted to measure the variance or the standard deviation of $y(t)$, but it has been shown that even with high precision oscillators these parameters actually diverge for long term measurements under common noise conditions. In order to mitigate this problem, Allan developed a modified version of the statistical variance with an explicit time dependence [131].

The Allan variance

In 1966 Allan proposed to use the two-sample variance as a measure of frequency stability. The two-sample variance is defined as the expectation value of the variance between neighboring samples

$$\sigma_y^2(\tau) = \mathbb{E}\left\{\frac{1}{2}\left[\overline{y}_{k+1} - \overline{y}_k\right]^2\right\}, \tag{7.13}$$

where the bar denotes a time average, and k is a sample index such that the time difference between adjacent samples is $\tau = t_{k+1} - t_k$. Since theoretic expectation values are not accessible experimentally, an experimental *Allan Variance (AVAR)* is calculated as a simple average:

$$\sigma_y^2(\tau) = \frac{1}{2\,(M-1)} \sum_{k=1}^{M-1} \left(y_{k+1} - y_k\right)^2, \tag{7.14a}$$

or expressed using $x_k = x(t_k)$,

$$\sigma_y^2(\tau) = \frac{1}{2\tau\,(N-1)} \sum_{k=1}^{N-2} \left(x_{k+2} - 2x_{k+1} + x_k\right)^2, \tag{7.14b}$$

where M is the number of considered y samples and therefore $(M-1)$ is the number of considered pairs, just as N is the number of x samples considered and $(N-2)$ is the number of x-triplets. As with the normal variance there is a corresponding standard deviation called *Allan deviation (ADEV)* defined as $\sigma_y(\tau) = \sqrt{\sigma_y^2(\tau)}$.

The overlapping Allan variance

An improvement over the AVAR can be achieved, if the time between recorded samples Δt is smaller than τ, which is almost always the case as one is generally interested in how σ_y^2 depends on τ. One usually calculates σ_y^2 for all multiples of Δt. So only for the minimum $\tau = \Delta t$ we are not oversampling. If we calculate the AVAR for a $\tau = n\Delta t$ we can start at any of the first $n-1$ samples of our set and get a similar result. These results are statistically correlated because the intervals that are used overlap, but nonetheless averaging these results produces an AVAR that is much more smooth for large values of τ. This new AVAR is called *overlapping Allan variance*

$$\sigma_y^2(\tau) = \frac{1}{2n^2\left(M-2n+1\right)} \sum_{j=0}^{M-2n} \left(\sum_{k=j}^{j+n-1} y_{k+n} - y_k \right)^2 , \tag{7.15a}$$

or if $x(t)$ was measured,

$$\sigma_y^2(\tau) = \frac{1}{2n^2\Delta t^2\left(N-2n\right)} \sum_{k=0}^{N-2n-1} \left(x_{k+2n} - 2x_{k+n} + x_k\right)^2 . \tag{7.15b}$$

The modified Allan variance

The AVAR has become the figure of choice for most time metrology applications, because it is easy to calculate and easy to measure, but it is by no means the only way to measure the frequency stability of an oscillator. A number of other parameters can be calculated that have a higher discriminatory power for different types of oscillator noise. A thorough treatment of this is given in Ref. [132]. For us it suffices to introduce one more figure: the *modified Allan variance (MVAR)* by Allan and Barnes [133]. It is calculated as

$$\mathrm{mod}\sigma_y^2(n\Delta t) = \frac{1}{2n^4(M-3n+2)} \sum_{j=0}^{M-3n+1} \left\{ \sum_{i=j}^{j+n-1} \left(\sum_{k=i}^{i+n-1} y_{k+n} - y_k \right) \right\}^2 , \tag{7.16a}$$

or using $x(t)$,

$$\mathrm{mod}\sigma_y^2(n\Delta t) = \frac{1}{2n^4\Delta t^2(N-3n+1)} \sum_{j=0}^{N-3n} \left\{ \sum_{k=j}^{j+n-1} x_{k+2n} - 2x_{k+n} + x_k \right\}^2 . \tag{7.16b}$$

The square root of the MVAR is the *modified Allan deviation (MDEV).* The main advantage of the MVAR is the power to distinguish between noise types on short time scales as we will describe in the next section. It's main disadvantage is the fact that its runtime scales as $\mathcal{O}(M^2)$, and it may therefore take a long time to calculate. This can be improved if the inner averages are calculated using convolutions with rectangle functions, which can be calculated very fast in Fourier space using the convolution theorem and the Fast Fourier Transform (FFT) algorithm.

Noise characterization

Every electronic circuit has noise characteristics that are dominated by frequency independent white noise at high frequencies and some $1/f^\alpha$-noise that dominates the low frequency range with a coefficient α varying with the circuit details and the parameter measured. The exact reason why every electronic measurement system seems to show this behaviour is still under investigation, although in particular cases the noise sources have been modeled successfully. For the phase noise $\phi(t)$ this holds true as well. Different noise processes have been identified in the literature [132, 134] and they lead to different power laws in the one-sided *power spectral density (PSD)* of the phase noise as well as the AVAR and the MVAR. We see in Table 7.1 that the MVAR is able to distinguish between white phase noise and flicker phase noise, while the AVAR is not. Furthermore, in many cases one can see on what time scale which type of noise dominates from the slope in a log-log plot of σ_y^2 vs. τ as shown in Fig. 7.7 for a process containing all noise types listed in Table 7.1, each dominating on different time scales τ.

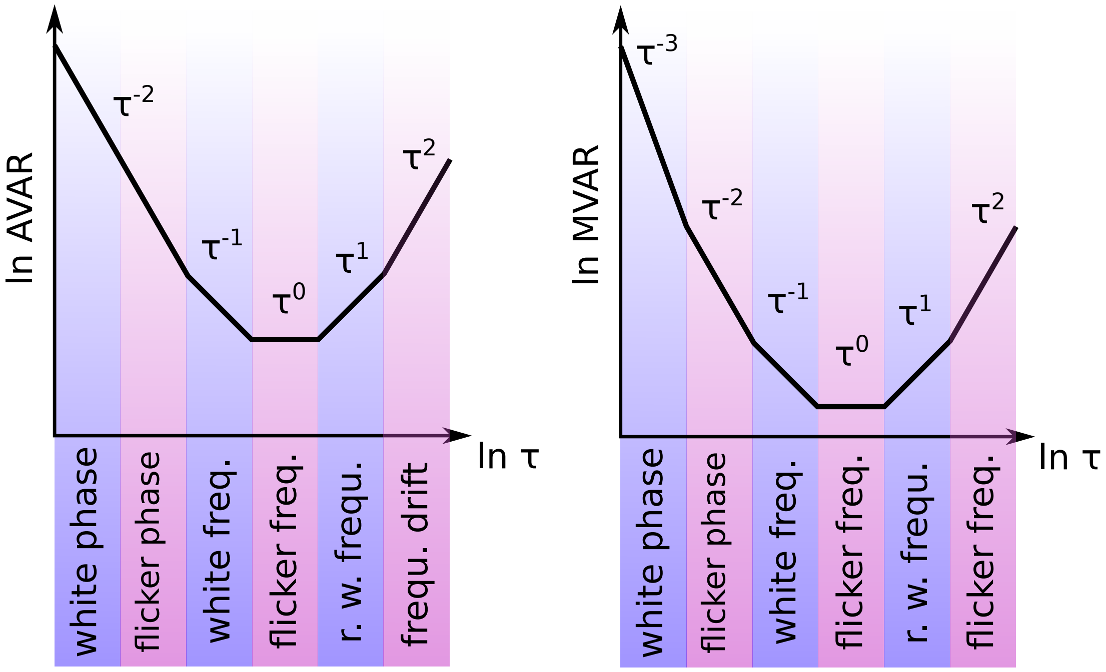

Figure 7.7.: Power law behaviour of the AVAR and the MVAR, for an oscillator that contains different noise sources dominating on different time scales. The distinguishing power between the two types of phase noise makes the MVAR preferable.

Table 7.1.: Power law behaviour of different noise types

noise type	**PSD**$_\phi$	**AVAR**	**MVAR**
white phase	const.	$\sim \tau^{-2}$	$\sim \tau^{-3}$
flicker phase	$\sim f^{-1}$	$\sim \tau^{-2}$	$\sim \tau^{-2}$
white frequency	$\sim f^{-2}$	$\sim \tau^{-1}$	$\sim \tau^{-1}$
flicker frequency	$\sim f^{-3}$	const.	const.
random walk frequency	$\sim f^{-4}$	$\sim \tau^{1}$	$\sim \tau^{1}$
(linear frequency drift)		$\sim \tau^{2}$	$\sim \tau^{2}$

7.5.2. Noise of the electro thermal oscillator

From oscillator data taken with our electro thermal oscillator over a timespan of 409 300 s, (which is about 4 days and 7 hours,) we can determine the overlapping ADEV and MDEV of the oscillator for different time intervals τ as shown in Fig. 7.8. We see that a minimum noise contribution is reached for a timespan of about one hour. Longer measurements will not improve the measurement results due to the intrinsic frequency instability of the oscillator. If we compare this to the previous discussion of the Levenberg-Marquardt fit in Fig. 7.6 which uses a Jacobian approximation as the Hessian of a least squares objective function, to determine the uncertainty of the fit parameters, we have to keep in mind that the fit does only determine how much the sum of squared differences between the fit function and the data changes with varying fit parameters in a local neighborhood. If this sum increases quickly, the fit parameters are assumed to be fitted with a high certainty. Usually this can be translated to a maximum likelihood result as expressed in Eqs. (7.7) and (7.8), but the proof of this requires that the errors are small and of the type of Eq. (7.9), which they are not, as we have just discussed. Therefore, even though the measurement performance of the thermal LC oscillator is very good as the measurements in Fig. 7.5 show, the Levenberg-Marquardt result must not be trusted beyond the accuracy allowed for by the minimum ADEV. When determining the accuracy of actual measured heat capacity values, the reader is advised to determine the noise from the actual fluctuations of the calculated values.

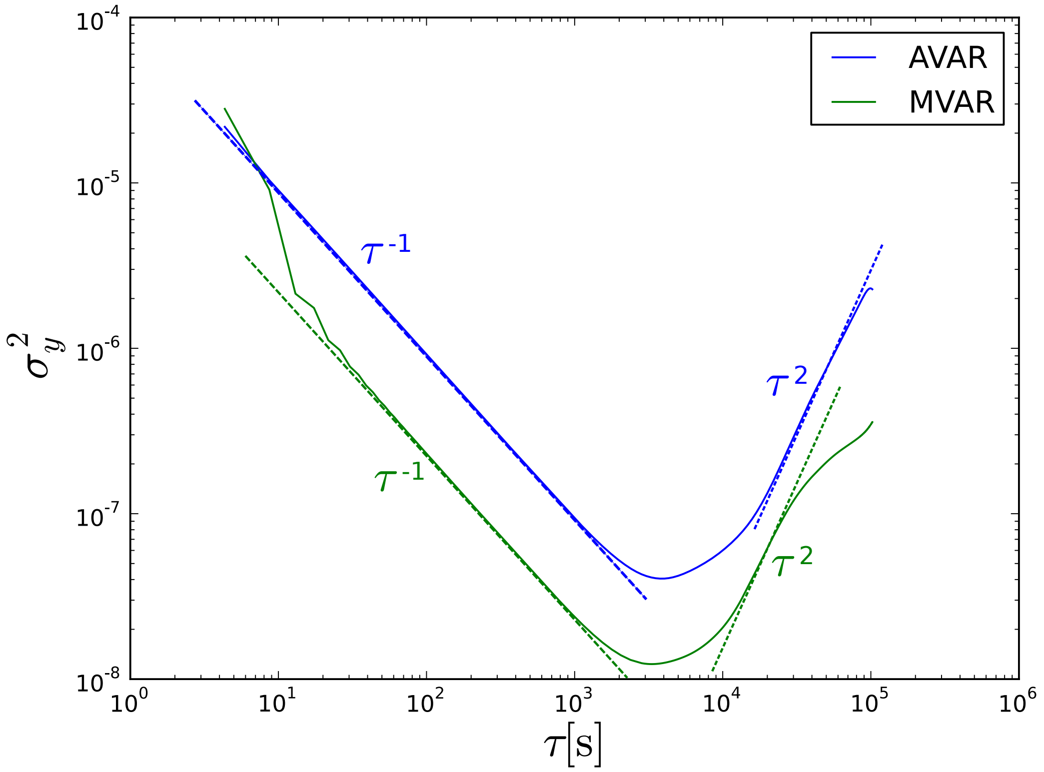

Figure 7.8.: AVAR and MVAR of the electro thermal oscillator. The τ^{-1} dependences show that the measurement is mostly dominated by white frequency noise. The initial difference in slope between the MVAR and the AVAR alludes to minor contributions of white phase noise for very short time intervals. The long term behavior is dominated by frequency drift as the τ^2 contribution indicates.

7.6. Improvements of the oscillator:Extension to low temperatures

After the measurements which were described in the previous sections, the oscillator set-up was further improved to enhance the low temperature performance. The main disadvantage of the LC oscillator setup described in Section 7.3 is the limited temperature range inside which the oscillator can be operated. The asymmetric shift in heating response to an electrical current that is caused by the resistive heating of the Peltier element is becoming larger with lower temperature as the Peltier coefficient decreases with temperature. The thermal current through a Peltier element with an internal resistance R and a temperature difference $\Delta T = 0\,\mathrm{K}$, which is subjected to an electrical current I_e is

$$I_t = \Pi I_e + R I_e^2. \tag{7.17}$$

When the Peltier coefficient decreases at lower temperatures, the resistive heating becomes more dominant, producing an offset in the response $I_t(I_e)$ for an I_e signal that is symmetric around zero, and is limiting the amplitude of I_t to $|I_t| < \frac{\Pi^2}{4R}$. To reduce these resistive effects we have changed the amplifier circuit to allow for an electrical offset current.

A further necessary improvement for the operation at low temperatures is a modification of the diode clamp. In the current configuration the thermal oscillations are limited to a minimum amplitude of 20 mK, because the diodes limit the output oscillation at a voltage of 120 mV below which the non-linearity is too low to prevent the oscillation from decaying. To achieve diode action at lower temperature amplitudes, the Seebeck signal needs to be amplified, but this in turn produces larger round trip gains and thus would fail to produce smaller oscillations. The solution to this problem is an adjustable damping stage. The corresponding electrical circuit is displayed in Fig. 7.9. Two potentiometers on the same axis serve to adjust the amplification and the damping at the same time, ideally making the expansion/compression of the voltage signal in the diode stage adjustable orthogonally to the total gain. The amplitude achievable with this compression stage is $\approx 0.7\,\mathrm{mK}$. The present version of the LC circuit oscillator amplifier also contains a switch to control the gyrator resistor which allows one to choose the oscillation frequency. The complete circuit diagram of the improved oscillator amplifier is

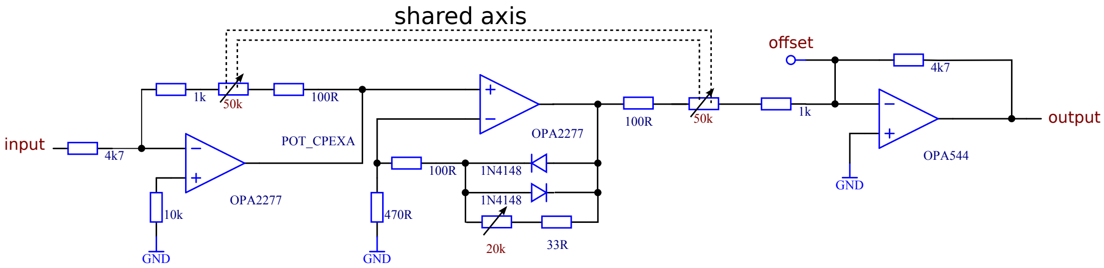

Figure 7.9.: Adjustment circuit for the diode clipping. The adjustable gain of the central stage is reduced as soon as the corner voltage of the diodes is reached. The first and the last stage counteract each other. When the first stage has a gain of G the last stage has a gain of $1/G$, hence only the voltage amplitude of the diode stage and therefore the clipping level is changed by the 50k potentiometers, but not the total gain.

shown in appendix section A.1. Using these improvements, oscillations could be produced down to about $T = 120\,\mathrm{K}$. Since the Peltier elements are not designed for low temperature operations, however, useful measurements could only be performed down to about $T = 190\,\mathrm{K}$, below which the Peltier response shows strong irregularities of unknown origin.

7.6.1. A thermal phase shift oscillator

The thermal oscillator described in Sections 7.3 and 7.4 is limited in the useful temperature range by the poor low-temperature performance of the Peltier elements. It is possible to use a different oscillator design for the realization of an electro thermal oscillator at cryogenic temperatures that does not rely on the use of Peltier elements.

Replacing the Peltier elements

Replacing the Peltier elements poses three challenges that need to be met:

1. An output voltage needs to be generated which changes linearly with the sample temperature
2. The sample should be heated with a heating power proportional to the inflowing current

3. The sample must cool under the influence of a reverse current

The first point is trivially solved using a resistive temperature sensor and a current source. The second point can be fulfilled by using a square rooter circuit. Such a circuit can be build in a number of ways, we have chosen to use an operational amplifier to functionally invert a four quadrant amplifier with connected inputs. The third point is solved by adding a permanent current offset to a heating resistor. If no voltage is applied, the sample will heat up to some temperature offset from a thermal bath to which it is connected through a heat link. Positive and negative voltages produce either a heating through added heating current, or to a cooling through the heat link by reducing the offset heat. The SPICE simulation of the setup is displayed in Fig. 7.10.

7.6.2. The electrical Phase Shift Oscillator (PSO)

The device described in Section 7.6.1 now acts as an electrical low pass unit. The LC-oscillator design requires a gyrator designed for fairly large currents, a large capacitor, a power amplifier and large heat sinks. To circumvent these requirements we employed a *phase shift oscillator (PSO)* design for this new oscillator. PSOs are based on the phase shifting properties of cascaded low pass filters. First order low pass filters can shift the phase of an input signal by up to 90°. Behind the low pass filter, an amplifier equalizes the low pass losses and provides a low impedance output for the next low pass stage. Chaining three of these low passes together provides for a frequency dependent phase shift of up to 270°. To complete the round trip phase to 360°, in order to meet the Barkhausen criterion for stable autonomous oscillation, it is followed by a 180° inverter stage, again with a diode clamp to produce the non-linearity required to stabilize the amplitude. If the loop is closed this oscillator already oscillates autonomously.

7.6.3. Performance of the thermal PSO

The electrical PSO described in Section 7.6.2 becomes a measuring device for heat capacity by connecting the previously described thermo electrical low pass unit between the output and the input of the PSO. This device produces autonomous oscillations that depend on the heat capacity of a sample, and can be operated

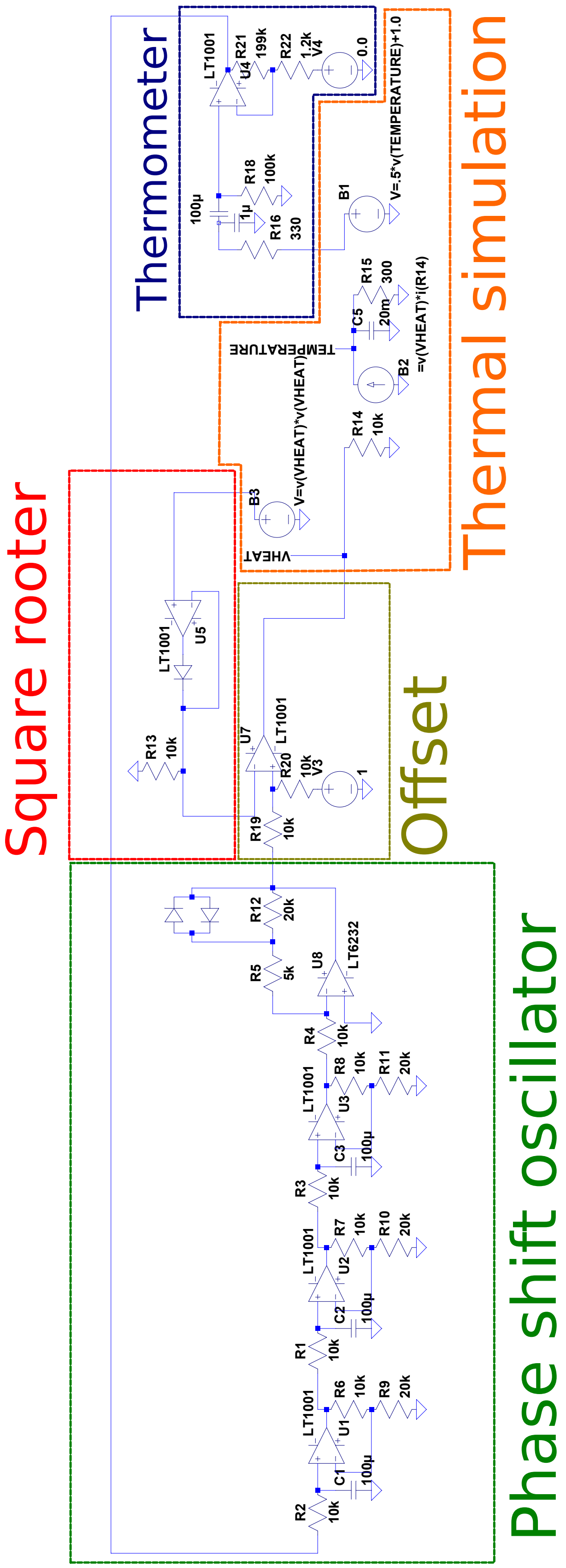

Figure 7.10.: Schematic of the thermal PSO as simulated in `LT-SPICE` (see text).

at any temperature where the resistive thermometer works. We show the results of corresponding test measurements in Fig. 7.11a, showing the general efficacy of the setup by demonstrating a frequency jump of the oscillation due to the heat capacity change of a Nb_3Sn sample at its transition to the superconducting state. Unfortunately, the accuracy that is achieved is severely limited by the so called Leeson effect: Any amplifier noise of an oscillator circuit becomes low pass filtered and amplified through temporal integration [134]. In our case the resulting low frequency noise is so strong that it swamps the oscillation signal unless unreasonably high amplitudes are used (see Fig. 7.11b). Therefore, we have not yet achieved accuracies that are comparable or even better than the traditional low temperature heat capacity measurement techniques, but nonetheless it may be possible that thermal oscillators surpass traditional methods in accuracy once the noise sources are better understood and controlled.

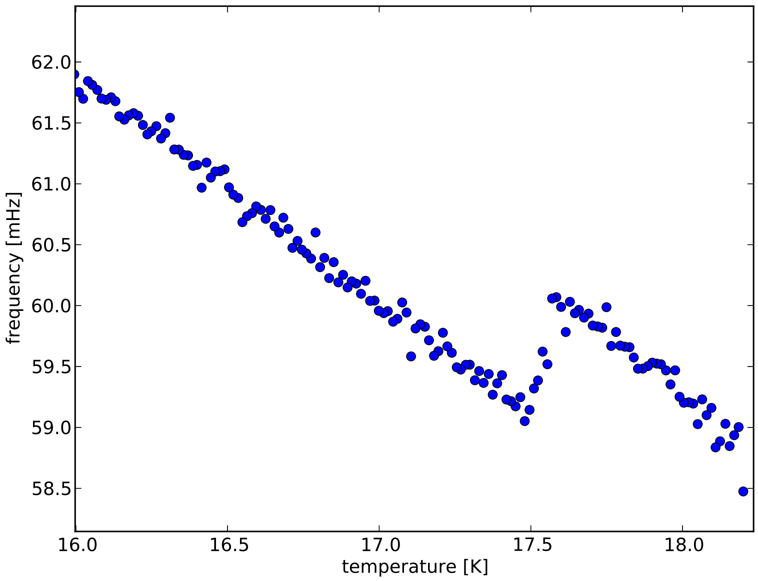

(a) The oscillator frequency can be used to detect the superconducting phase transition of a Nb_3Sn sample. The drop in the heat capacity at $T_c = 17.5\,\mathrm{K}$ (bath temperature) causes an increase in the oscillator frequency.

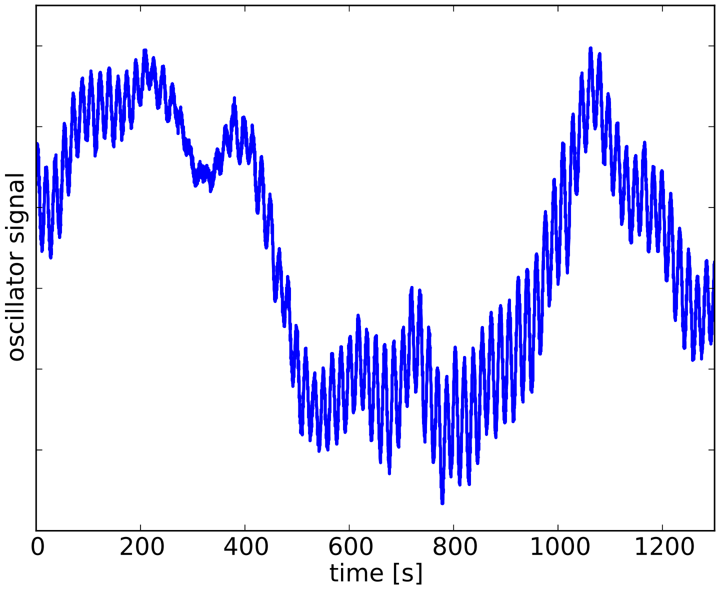

(b) The Leeson effect causes low frequency noise which dominates the measured signal for small amplitudes.

Figure 7.11.: Measurements on Nb_3Sn using the phase shift oscillator for low temperature measurements

REVIEW OF SCIENTIFIC INSTRUMENTS **82**, 094901 (2011)

LC-circuit calorimetry

O. Bossen and A. Schilling
Physik-Institut der Universität Zürich, Winterthurerstrasse 190, 8057 Zürich, Switzerland

(Received 22 June 2011; accepted 11 August 2011; published online 6 September 2011)

We present a new type of calorimeter in which we couple an unknown heat capacity with the aid of Peltier elements to an electrical circuit. The use of an electrical inductance and an amplifier in the circuit allows us to achieve autonomous oscillations, and the measurement of the corresponding resonance frequency makes it possible to accurately measure the heat capacity with an intrinsic statistical uncertainty that decreases as $\sim t_m^{-3/2}$ with measuring time t_m, as opposed to a corresponding uncertainty $\sim t_m^{-1/2}$ in the conventional alternating current method to measure heat capacities. We have built a demonstration experiment to show the feasibility of the new technique, and we have tested it on a gadolinium sample at its transition to the ferromagnetic state. © *2011 American Institute of Physics*. [doi:10.1063/1.3632116]

I. INTRODUCTION

Calorimetry is an old field in experimental physics, and numerous experimental techniques have been developed for the accurate measurement of heat capacities.[1] The frequently used ac technique invented by Corbino[2] and modified by Sullivan and Seidel,[3] for example, measures the heat capacity by monitoring the temperature amplitude of a sample that is subject to an oscillating heating power, or, although less common, by measuring an oscillating heat current produced by a Peltier element.[4] Such ac techniques have numerous advantages over other methods, e.g., heat-pulse, differential thermal analysis,[5] or relaxation techniques.[1] A certain robustness to noise and the possibility to use very small temperature amplitudes stem from the fact that the signal of interest can be separated from the instrumental noise by using a frequency selective filter, such as a lock-in amplifier. To increase the total accuracy even further, the duration of a measurement t_m can be increased at will, and the resulting statistical uncertainty decreases as $t_m^{-1/2}$.

If a calorimeter could be built where the heat capacity is related to the frequency instead of the amplitude of an oscillation, one would retain most of the advantages of the conventional ac techniques, but the statistical uncertainty would decrease much more rapidly,[6] i.e., as $t_m^{-3/2}$. Therefore, the accuracy of such a method would be mainly limited by the stability of the oscillator components, rather than by statistical constraints.

In the following, we describe the realization of an oscillating thermo-electrical circuit using Peltier elements which makes an electrical inductor to effectively act as a "thermal inductor." The heat capacity can be calculated from the measured resonance frequency of the circuit, and its statistical uncertainty drops according to $t_m^{-3/2}$ as expected.

II. OPERATING PRINCIPLE OF THE THERMO-ELECTRICAL OSCILLATOR

It is known that the flow of heat Q_t (with a corresponding heat current $I_t = \dot{Q}_t$) between entities with a certain heat capacity C_t through links with a finite thermal conductivity can be mapped onto the flow of charge Q_e (with the electrical current $I_e = \dot{Q}_e$) in electrical circuits that is composed of capacitors C_e and resistors, respectively, where the temperature T in the thermal case corresponds to the electrostatic potential V in the equivalent electrical circuit. The differential equations describing the time evolution of $Q_t(t)$ or $Q_e(t)$, respectively, are of first order in time t. However, a simple thermal analog of an electrical inductor involving a higher derivative $\ddot{Q}_t = \dot{I}_t$ does not exist, although the inclusion of terms including $\dot{I}_t$ is justified in certain rare cases.[7] Therefore, it is impossible to realize autonomously oscillating thermal circuits by using only standard thermal elements.

In our experiment, we connect an electrical inductor L_e to a Peltier element as shown in Fig. 1. If the heat current I_t through the Peltier element to the thermal bath varies with time, an associated electrical current I_e in the circuit changes according to $\Pi \dot{I}_e = \dot{I}_t$, where Π is the Peltier coefficient of the Peltier element. It induces a voltage drop $L_e \dot{I}_e$ across the inductor that opposes the changes in the heat current I_t through the Peltier element via the Seebeck effect, i.e., a resulting additional temperature difference $\Delta T = L_e \dot{I}_e / \alpha$ (where α denotes the Seebeck coefficient) across the Peltier element is imposed that counteracts the variation in the flow of heat, $\dot{I}_t$. We can, therefore, define an effective thermal inductance,

$$L_t := \frac{\Delta T}{\dot{I}_t} = \frac{L_e}{\alpha \Pi}. \tag{1}$$

However, as a consequence of the significant losses produced by the non-zero thermal conductivity and electrical resistance of the Peltier element, the idealized element shown in Fig. 1 allows in general only for an overdamped variation of the heat current. This obstacle can be avoided by including an amplifier with a suitable gain in the electrical circuit, and autonomous oscillations can eventually be achieved in this way. In the ideal case of a stationary oscillation with constant amplitude where all losses are exactly compensated by the amplifying element, the electrical circuit behaves like a simple LC-circuit with thermal inductance L_t and the heat capacity C_t, or with an electrical inductance L_e and an equivalent elec-

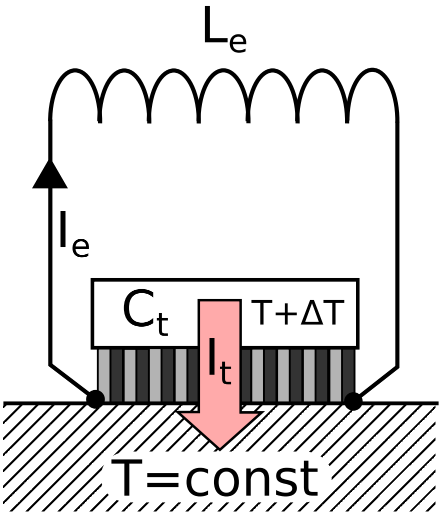

FIG. 1. (Color online) An electrical inductor L_e is connected to a Peltier element that separates the heat capacity C_t from a thermal bath T. Changes in the electrical current I_e induce a temperature difference $\Delta T = L_e \dot{I}_e/\alpha$ (where α denotes the Seebeck coefficient) across the Peltier element that counteracts the variation in the flow of heat $\dot{I}_t$.

trical capacitance,

$$C_e = \frac{Q_e}{V} = \frac{\int I_e \, dt}{\alpha \Delta T} = \frac{C_t \int I_e \, dt}{\alpha \int \Pi I_e \, dt} = \frac{C_t}{\alpha \Pi} \tag{2}$$

and with resonance frequency $\omega^2 = 1/L_t C_t = 1/L_e C_e$. Therefore, the heat capacity can be derived from ω according to

$$C_t = \frac{\alpha \Pi}{L_e \omega^2}, \tag{3}$$

notably without any need to quantify the thermal and electrical losses in the Peltier element. To the best of our knowledge, the correspondences between an L_e and a thermal analog L_t, or a C_t and a C_e as expressed in Eqs. (1) and (2), respectively, are novel and have also never been exploited in any calorimetric technique.

III. EXPERIMENTAL SETUP

We have chosen the circuit shown in Fig. 2 containing two Peltier elements (MPC-D701, Micropelt Inc.) based on Bi_2Te_3, with lateral dimensions of ≈3.5 mm and a thickness of ≈1 mm. While the left element acts, together with the sample to be measured, as the equivalent electrical capacitance as described above, the right element is used to compensate for thermal and electrical losses and to maintain a constant amplitude of the temperature oscillation. For this purpose, the voltage across the right element is amplified and then fed onto the electrical contacts of the left element. To achieve a stable oscillation of the desired amplitude, the gain of the amplifier can be controlled using a voltage-controlled gain amplifier (AD630, Analog Devices). An additional clamp with Schottky diodes (BAT43) and two potentiometers forms a nonlinear resistor that reduces the gain at large oscillation amplitudes and, therefore, forces the circuit to self-stabilize.

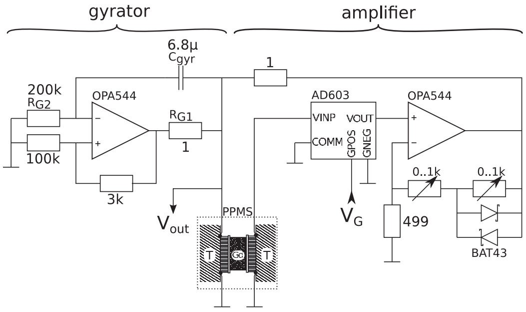

FIG. 2. Circuit diagram showing the Peltier element system, the Gyrator to mimic a large electrical inductance, and the amplifier to compensate for thermal and electrical losses (see text). The voltage V_G controls the gain of the amplifier. The two Peltier elements have the same polarity, and the sample is attached to their "top side." The measured signal is tapped at V_{out}.

For a design heat capacity $C_t \approx 20\,\mathrm{mJ/K}$ to be measured near room temperature (which corresponds to 2.87×10^{-4} mol of a Dulong-Petit solid), and using $\alpha \approx 29\,\mathrm{mV/K}$ and $\Pi \approx \alpha T \approx 8.4\,\mathrm{W/A}$ for the used Peltier elements, the equivalent electrical capacitance becomes $C_e \approx 82\,\mathrm{mF}$. Depending on the heat capacities and the thermal conductivities involved in the thermal part of the system, the frequency of the temperature oscillation must be small enough to allow for a quasi-stationary thermal equilibrium. If we choose $f = \omega/2\pi \approx 0.18\,\mathrm{Hz}$, we need an inductance $L_e \approx 10\,\mathrm{H}$ which would require impractically large passive elements. Therefore, we replaced the inductance by a gyrator, the circuit diagram of which is also shown in Fig. 2. The effective induction of the gyrator is given by Ref. 8 $L_e = (R_P + R_{G1}) R_{G2} C_{gyr}$, where the internal resistance $R_P \approx 6.5\,\Omega$ of the Peltier element has to be included here. With $R_{G1} = 1\,\Omega$, $R_{G2} = 200\,\mathrm{k}\Omega$, and $C_{gyr} = 6.8\,\mu\mathrm{F}$, we indeed obtain $L_e \approx 10\,\mathrm{H}$.

IV. TEST MEASUREMENTS

A test sample (45.2 mg or 2.87×10^{-4} mol of gadolinium with 99.99% purity that had been previously annealed at $T = 1123\,\mathrm{K}$ in vacuum to reduce lattice strains)[9] was sandwiched between the two Peltier elements and placed into a commercial physical property measurement system (PPMS, Quantum Design) for control of the base temperature. The gain of the amplifier was chosen in a way to achieve temperature oscillations with an amplitude of the order of 0.2 K. For each data point, the oscillating voltage was read out during 1200 s with a 10 Hz-triggered Keithley 2001 multimeter in equal time intervals of 0.1 s (see Fig. 3), and the resulting data were then least-squares fitted to obtain the oscillation frequency (see Fig. 4(a)). To compensate for the heat capacity of the empty system (≈15% of the total heat capacity), corresponding measurements have been done without the sample installed. The resulting values of the heat capacity are shown

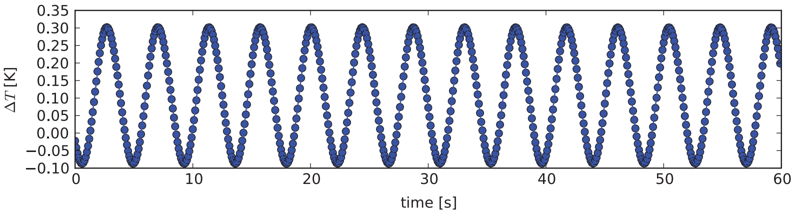

FIG. 3. (Color online) Thermal oscillations of the LC-circuit. The solid line is a least-squares fit to a sinusoidal variation of ΔT in time around an offset value that is caused by lost heat dissipated in the Peltier elements.

in Fig. 4(b), together with the heat-capacity data obtained on the same sample using the commercial heat-capacity option of the PPMS system and with temperature steps of ≈ 0.5 K. While the heat-capacity data using our thermal LC-method are neither smoothed nor further averaged, the PPMS data were averaged over six individual measurements. The data-acquisition time for each of the LC-method data points was 1200 s, while collecting an averaged PPMS data point took about one hour of time, and the temperature amplitudes for both techniques were comparable (0.3 K–0.5 K). The transition of the Gd sample to the ferromagnetic state takes place at the Curie temperature $T_C \approx 290$ K, and the absolute values for the heat capacity agree well with the PPMS data (see Fig. 4(b)).

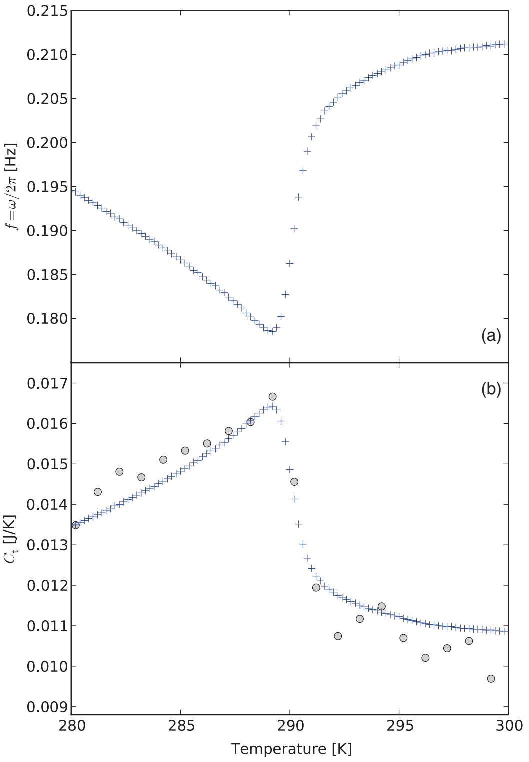

FIG. 4. (Color online) (a) Measured frequency of the oscillator and (b) heat capacity of a Gd sample, as functions of temperature. Crosses represent the data that we obtained by the present thermal LC-method, while circles denote the values from the measurements on the same sample using a commercial heat-capacity system (see text).

V. ACCURACY CONSIDERATIONS

The accuracy of any heat-capacity measurement is limited by systematic and statistical uncertainties. Sources of systematic errors (such as finite instrumental resolution, limited accuracy by a large background signal, and errors in the temperature calibration) are common to all techniques for measuring the heat capacity, and we shall not further discuss these shortcomings here. The main advantage of the present thermal LC-circuit technique is that it significantly reduces the statistical uncertainty with increasing measuring time.

The statistics behind the problem of estimating the amplitude A, the frequency ω, and the phase φ of an oscillation $A\sin(\omega t + \varphi)$ out of a set of N samples of finite length T has been analyzed in detail in Ref. 6. Assuming a white noise with variance σ^2, the resulting relative standard deviation σ_A/A in the amplitude A from a measurement of N oscillation cycles with length $T = 2\pi/\omega$ is

$$\frac{\sigma_A}{A} \geq \frac{\sigma}{A\sqrt{N}}. \tag{4}$$

In a conventional ac technique to measure heat capacities, the relative standard deviation in the heat capacity C_t from the mean value is proportional to the respective standard deviation in the measured amplitude A of a temperature oscillation,[2] and therefore, the statistical uncertainty in C_t decreases with $t_m^{-1/2}$ where $t_m = NT$ is the total time to take such a measurement (in all other conventional methods, the statistical uncertainty also decreases as $N^{-1/2}$, where N is the number of measurements to calculate the average of a data point).

The corresponding relative standard deviation σ_ω/ω in the frequency ω, however, varies with N according to

$$\frac{\sigma_\omega}{\omega} \geq \frac{\sqrt{3}\sigma}{\pi A\sqrt{N(N^2-1)}}, \tag{5}$$

i.e., it decreases with $N^{-3/2}$ (or $t_m^{-3/2}$) for large N. As the heat capacity in our technique is proportional to ω^{-2} (see Eq. (3)), the relative standard deviation $\sigma_{C_t}/C_t \approx 2\sigma_\omega/\omega$ also decreases with N in the same fashion. In Fig. 5, we show the amplitudes and the frequencies for a selected data point,

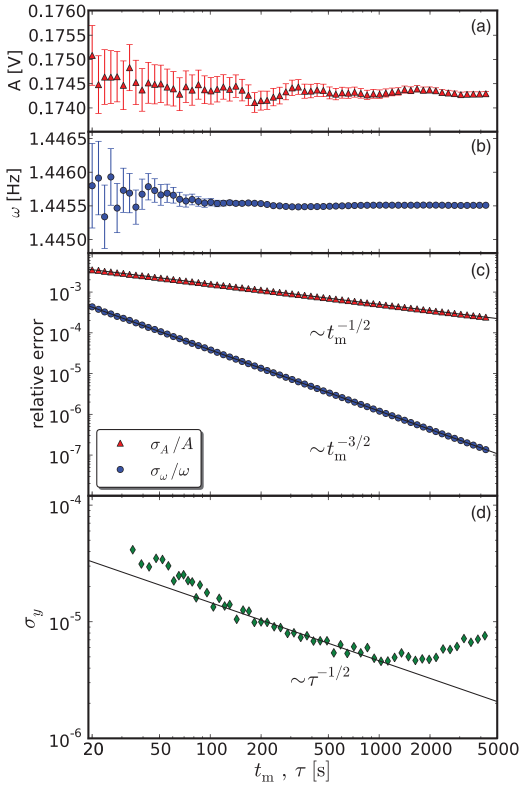

FIG. 5. (Color online) (a) Amplitudes and (b) frequencies for a selected data point together with the respective standard deviations from the Levenberg-Marquardt fit, as functions of measurement time t_{m}. (c) The respective relative standard deviations on a log-log scale to illustrate the power-law behavior are discussed in the text. Solid lines are fits according to $t^{-1/2}$ for σ_A/A and to $t^{-3/2}$ for the σ_ω/ω data, respectively. (d) The overlapping Allan deviation σ_y, plotted against the observation time τ. The solid line illustrates the approximate $\tau^{-1/2}$ dependence of σ_y (see text).

together with the respective relative standard deviations, as functions of the measurement time t_{m} which is proportional to the number of oscillation cycles N. The standard deviations σ_A and σ_ω have been taken from a standard Levenberg-Marquardt routine used for least-squares fitting the experimental data. The σ_A/A data decrease relatively slowly with $N^{-1/2}$, while the σ_ω/ω data (and along with them $\sigma_{C_{\mathrm{t}}}/C_{\mathrm{t}}$) drop much faster with $N^{-3/2}$ as expected. Therefore, very high accuracies for C_{t} can, in principle, be achieved in a comparably very short measuring time. For example, to reduce the statistical uncertainty in C_{t} by a factor of 10, conventional methods require 100 times longer duration of a measurement, while the thermal LC method needs only ≈5 times longer data acquisition time. As both σ_A/A and σ_ω/ω are proportional to the same quantity σ/A, there is no hidden drawback in the Eq. (5) that would put this tremendous statistical advantage into perspective.

However, in order to tap the full potential of this technique, it is essential that the oscillation frequency ω is sufficiently stable during the time of the measurement so that the potentially minuscule statistical uncertainty is not impaired by extrinsic fluctuations, e.g., by an insufficient stabilization of the temperature of the sample or by an unwanted variability in the electronic circuit. While a Levenberg-Marquardt fit always finds some least-squares minimum, with a σ_ω that decreases for increasing t_{m}, the actual oscillator frequency can be unstable in such a way that repeated measurements under identical experimental conditions lead to different results for the fitted parameters. The quantity σ_ω, therefore, cannot be readily interpreted as the true measurement error of ω. A standard measure for the stability of an oscillator is provided by the Allan deviation σ_y.[10] Assuming white noise in the oscillator frequency ω, for example, σ_y is expected to drop as $\tau^{-1/2}$, where τ denotes the time over which the frequency is observed. At large observation times, σ_y can saturate or even increase again as soon as other sources of noise (Flicker noise, random-walk noise) become dominant.[11] In Fig. 5(d), we have plotted the overlapping Allan deviation as a function of observation time τ on a log-log scale. While σ_y initially drops approximately with $\tau^{-1/2}$, it saturates in our experiment around $\sigma_y \approx 4 \times 10^{-6}$ for $\tau \approx 1000$ s and increases for larger values of τ. In this sense, we interpret the minimum in σ_y as an estimate for the achievable uncertainty in ω for a given set of experimental data, while the σ_ω/ω values from Eq. (5) and shown in Fig. 5(c) represent the statistical uncertainty assuming a perfectly stable frequency with white noise only in the temperature amplitude. In our demonstration experiment, no special care has been taken to minimize extrinsic sources for variations in ω. Such sources of error are the decisive factors that are limiting the maximum achievable accuracy in the present thermal LC technique, but they are to a large extent controllable, while the intrinsic statistical uncertainty should play a significantly less important role than in conventional techniques to measure heat capacities.

VI. CONCLUSIONS

We have described a method where the heat capacity is coupled to an electrical circuit with the aid of the Peltier elements, which makes an electrical inductor to effectively act as a "thermal inductor." The use of an amplifier in the circuit allows us to achieve autonomous oscillations, and the measurement of the corresponding resonance frequency makes it possible to calculate the heat capacity. While the statistical uncertainty in conventional techniques to measure heat capacities scales according to $t_{\mathrm{m}}^{-1/2}$ with measuring time t_{m}, the respective uncertainty in the present thermal LC technique decreases significantly faster, i.e., with $t_{\mathrm{m}}^{-3/2}$, and is ultimately limited by the stability of the thermal and electronic components used in the experiment.

ACKNOWLEDGMENTS

This work was supported by the Schweizerische Nationalfonds zur Förderung der Wissenschaftlichen Forschung (Grant. No. 20-131899).

[1] E. Gmelin, Thermochim. Acta **29**, 1 (1979); G. R. Stewart, Rev. Sci. Instrum. **54**, 1 (1983); Y. Kraftmakher, Phys. Rep. **356**, 1 (2002).

[2] O. M. Corbino, Phys. Z. **XI**, 413 (1910); **XIII**, 375 (1912).

[3] P. F. Sullivan and G. Seidel, Phys. Rev. **173**, 679 (1968).

[4] D. Jung, I. Moon, and Y. Jeong, Thermochim. Acta **391**, 7 (2002); R. Lortz, S. Abe, Y. Wang, F. Bouquet, U. Tutsch, and A. Junod, Rev. Sci. Instrum. **76**, 103902 (2005).

[5] A. Schilling and M. Reibelt, Rev. Sci. Instrum. **78**, 033904 (2007).

[6] D. C. Rife and R. R. Boorstyn, IEEE Trans. Inf. Theory **IT-20**, 591 (1974).

[7] R. C. L. Bosworth, Nature (London) **158**, 309 (1946); T. F. McNelly, S. J. Rogers, D. J. C. R. J. Rollefson, W. M. Goubau, G. E. Schmidt, J. A. Krumhansl, and R. O. Pohl, Phys. Rev. Lett. **24**, 100 (1970); B. M. Weedy, IEEE Electr. Power Syst. Res. **15**, 197 (1988); D. D. Joseph and L. Preziosi, Rev. Mod. Phys. **61**, 41 (1989).

[8] D. F. Berndt and S. C. Dutta Roy, IEEE J. Solid-State Circuits **SC-4**, 161 (1969).

[9] D. S. Simons and M. B. Salamon, Phys. Rev. B **10**, 4680 (1974).

[10] P. Allan, Proc. IEEE **54**, 221 (1966).

[11] W. Riley, *Handbook of Frequency Stability Analysis*, NIST Special Publication No. 1065 (NIST, Boulder, CO, 2008).

8. Conclusions

We have discussed the vortex-lattice melting in conventional low-T_c superconductors and derived numeric results for the expected melting entropies and magnetization discontinuities. As expected, the discontinuities in Δs and ΔM are largest in compounds with a high critical temperature T_{c0} and a large Gi. The maximum possible values for the discontinuities Δs vary by more than two orders of magnitude between the different substances, and they are commonly attained around approximately $B \approx B_{c2}(0)/2$. The smallest Δs and ΔM values can be expected in low-T_c, low-Gi materials such as Nb and $\mathrm{CaC_6}$. Moreover, the latter materials show also low κ values on the order of unity, and they may therefore suffer from an additional reduction of Δs and ΔM.

In order to test our predictions for the melting signatures in the heat capacity and the magnetization we have performed measurements on a $\mathrm{Nb_3Sn}$ single crystal for which evidence of a possible vortex lattice melting transition was reported by Lortz *et al.* [26]. We have shown that the AC magnetic susceptibility data of the $\mathrm{Nb_3Sn}$ sample displaying a peak effect near T_c can be well explained using a flux-creep model with a varying creep exponent. While $n \approx 5$ fits our data outside the peak-effect region reasonably well, a larger exponent $n \approx 51$, i.e. a scenario closer to Bean's critical-state model applies within the narrow peak-effect region near T_c.

Depending on the magnitude of the critical-current density in the peak-effect region, the sample geometry and the probing AC magnetic field, single or double peaks in $\chi''(T)$ may occur that are nevertheless manifestations of the same underlying physical phenomenon.

We have also performed measurements of the heat capacity on $\mathrm{Nb_3Sn}$ which show no detectable sign of vortex lattice melting in magnetic fields between 0 T and 9 T for plain AC calorimetric measurements. In order to minimize non-equilibrium effects we performed heat capacity measurements using a vortex lattice "shaking" technique with various shaking amplitudes and frequencies. We find that the strong variation of the magnetic self heating with temperature, which is induced by this vortex lattice “shaking” method in conjunction with the magnetic susceptibility anomalies in the peak effect region, severely affects the heat capacity measurements and can produce melting-like artifacts. These artifacts essentially disappear, as soon as the phase of the temperature signal is correctly taken into account in the analysis. We conclude that the strong variation of the magnetic-heating power with temperature in the peak-effect region must be taken into account in thermal experiments using a simultaneous “vortex-shaking” field, in order to prevent the occurence of artifacts in the resulting heat-capacity data.

In order to reach the high sensitivity that is necessary to detect the small value of Δs, we have described a calorimetry technique in which a heat capacity is coupled to an electrical circuit with the aid of Peltier elements, which makes an electrical inductor to effectively act as a “thermal inductor“. The use of an amplifier in the circuit allows us to achieve autonomous oscillations, and the measurement of the corresponding resonance frequency makes it possible to calculate the heat capacity. While the statistical uncertainty in conventional techniques to measure heat capacities scales according to $t_{\mathrm{m}}^{-1/2}$ with measuring time t_{m}, the respective uncertainty in the presented thermal ”LC technique“ decreases significantly faster, i.e., with $t_{\mathrm{m}}^{-3/2}$, and is ultimately limited by the stability of the thermal and electronic components used in the experiment. While we have demonstrated the principal feasibility of using a thermal oscillator technique at low temperatures more work will be necessary to bring this technique to the same level of accuracy as the established AC calorimetry technique by Sullivan and Seidel.

Bibliography

[1] H. K. Onnes, “The liquefication of helium,” *Proc. K. Akad. Amsterdam*, vol. 11, p. 168, 1908.

[2] H. K. Onnes, “Further experiments with liquid helium. C. On the change of electric resistance of pure metals at very low temperatures, etc. IV. The resistance of pure mercury at helium temperatures.,” *Commun. Phys. Lab. Univ. Leiden*, vol. 120b, 1911.

[3] H. K. Onnes, “Further experiments with liquid helium. D. On the change of electric resistance of pure metals at very low temperatures, etc. V. The disappearance of the resistance of mercury.,” *Comm. Phys. Lab. Univ. Leiden*, vol. 122b, 1911.

[4] H. K. Onnes, “Further experiments with liquid helium. G. On the electrical resistance of pure metals, etc. VI. On the sudden change in the rate at which the resistance of mercury disappears.,” *Comm. Phys. Lab. Univ. Leiden*, vol. 124c, 1911.

[5] W. Meissner and R. Ochsenfeld, “Ein neuer Effekt bei Eintritt der Supraleitfähigkeit,” *Naturwissenschaften*, vol. 21, no. 44, pp. 787—788, 1933.

[6] F. London and H. London, “The Electromagnetic Equations of the Supraconductor,” *Proc. R. Soc. Lond.*, vol. A149, pp. 71–88, 1935.

[7] V. L. Ginzburg and L. Landau, “On the theory of superconductivity,” *Zh. Eksp. Theor. Fiz.*, vol. 20, p. 1064, 1950.

[8] A. A. Abrikosov, “On the Magnetic Properties of Superconductors of the Second Group,” *J. Exp. Theor. Phys.*, vol. 5, no. 6, p. 1174, 1957.

[9] C. A. Reynolds, B. Serin, W. H. Wright, and L. B. Nesbitt, “Superconductivity of isotopes of mercury,” *Phys. Rev.*, vol. 78, p. 487, 1950.

[10] E. Maxwell, “Isotope effect in the superconductivity of mercury,” *Phys. Rev.*, vol. 78, p. 477, 1950.

[11] H. Fröhlich, “Theory of the superconducting state I. The ground state at the absolute zero of temperature,” *Phys. Rev.*, vol. 79, p. 845, 1950.

[12] L. N. Cooper, “Bound Electron Pairs in a Degenerate Fermi Gas,” *Phys. Rev.*, vol. 104, pp. 1189–1190, Nov 1956.

[13] J. Bardeen, L. N. Cooper, and J. R. Schrieffer, “Microscopic Theory of Superconductivity,” *Phys. Rev.*, vol. 106, pp. 162–164, Apr 1957.

[14] J. Bardeen, L. N. Cooper, and J. R. Schrieffer, “Theory of Superconductivity,” *Phys. Rev.*, vol. 108, pp. 1175–1204, Dec 1957.

[15] L. Gor’kov, “Microscopic derivation of the ginzburg-landau equations in the theory of superconductivity,” *Sov. Phys. JETP*, vol. 9, pp. 1364–1367, 1959.

[16] L. Gor’kov, “Mikroskopicheskii vyvod uravnenii Ginzburga-Landau v teorii sverkhprovodimosti,” *Zh. Eksp. Theor. Fiz.*, vol. 36, no. 6, pp. 1918–1923, 1959.

[17] J. Bednorz and K. Müller, “Possible highT_c superconductivity in the Ba–La–Cu–O system,” *Z. Phys. B*, vol. 64, pp. 189–193, 1986.

[18] J. Nagamatsu, N. Nakagawa, T. Muranaka, Y. Zenitani, and J. Akimitsu, “Superconductivity at 39 K in magnesium diboride,” *Nature*, vol. 410, pp. 63–64, 2001.

[19] Y. Kamihara, H. Hiramatsu, M. Hirano, R. Kawamura, H. Yanagi, T. Kamiya, and H. Hosono, “Iron-Based Layered Superconductor: LaOFeP,” *Journal of the American Chemical Society*, vol. 128, no. 31, pp. 10012–10013, 2006. PMID: 16881620.

[20] P. W. Anderson, “Theory of Flux Creep in Hard Superconductors,” *Phys. Rev. Lett.*, vol. 9, pp. 309–311, Oct 1962.

[21] R. Cubitt, E. M. Forgan, G. Yang, S. L. Lee, D. M. Paul, H. A. Mook, M. Yethiraj, P. H. Kes, T. W. Li, A. A. Menovsky, Z. Tarnawski, and

K. Mortensen, “Direct observation of magnetic flux lattice melting and decomposition in the high-Tc superconductor $Bi_{2.15}Sr_{1.95}CaCu_2O_{8+x}$,” *Nature*, vol. 365, pp. 407–411, 1993.

[22] A. Schilling, R. A. Fisher, N. E. Phillips, U. Welp, D. Dasgupta, W. K. Kwok, and G. W. Crabtree, “Calorimetric measurement of the latent heat of vortex-lattice melting in untwinned $YBa_2Cu_3O_{7-\delta}$,” *Nature*, vol. 382, pp. 791–793, 1996.

[23] M. Roulin, A. Junod, and E. Walker, “Flux Line Lattice Melting Transition in $YBa_2Cu_3O_{6.94}$ Observed in Specific Heat Experiments,” *Science*, vol. 273, pp. 1210–1212, 1996.

[24] T. G. Berlincourt, R. R. Hake, and D. H. Leslie, “Superconductivity at High Magnetic Fields and Current Densities in Some Nb-Zr Alloys,” *Phys. Rev. Lett.*, vol. 6, pp. 671–674, Jun 1961.

[25] A. B. Pippard, “A possible mechanism for the peak effect in type II superconductors,” *Philos. Mag.*, vol. 19, no. 158, pp. 217–220, 1969.

[26] R. Lortz, F. Lin, N. Musolino, Y. Wang, A. Junod, B. Rosenstein, and N. Toyota, “Thermal fluctuations and vortex melting in the Nb_3Sn superconductor from high resolution specific heat measurements,” *Phys. Rev. B*, vol. 74, p. 104502, Sep 2006.

[27] M. Tinkham, *Introduction to Superconductivity.* Dover books on physics and chemistry, Dover, 1996.

[28] G. Blatter, M. V. Feigel’man, V. B. Geshkenbein, A. I. Larkin, and V. M. Vinokur, “Vortices in high-temperature superconductors,” *Rev. Mod. Phys.*, vol. 66, pp. 1125–1388, 1994.

[29] P. J. Curran, V. V. Khotkevych, S. J. Bending, A. S. Gibbs, S. L. Lee, and A. P. Mackenzie, “Vortex imaging and vortex lattice transitions in superconducting Sr_2RuO_4 single crystals,” *Phys. Rev. B*, vol. 84, p. 104507, Sep 2011.

[30] H. F. Hess, R. B. Robinson, R. C. Dynes, J. M. Valles, and J. V. Waszczak, “Scanning-Tunneling-Microscope Observation of the Abrikosov Flux Lattice and the Density of States near and inside a Fluxoid,” *Phys. Rev. Lett.*, vol. 62, pp. 214–216, Jan 1989.

[31] E. H. Brandt and G. P. Mikitik, “Why an ac Magnetic Field Shifts the Irreversibility Line in Type-II Superconductors,” *Phys. Rev. Lett.*, vol. 89, p. 027002, Jun 2002.

[32] M. Willemin, C. Rossel, J. Hofer, H. Keller, A. Erb, and E. Walker, “Strong shift of the irreversibility line in high-T_c superconductors upon vortex shaking with an oscillating magnetic field,” *Phys. Rev. B*, vol. 58, pp. R5940–R5943, Sep 1998.

[33] E. H. Brandt and G. P. Mikitik, “Vortex shaking in superconducting platelets in an inclined magnetic field,” *Supercond. Sci. Technol.*, vol. 20, no. 9, p. S111, 2007.

[34] D. R. Nelson, “Vortex Entanglement in High-T_c Superconductors,” *Phys. Rev. Lett.*, vol. 60, no. 19, pp. 1973–1976, 1988.

[35] A. Houghton, R. A. Pelcovits, and A. Sudbø, “Flux lattice melting in high-Tc superconductors,” *Phys. Rev.B*, vol. 40, no. 10, pp. 6763 – 6770, 1989.

[36] P. L. Gammel, L. F. Schneemeyer, J. V.Wasczak, and D. J. Bishop, “Evidence from Mechanical Measurements for Flux-Lattice Melting in Single-Crystal $\mathrm{YBa_2Cu_3O_7}$ and $\mathrm{Bi_2 \cdot 2\,Sr_2Ca_0 \cdot 8\,Cu_2O_8}$,” *Phys. Rev. Lett.*, vol. 61, no. 14, pp. 1666–1669, 1988.

[37] D. E. Farrell, J. P. Rice, and D. M. Ginsberg, “Experimental Evidence for Flux-Lattice Melting,” *Phys. Rev. Lett.*, vol. 67, no. 9, pp. 1165–1168, 1991.

[38] H. Safar, P. L. Gammel, D. A. Huse, D. J. Bishop, J. P. Rice, and D. M. Ginsberg, “Experimental evidence for a first-order vortex-lattice-melting transition in untwinned, single crystal $\mathrm{YBa_2Cu_3O_7}$,” *Phys. Rev. Lett.*, vol. 69, pp. 824–827, Aug 1992.

[39] S. L. Lee, P. Zimmermann, H. Keller, M. Warden, I. M. Savić, R. Schauwecker, D. Zech, R. Cubitt, E. M. Forgan, P. H. Kes, T. W. Li, A. A. Menovsky, and Z. Tarnawski, “Evidence for flux-lattice melting and a dimensional crossover in single-crystal $\mathrm{Bi_{2.15}Sr_{1.85}CaCu_2O_{8+\delta}}$ from muon spin rotation studies,” *Phys. Rev. Lett.*, vol. 71, pp. 3862–3865, Dec 1993.

[40] D. S. Fisher, M. P. A. Fisher, and D. A. Huse, “Thermal fluctuation, quenched disorder, phasee transitions, and tansport in type-II superconductors,” *Phys. Rev. B.*, vol. 43, no. 1, pp. 130–159, 1991.

[41] G. Blatter and B. Ivlev, "Quantum melting of the vortex lattice in high-Tc superconductors," *Phys. Rev. Lett.*, vol. 70, no. 17, pp. 2621–2624, 1993.

[42] E. Zeldov, D. Majer, M. Konczykowski, V. B. Geshkenbein, V. M. Vinokur, and H. Shtrikman, "Thermodynamic observation of first-order vortex-lattice melting transition in $Bi_2Sr_2CaCu_2O_8$," *Nature*, vol. 375, pp. 373–376, 1995.

[43] H. Pastoriza, M. F. Goffman, A. Arribére, and F. de la Cruz, "First Order Phase Transition at the Irreversibility Line of $Bi_2Sr_2CaCu_2O_{8+\delta}$," *Phys. Rev. Lett.*, vol. 72, no. 18, pp. 2951–2954, 1994.

[44] U. Welp, J. A. Fendrich, W. Kwok, G. Crabtree, and B. Veal, "Thermodynamic Evidence for a Flux Line Lattice Transition in $YBa_2Cu_3O_{7-\delta}$," *Phys. Rev. Lett.*, vol. 76, no. 25, pp. 4809–4812, 1996.

[45] A. Schilling, M. Willemin, C. Rossel, H. Keller, R. A. Fisher, N. E. Phillips, U. Welp, W. K. Kwok, R. J. Olsson, and G. W. Crabtree, "Anisotropy of magnetization discontinuity at vortex-lattice melting in untwinned $YBa_2Cu_3O_{7-\delta}$," *Phys. Rev. B*, vol. 61, pp. 3592–3603, Feb 2000.

[46] M. P. A. Fisher, "Vortex-glass superconductivity: A possible new phase in bulk high-T_c oxides," *Phys. Rev. Lett.*, vol. 62, pp. 1415–1418, Mar 1989.

[47] A. Schilling, R. A. Fisher, N. E. Phillips, U. Welp, W. K. Kwok, and G. W. Crabtree, "Anisotropic Latent Heat of Vortex-Lattice Melting in Untwinned $YBa_2Cu_3O_{7-\delta}$," *Phys. Rev. Lett.*, vol. 78, pp. 4833–4836, Jun 1997.

[48] A. Schilling, R. A. Fisher, N. E. Phillips, U. Welp, W. K. Kwok, and G. W. Crabtree, "Angular dependence of the latent heat of vortex-lattice melting in untwinned $YBa_2Cu_3O_{7-\delta}$," *Phys. Rev. B*, vol. 58, pp. 11157–11160, Nov 1998.

[49] A. Schilling, U. Welp, W. K. Kwok, and G. W. Crabtree, "Vortex-lattice melting in untwinned $YBa_2Cu_3O_{7-\delta}$ for $H \perp c$," *Phys. Rev. B*, vol. 65, p. 054505, Jan 2002.

[50] F. Bouquet, C. Marcenat, E. Steep, R. Calemczuk, W. K. Kwok, U. Welp, G. W. Crabtree, R. A. Fisher, N. E. Phillips, and A. Schilling, "An unusual phase transition to a second liquid vortex phase in the superconductor $YBa_2Cu_3O_7$," *Nature*, vol. 411, pp. 448–451, 2001.

[51] M. Roulin, A. Junod, A. Erb, and E. Walker, “Calorimetric Transitions on the Melting Line of the Vortex System as a Function of Oxygen Deficiency in High-Purity $YBa_2Cu_3O_x$,” *Phys. Rev. Lett.*, vol. 80, pp. 1722–1725, Feb 1998.

[52] B. Revaz, A. Junod, and A. Erb, “Specific heat peaks observed up to 16 T on the melting line of vortex matter in $DyBa_2Cu_3O_7$,” *Phys. Rev. B*, vol. 58, pp. 11153–11156, Nov 1998.

[53] H. Iwasaki, T. Chigira, T. Naito, S. Moriyama, Y. Iwasa, T. Nishizaki, and N. Kobayashi, “Observation of the vortex lattice phase transition in the specific heat in $La_{1.86}Sr_{0.14}CuO_4$ single crystal,” *Physica C*, vol. 366, pp. 129–134, 2002.

[54] M. J. W. Dodgson, V. B. Geshkenbein, H. Nordborg, and G. Blatter, “Characteristics of First-Order Vortex Lattice Melting: Jumps in Entropy and Magnetization,” *Phys. Rev. Lett.*, vol. 80, no. 4, pp. 837 – 840, 1998.

[55] M. J. W. Dodgson, V. B. Geshkenbein, H. Nordborg, and G. Blatter, “Thermodynamics of the first-order vortex lattice melting transition in $YBa_2Cu_3O_{7-\delta}$,” *Phys. Rev. B*, vol. 57, pp. 14498–14506, Jun 1998.

[56] C. J. Bowell, R. J. Lycett, M. Laver, C. D. Dewhurst, R. Cubitt, and E. M. Forgan, “Absence of vortex lattice melting in a high-purity Nb superconductor,” *Phys. Rev. B*, vol. 82, p. 144508, 2010.

[57] A. R. Ruffa, “Thermal potential, mechanical instability, and melting entropy,” *Phys. Rev. B*, vol. 25, no. 9, pp. 5895 – 5900, 1982.

[58] J. Kierfeld, “Lindeman criterion and vortex Lattice phase transitions in type-II superconductors,” *Phys. Rev. B*, vol. 69, p. 024501, 2004.

[59] O. Bossen and A. Schilling, “Estimates for the thermodynamic signatures of vortex-lattice melting in conventional superconductors,” *Physica C*, vol. 483, no. 0, pp. 201 – 206, 2012.

[60] F. A. Lindemann, “The calculation of molecular vibration frequencies,” *Z. Phys.*, vol. 11, p. 609, 1910.

[61] G. P. Mikitik and E. H. Brandt, “Peak effect, vortex-lattice melting line, and order-disorder transition in conventional and high-Tc superconductors,” *Phys. Rev. B*, vol. 64, p. 184514, 2001.

[62] E. H. Brandt, “Properties of the flux line lattice in type-II superconductors,” *Phys. Rev. B*, vol. 34, no. 9, pp. 6514–6517, 1986.

[63] S. Ryu, S. Doniach, G. Deutscher, and A. Kapitulnik, “Monte Carlo simulation of flux lattice melting in a model high-T_c superconductor,” *Phys. Rev. Lett.*, vol. 68, pp. 710–713, Feb 1992.

[64] P. A. Lee and S. R. Shenoy, “Effective Dimensionality Change of Fluctuations in Superconductors in a Magnetic Field,” *Phys. Rev. Lett.*, vol. 28, no. 16, pp. 1025–1028, 1972.

[65] U. Welp, C. Chaparro, A. E. Koshelev, W. K. Kwok, A. Rydh, N. D. Zhigadlo, J. Karpinski, and S. Weyeneth, “Anisotropic phase diagram and superconducting fluctuations of single-crystalline $\mathrm{SmFeAsO_{0.85}F_{0.15}}$,” *Phys. Rev. B*, vol. 83, p. 100513, Mar 2011.

[66] H. Nakagawa, N. Miura, and Y. Enomoto, “The upper critical field and the normal-state resistivity of $\mathrm{YBa_2Cu_3O_{7-\delta}}$ thin films in megagauss fields,” *J. Phys.-Condens. Mat.*, vol. 10, no. 49, p. 11571, 1998.

[67] U. Welp, W. K. Kwok, G. W. Crabtree, K. G. Vandervoort, and J. Z. Liu, “Magnetic measurements of the upper critical field of $\mathrm{YBa_2Cu_3O_{7-\delta}}$ single crystals,” *Phys. Rev. Lett.*, vol. 62, pp. 1908–1911, Apr 1989.

[68] A. Sokolov, Y. Kufaev, and E. Sonin, “Penetration depth and Ginzburg number in $\mathrm{Rb_3C_{60}}$,” *Physica C*, vol. 212, no. 1–2, pp. 19 – 22, 1993.

[69] C. Bueza and T. Yamashita, “Review of the superconducting properties of $\mathrm{MgB_2}$,” *Supercond. Sci. Technol.*, vol. 14, pp. R115–R146, 2001.

[70] M. Angst, R. Puzniak, A. Wisniewski, J. Jun, S. M. Kazakov, J. Karpinski, and J. R. H. Keller, “Temperature and field dependence of the Anisotropy of $\mathrm{MgB_2}$,” *Phys. Rev. Lett.*, vol. 88, no. 16, p. 167004, 2002.

[71] A. S. Sefat, R. Jin, M. A. McGuire, B. C. Sales, D. J. Singh, and D. Mandrus, “Superconductivity at 22 K in Co-Doped $\mathrm{BaFe_2As_2}$ Crystals,” *Phys. Rev. Lett.*, vol. 101, p. 117004, Sep 2008.

[72] B. A. Baumert, "Potassium Barium Bismuth Oxide: A Review," *J. Supercond.*, vol. 8, no. 1, pp. 175–181, 1995.

[73] G. Otto, E. Saur, and H. Wizgall, "Critical data of some A15 type superconductors in transverse fields up to 230 kOe," *J. Low Temp. Phys.*, vol. 1, no. 1, pp. 19–28, 1969.

[74] M. N. Khlopkin, "The specific heat in Nb_3Sn in magnetic field up to 19 T," *Sov. Phys. JETP*, vol. 63, p. 164, 1986.

[75] M. N. Khlopkin, "Structural and Superconducting transitions in V_3Si samples with various defect concentrations," *JETP Lett*, vol. 39, no. 7, pp. 358–360, 1984.

[76] D. Eckert and K. H. Berthel, "The lower critical field H_{c1} of V3Si," *Cryogenics*, vol. 15, pp. 479–480, August 1975.

[77] W. E. Pickett and D. J. Singh, "$LuNi_2B_2C$: a novel Ni-based strong-coupling superconductor," *Phys. Rev. Lett.*, vol. 72, no. 23, pp. 3702–3705, 1994.

[78] M. R. Eskildsen, P. Gamel, B. P. Barber, A. P. Ramirez, D. J. Bishop, N. H. Andersen, K. Mortensen, C. A. Bolle, C. M. Lieber, and P. C. Canfield, "Structural Stability of the square flux line lattice in YNI_2B_2C and $LuNi_2B_2C$ studied with small angle neutron scattering," *Phys. Rev. Lett.*, vol. 79, no. 3, pp. 487–490, 1997.

[79] G. M. Schmiedeshoff, C. D. Boer, M. V. Tompkins, W. P. Beyermann, A. H. Lacerda, J. L. Smith, and P. C. Canfield, "Superconductivity (and magnetism) in the Nickel Borocarbides," *J. Supercond. Nov. Magn.*, vol. 13, no. 5, pp. 847–853, 2000.

[80] D. E. Prober, M. R. Beasley, and R. Schwall, "Fluctuation-induced diamagnetism and dimensionality in superconducting layered compounds: TaS_2(pyridine)1/2 and $NbSe_2$," *Phys. Rev. B*, vol. 15, no. 11, pp. 5245–5261, 1977.

[81] F. Soto, H. Berger, L. Cabo, C. Carballeira, J. Mosqueira, D. Pavuna, P. Toimil, and F. Vidal, "Electric and magnetic characterization of $NbSe_2$ single crystals: Anisotropic superconducting fluctuations above T_c," *Physica C*, vol. 460 – 462, pp. 789 – 790, 2007.

[82] E. Jobiliong, H. D. Zhou, J. A. Janik, Y.-J. Jo, L. Balicas, J. S. Brooks, and C. R. Wiebe, “Anisotropic superconductivity in bulk CaC_6,” *Phys. Rev. B*, vol. 76, p. 052511, 2007.

[83] F. Muranányi, M. Bendele, R. Khasanov, Z. Guguchia, A. Shengelaya, C. Balnes, and H. Keller, “Muon spin rotation study of the intercalated graphite superconductor CaC_6 at low temperatures,” *J. Supercond. Nov. Magn.*, vol. 25, pp. 159–163, 2012.

[84] N. Y. Alekseyevskiy, V. I. Nizhankovskiy, and K.-H. Bertel, “Superconductivity and electronic structure of pure niobium. II. Superconductive properties of pure niobium,” *Fiz. metal. metalloved.*, vol. 37, pp. 53–64, 1974.

[85] S. P. Farrant and C. E. Gough, “Measurement of the fluctuation heat capacity of Niobium in a magnetic field,” *Phys. Rev. Lett.*, vol. 34, no. 15, pp. 943–946, 1975.

[86] D. J. Thouless, “Critical Fluctuations of a Type-II Superconductor in a Magnetic Field,” *Phys. Rev. Lett.*, vol. 34, pp. 946–949, Apr 1975.

[87] M. Willemin, A. Schilling, H. Keller, C. Rossel, J. Hofer, U. Welp, W. K. Kwok, R. J. Olsson, and G. W. Crabtree, “First-Order Vortex-Lattice Melting Transition in $YBa_2Cu_3O_{7-\delta}$ near the Critical Temperature Detected by Magnetic Torque,” *Phys. Rev. Lett.*, vol. 81, pp. 4236–4239, Nov 1998.

[88] M. Reibelt, A. Schilling, and N. Toyota, “Application of a small oscillating magnetic field to reveal the peak effect in the resistivity of Nb_3Sn,” *Phys. Rev. B*, vol. 81, p. 094510, Mar 2010.

[89] D. Majer, E. Zeldov, and M. Konczykowski, “Separation of the Irreversibility and Melting Lines in $Bi_2Sr_2CaCu_2O_8$ Crystals,” *Phys. Rev. Lett.*, vol. 75, pp. 1166–1169, Aug 1995.

[90] M. Feigel’man, V. Geshkenbein, and A. Larkin, “Pinning and creep in layered superconductors,” *Physica C*, vol. 167, no. 1–2, pp. 177 – 187, 1990.

[91] O. M. Corbino, “Über die spezifische Wärme der Metalle bei hohen Temperaturen,” *Physik. Z.*, vol. XIII, p. 375, 1912.

[92] O. M. Corbino, “Thermische Oszillationen wechselstromdurchflossener Lampen mit dünnem Faden und daraus sich ergebende Gleichrichterwirkung infolge der Anwesenheit geradzahlinger Oberschwingungen,” *Physik. Z.*, vol. XI, p. 413, 1910.

[93] P. F. Sullivan and G. Seidel, “Steady-State, ac-Temperature Calorimetry,” *Phys. Rev.*, vol. 173, pp. 679—685, 1968.

[94] Y. Kraftmakher, “Modulation calorimetry and related techniques,” *Phys. Rep.*, vol. 356, no. 1–2, pp. 1 – 117, 2002.

[95] B. T. Matthias, T. H. Geballe, S. Geller, and E. Corenzwit, “Superconductivity of Nb_3Sn,” *Phys. Rev.*, vol. 95, pp. 1435–1435, Sep 1954.

[96] D. Dew-Hughes, “Superconducting A-15 compounds: A review,” *Cryogenics*, vol. 15, no. 8, pp. 435 – 454, 1975.

[97] P. J. Lee and D. C. Larbalestier, “Microstructural factors important for the development of high critical current density Nb_3Sn strand,” *Cryogenics*, vol. 48, no. 7–8, pp. 283 – 292, 2008.

[98] J. J. Hanak and H. S. Berman, *Crystal Growth: Proceedings of the International Conference on Crystal Growth, Boston, 20-24 June, 1966*, p. 249. No. v. 2 in Journal of physics and chemistry of solids / Supplement 1967, Pergamon Press, 1967. and International Conference on Crystal Growth (1966, Boston, Mass.).

[99] H. Takei, H. Watanabe, N. Toyota, T. Fukase, and K. Kitamura, “Growth and Properties of A15-type Nb_3Sn Single Crystals,” *Jpn. J. Appl. Phys.*, vol. 22, no. Part 1, No. 5, pp. 887–888, 1983.

[100] N. Toyota, T. Itoh, M. Kataoka, T. Fukase, H. Takei, and Y. Muto, “Magnetic field effect on the martensitic transformation temperature in Nb_3Sn,” *Physica B+C*, vol. 135, no. 1–3, pp. 364 – 366, 1985.

[101] N. Toyota, T. Kobayashi, M. Kataoka, H. F. J. Watanabe, T. Fukase, Y. Muto, and F. Takei, “Interference between Superconductivity and Martensitic Transition in A15 Compounds,” *J. Phys. Soc. Jpn.*, vol. 57, no. 9, pp. 3089–3101, 1988.

[102] M. G. Adesso, D. Uglietti, R. Flükiger, M. Polichetti, and S. Pace, "Transition between the Bragg glass and the disordered phase in Nb_3Sn detected by third harmonics of the ac magnetic susceptibility," *Phys. Rev. B*, vol. 73, p. 092513, Mar 2006.

[103] R. Lortz, N. Musolino, Y. Wang, A. Junod, and N. Toyota, "Origin of the magnetization peak effect in the Nb_3Sn superconductor," *Phys. Rev. B*, vol. 75, p. 094503, Mar 2007.

[104] D.-X. Chen, E. Pardo, and A. Sanchez, "Fluxmetric and magnetometric demagnetizing factors for cylinders," *Journal of Magnetism and Magnetic Materials*, vol. 306, no. 1, pp. 135 – 146, 2006.

[105] J. R. Clem, *Magnetic Susceptibility of Superconductors and Other Spin Systems.* Springer, 1992.

[106] R. Liang, D. A. Bonn, and W. N. Hardy, "Discontinuity of Reversible Magnetization in Untwinned YBCO Single Crystals at the First Order Vortex Melting Transition," *Phys. Rev. Lett.*, vol. 76, pp. 835–838, Jan 1996.

[107] V. B. Geshkenbein, V. M. Vinokur, and R. Fehrenbacher, "ac absorption in the high-T_c superconductors: Reinterpretation of the irreversibility line," *Phys. Rev. B*, vol. 43, pp. 3748–3751, Feb 1991.

[108] C. P. Bean, "Magnetization of High-Field Superconductors," *Rev. Mod. Phys.*, vol. 36, pp. 31–39, Jan 1964.

[109] X. Ling and J. I. Budnick, *Magnetic Susceptibility of Superconductors and Other Spin Systems.* Springer, 1992.

[110] E. H. Brandt, "Superconductor disks and cylinders in an axial magnetic field. I. Flux penetration and magnetization curves," *Phys. Rev. B*, vol. 58, pp. 6506–6522, Sep 1998.

[111] E. H. Brandt, "Superconductor disks and cylinders in an axial magnetic field: II. Nonlinear and linear ac susceptibilities," *Phys. Rev. B*, vol. 58, pp. 6523–6533, Sep 1998.

[112] E. Pardo, D. Chen, and A. Sanchez, "Demagnetizing factors for completely shielded rectangular prisms," *J. Appl. Phys*, vol. 96, no. 9, pp. 5365–5369, 2004.

[113] E. H. Brandt, “Susceptibility of superconductor disks and rings with and without flux creep,” *Phys. Rev. B*, vol. 55, pp. 14513–14526, Jun 1997.

[114] D. Matthews, G. Russell, and K. Taylor, “Flux trapping energies in YBCO in the presence of a transport current,” *Physica C*, vol. 171, no. 3–4, pp. 301 – 304, 1990.

[115] L. Ma, H. Li, R. Wang, and L. Li, “The nature of the relaxation of resistivity in high-Tc superconductors,” *Physica C*, vol. 279, no. 1–2, pp. 79 – 84, 1997.

[116] G. D’Anna, M.-O. André, and W. Benoit, “Double and Triple Peaks in the a.c. Losses of Some Superconductors,” *Europhys. Lett.*, vol. 25, no. 7, p. 539, 1994.

[117] Y. Kopelevich, A. Gupta, and P. Esquinazi, “Anomalous behavior of the flux line lattice of vibrating high-T_c superconductors at 30 K in magnetic fields parallel to the CuO_2 planes,” *Phys. Rev. Lett.*, vol. 70, pp. 666–669, Feb 1993.

[118] L. J. Vieland and A. W. Wicklund, “Specific heat of niobium-tin,” *Phys. Rev.*, vol. 166, pp. 424–431, Feb 1968.

[119] E. Gmelin, “Modern low-temperature calorimetry,” *Thermochim. Acta*, vol. 29, pp. 1–39, 1979.

[120] G. R. Stewart, “Measurement of low-temperature specific heat,” *Rev. Sci. Instrum.*, vol. 54, pp. 1–11, 1983.

[121] D. Jung, I. Moon, and Y. Jeong, “Peltier AC calorimeter,” *Thermochim. Acta*, vol. 391, pp. 7–12, 2002.

[122] R. Lortz, S. Abe, Y. Wang, F. Bouquet, U. Tutsch, and A. Junod, “Modulated-bath ac calorimetry using modified commercial Peltier elements,” *Rev. Sci. Instrum.*, vol. 76, p. 103902, 2005.

[123] A. Schilling and M. Reibelt, “Low-temperature differential-thermal analysis to measure variations in entropy,” *Rev. Sci. Instrum.*, vol. 78, p. 033904, 2007.

[124] D. C. Rife and R. R. Boorstyn, “Single-Tone Parameter Estimation from Discrete-Time Observations,” *IEEE Trans. Inform. Theory*, vol. IT-20, no. 5, p. 591, 1974.

[125] R. C. L. Bosworth, “Thermal Inductance,” *Nature*, vol. 158, p. 309, 1946.

[126] T. F. McNelly, S. J. Rogers, D. J. C. R. J. Rollefson, W. M. Goubau, G. E. Schmidt, J. A. Krumhansl, and R. O. Pohl, “Heat Pulses in NaF: Onset of Second Sound,” *Phys. Rev. Lett.*, vol. 24, pp. 100–02, 1970.

[127] B. M. Weedy, “The Analogy between Thermal and Electrical Quantities,” *IEEE Electric. Pwr. Syst. Res.*, vol. 15, pp. 197–201, 1988.

[128] D. D. Joseph and L. Preziosi, “Heat Waves,” *Rev. Mod. Phys.*, vol. 61, no. 1, pp. 41–73, 1989.

[129] D. F. Berndt and S. C. Dutta Roy, “Inductor simulation with a single unity gain amplifier,” *IEEE J. Solid-State Circ.*, vol. SC-4, pp. 161–162, 1969.

[130] D. S. Simons and M. B. Salamon, “Specific heat and resistivity of gadolinium near the Curie point in external magnetic fields,” *Phys. Rev. B*, vol. 10, no. 10, pp. 4680–4686, 1974.

[131] D. Allan, “Statistics of atomic frequency standards,” *P. IEEE*, vol. 54, pp. 221–230, feb. 1966.

[132] W. Riley, *Handbook of Frequency Stability Analysis.* No. 1065 in NIST Special Publication, NIST, 2008.

[133] D. Allan and J. Barnes, “A Modified "Allan Variance" with Increased Oscillator Characterization Ability,” in *Thirty Fifth Annual Frequency Control Symposium. 1981*, pp. 470 –475, may 1981.

[134] E. Rubiola, *Phase Noise and Frequency Stability in Oscillators.* The Cambridge RF and Microwave Engineering Series, Cambridge University Press, 2010.

Danksagung

Ich bedanke mich bei...

- Herrn Prof. Schilling, der mir diese Doktorarbeit in seiner Arbeitsgruppe ermöglicht hat, und bei auftretenden Problemen immer einen guten Rat hatte.
- den Werkstätten des Physik Instituts die mir bei technischen Herausforderungen mit Rat und Tat geholfen haben.
- meiner Familie für die finanzielle und moralische Unterstützung während des Studiums und darüber hinaus.
- meiner Freundin für ihre Liebe und Geduld.
- den Mitgliedern der Arbeitsgruppe Prof. Schilling für viele fachliche und freundschaftliche Diskussionen und Hilfe.
- den Mitgliedern der Arbeitsgruppe Prof. Keller ebenfalls für fachliche und freundschaftliche Diskussionen und Hilfe.
- meinen Freunden in Zürich für eine gute Zeit und moralische Unterstützung.
- den restlichen Mitgliedern des Physik Instituts für die positive und unbürokratische Atmosphäre.

Diese Doktorarbeit entstand mit Fördergeldern des *Schweizer Nationalfonds zur Förderung der Wissenschaftlichen Forschung* Grant-Nr. 20-131899

Lebenslauf

Bossen
Olaf
22.4.1981
Deutschland

Ausbildung

- **Abitur**, *Gymnasium Laatzen*, Deutschland, 2000
- **Physik Vordiplom**, *Humboldt Universität zu Berlin*, Deutschland, 2001–2002
- **Physik Studium**, *Universidat de Salamanca*, Spanien, 2003–2004
- **Physik Diplom**, *Eidgenössische Technische Hochschule Zürich*, Schweiz, 2004–2007
  Diplomarbeit „Time Resolved Photoluminescence of individual Carbon Nanotubes“
- **Doktorand**, *Universität Zürich*, Schweiz, 2008 – 2013

Publikationen

- Z. Shermadini, A. Krzton-Maziopa, M. Bendele, R. Khasanov, H. Luetkens, K. Conder, E. Pomjakushina, S. Weyeneth, V. Pomjakushin, O. Bossen, A. Amato, “Coexistence of Magnetism and Superconductivity in the Iron-Based Compound $Cs_{0.8}(FeSe_{0.98})_2$”, *Phys. Rev. Lett.*, vol. 106, pp. 117602, 2011.

- O. Bossen and A. Schilling, “LC-circuit calorimetry”, *Rev. Sci. Instrum.*, vol. 82, pp. 094901, 2011.
- O. Bossen and A. Schilling, “Estimates for the thermodynamic signatures of vortex-lattice melting in conventional superconductors”, *Physica C*, vol. 483, pp. 201 – 206, 2012.
- O. Bossen and A. Schilling, “AC magnetic susceptibility in the vortex lattice region in Nb_3Sn”, *Physica C*, vol. 492, pp. 133 – 137, 2013.

A. Amplifier Devices and Circuit Diagrams

A.1. LCCC amplifier

A.1.1. Device

Figure A.1.: The LCCC oscillator amplifier device. Controls in the upper row from left to right: Gyrator resistance, coupling switch, diode stage voltage expansion, diode stage gain, output gain, power button. Connectors in the lower row from left to right: PPMS sample space connector, amplified input, diode stage voltage, output voltage, AGC gain voltage input, offset voltage input

A.1.2. LCCC Amplifier Schematic (main part)

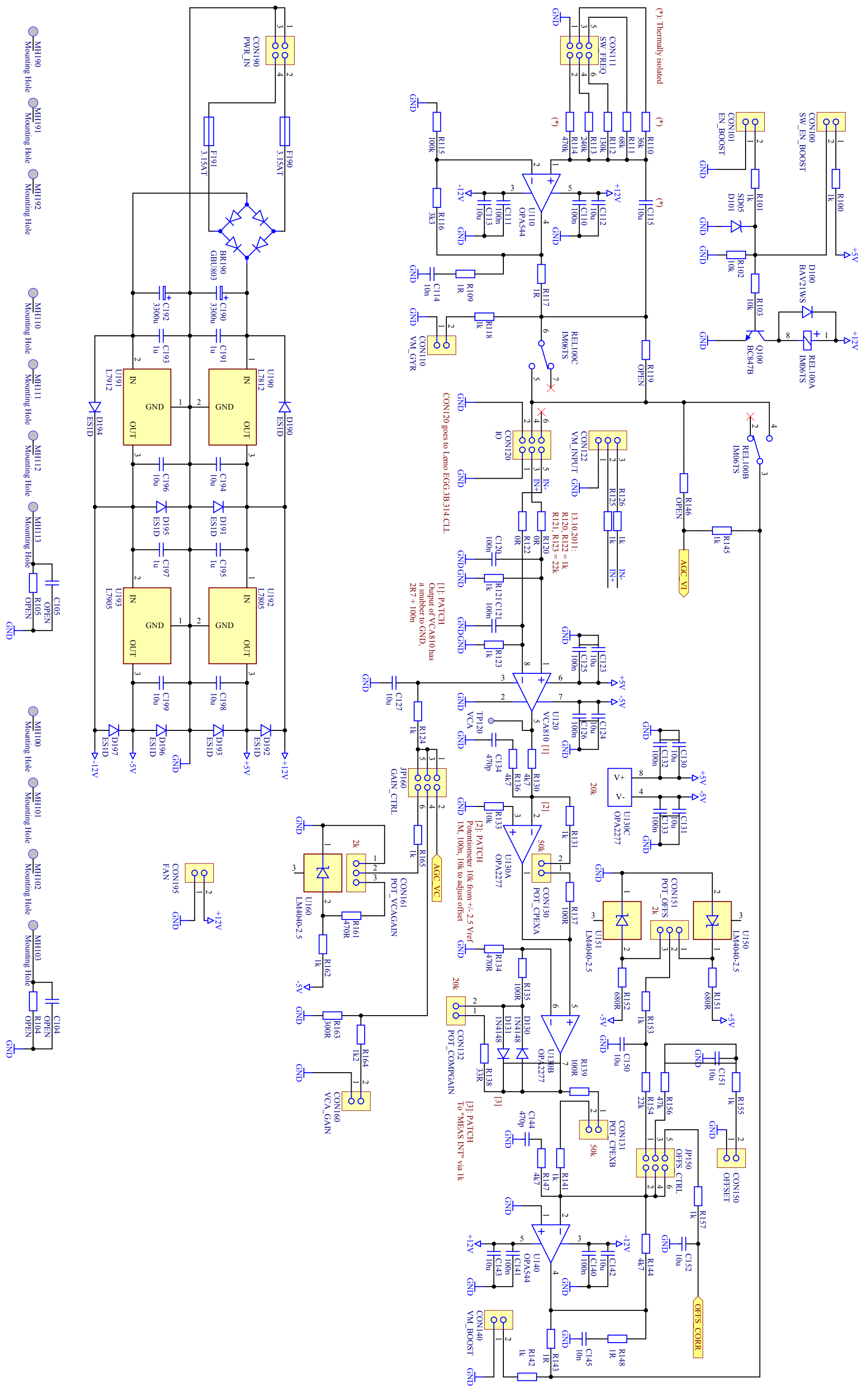

Figure A.2.: Main circuit of the gyrator and amplifier circuit of the thermal LC-oscillator calorimeter

A.1.3. LCCC Amplifier Schematic (unused AGC part)

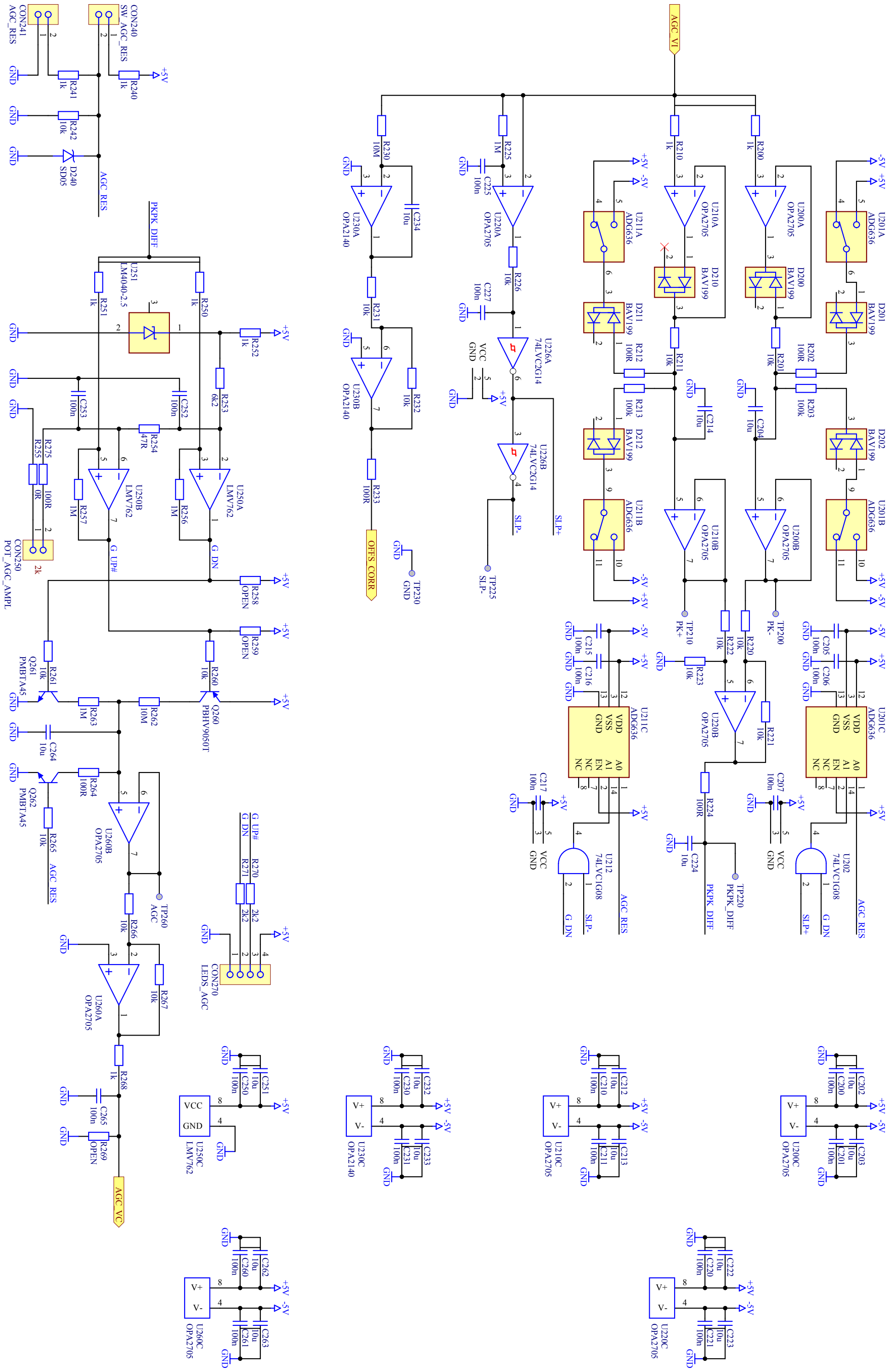

Figure A.3.: additional circuitry for automatic amplitude stabilization, this part is unused at present

A.2. Main Measurement Circuit

A.2.1. KHz-Amplifier

KHz-Amplifier Device

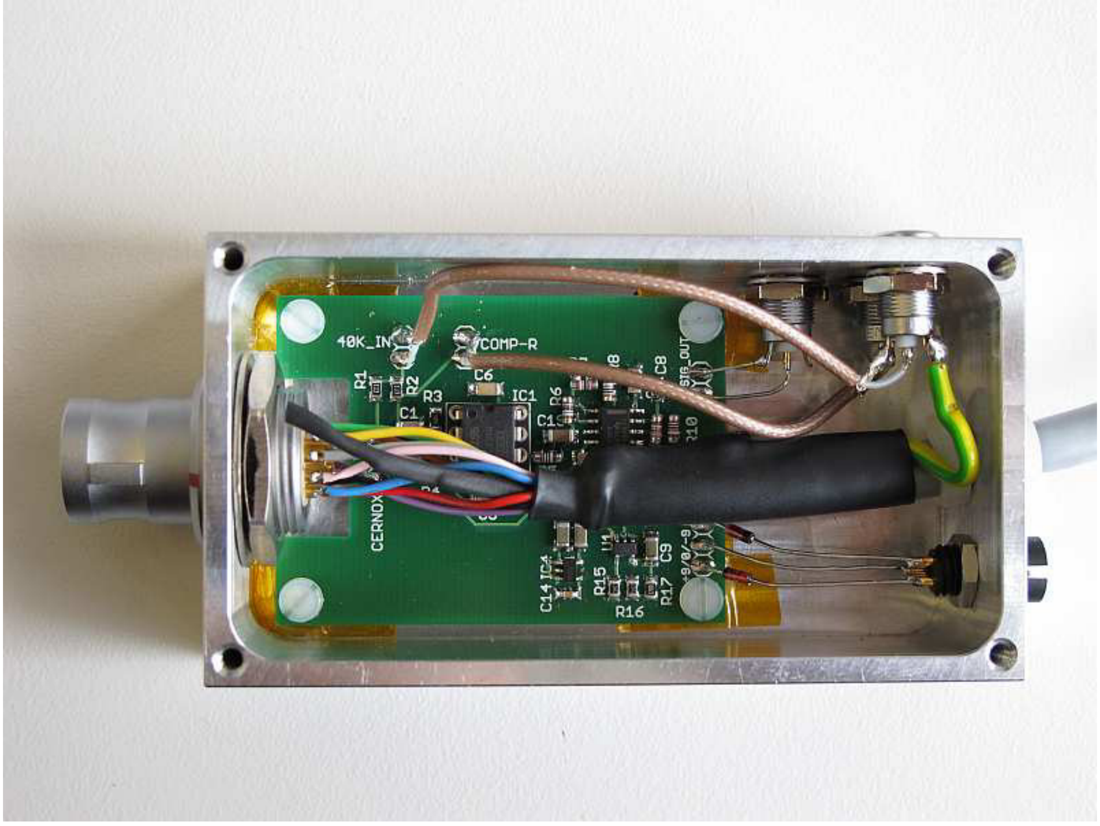

Figure A.4.: The open half Wheatstone bridge KHz amplifier box. Sensitive signals for the resistance decade and the input and output are carried in BNC/LEMO cables and connected to the side ports. Unused pins are passed through the amplifier unaltered to allow for auxiliary measurements. The aluminum box provides for a 4π sr shielding.

KHz-Amplifier Schematic

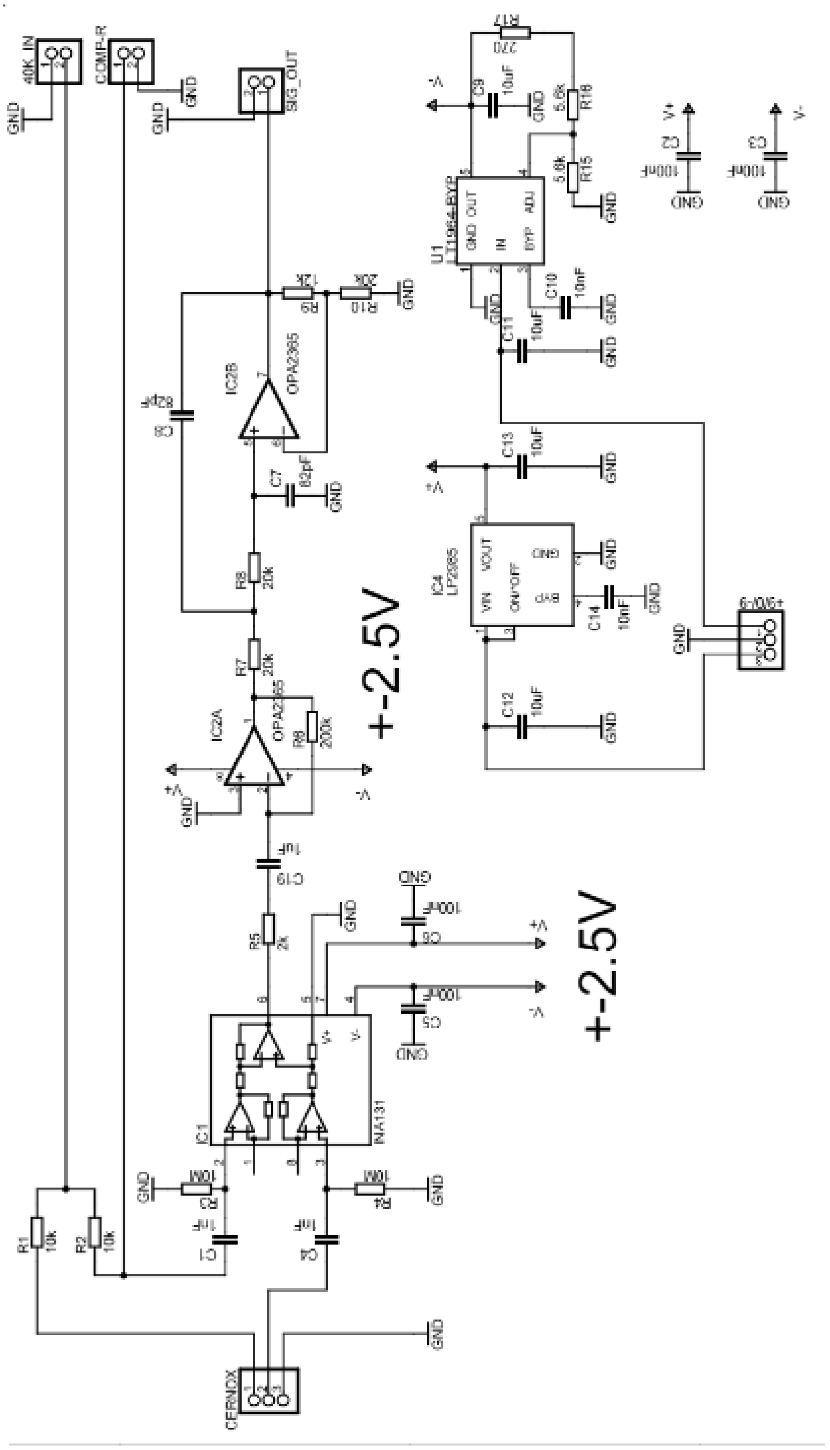

Figure A.5.: Schematic of the half Wheatstone bridge KHz amplifier displayed in Fig. A.4

.

B. Measurement pucks

Figure B.1.: Closed measurement puck used for the application of a shaking field in parallel to the main field for heat capacity measurements

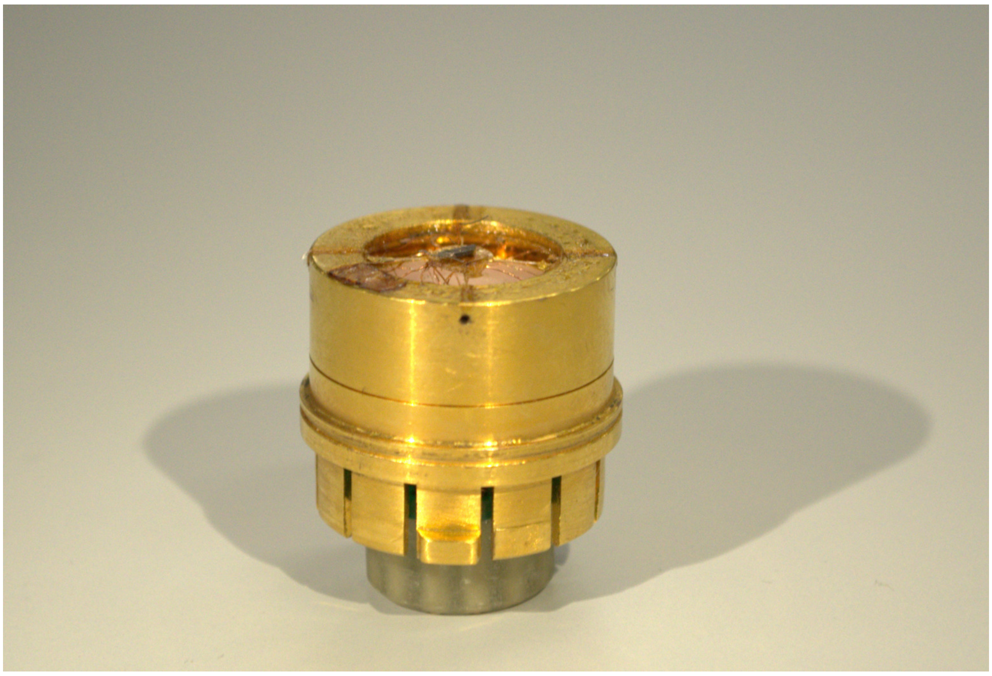

Figure B.2.: The same puck as in Fig. B.1 with radiation shield removed, showing the suspended measurement platform.

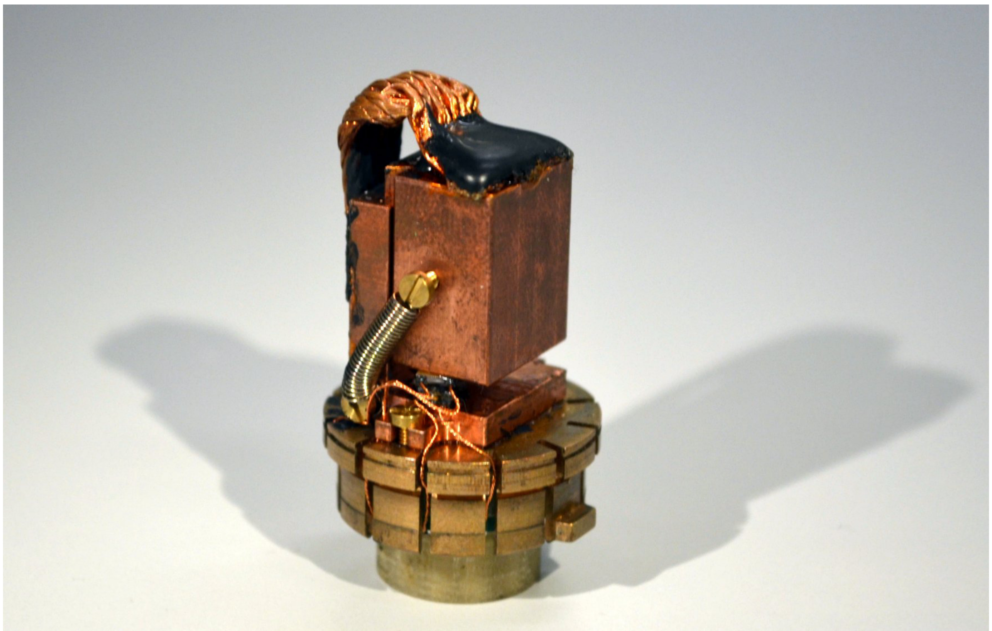

Figure B.3.: PPMS puck for LC-oscillator measurements. The large copper block on top is used as a thermal bath, and is attached to the base using a dove tail sliding mechanism and copper braid wire to provide for good thermal contact. Below are the sandwiched Peltier elements.